POLITECNICO DI MILANO

School of Industrial and Information Engineering

Master Thesis in Electrical Engineering

Torsional Vibrations Suppression by Disturbance-Observer-Based Control Approach

Supervisor: Prof. Roberto Perini

Co-Supervisor: Dr. Dejan Pejovski

Master thesis of:

Mohammad Hashim Saleh Al Takrouri

Matr. 911677

Academic year: 2020-2021

This page left intentionally blank

Acknowledgment

First and foremost, I would like to express my special thanks and gratitude to everyone who supported me throughout my study stages in Politecnico di Milano university, starting from the very first year and up to the final moments. I express my warm thanks to my project professor Roberto Perini, and the supervisor Doctor Dejan Pejovski for their assistance and dedicated involvement in every step throughout the project period, whom without their guidance and directions this project wouldn't come out and finished in this form. I would also thank my parents and friends who helped me a lot in finishing this project within the limited time frame. Thank you all.

This page left intentionally blank

Contents

List of Figures

List of Tables

Abstract

The problem of torsional vibrations appears when at least two rotational masses are interconnected by elastic shaft. These vibrations can amplify if the electromagnetic torque frequency of the motor coincides with the torsional natural frequency (TNF). Large vibrations can damage the machine and reduce the level of reliability. In this thesis, the origin of these mechanical torsional vibrations is explained in detail, starting by describing the mechanical system with Newton's equation of motion and then analysing its characteristics through transfer functions and bode plots response of the motor and load transfer functions. The sources of TNF excitors are presented, and electrical harmonic excitors are in the focus of this work.

A review of several methods of torsional vibration suppression is conducted by explaining their main idea and listing the advantages and disadvantage of each approach. One of the systems that is susceptible to the torsional vibrations are the axial flux permanent magnet machines due to its modular configuration. The machine concept is presented, and the electrical model is prepared. The electromagnetic torque harmonic spectrum is briefly described for synchronous machine that is supplied from a typical variable-frequency drive. After the TNF has been specified for the system and the order of electromagnetic torque harmonics is identified, a useful tool referred to as Campbell diagram is used to link both the electrical and mechanical system together and pinpoint the resonance intersections.

The main work of this thesis starts by designing a conventional speed/torque and current/voltage PI regulators for a one-mass machine model, then the motivation of the disturbance observer-based control (DOBC) is explained via frequency domain and time domain formulations. Since DOBC methods have the patch feature where the original control scheme of the system is unaffected by it, the original tuning of the PI regulators is left unchanged. Two types of observers are introduced, the first kind is referred to as linear Luenberger observer which is designed for our particular system, and then used to test the effectiveness of the DOBC approach. The nonlinear extended state observer is the second type of observer, which shows some design advantages over the former in terms of robustness against system model uncertainties. The effectiveness of observers with the implementation of DOBC method was tested under the system passing through the resonance intersections and under the steady-state resonance condition. All the simulated tests showed positive results for the suppression of torsional vibrations.

This page left intentionally blank

Chapter 1: Introduction

Environmental, economic, and social pressures towards cleaner energy have pushed the world into renewable energy solutions. In addition, recent developments in rare earth permanent magnet materials and power electronic have been a key player in wind turbine farms with modular axial-flux permanent magnet machines which due to its high efficiency, small size, light weight, and reliability are superior compared to the conventional radial machine. Since there are several rotational masses in the axial machine, the torsional vibration issue threatens its reliability level.

The thesis will explain the characteristics of axial machine from the mechanical aspects to the electrical ones, as well as their links in order to propose a control scheme based on DOBC to tackle the torsional vibrations problem.

1.1 Aim of the thesis

The objective of this thesis is to design a controller based on disturbance observer methodology to suppress the torsional vibrations that occur in axial-flux permanent magnet machines. The controller should behave in a robust manner, which means that under variation of the mechanical or the electrical parameters it should detect and suppress the vibration to ensure smooth response of the system.

1.2 How the book is organized?

The book is organized in five chapters as follows:

- Chapter 2 defines the torsional vibrations starting by analysing the one-mass and two-mass mechanical models, describing the system with Newton's equation of motion. The torsional vibration origin is explained, and the transfer functions of the motor speed and load speed are obtained. In addition, the resonance frequency and antiresonance frequency values are obtained for the system under analysis. Finally, in the second section of the chapter the sources of electrical resonance excitors are explained along with the problems of the torsional vibrations on the mechanical systems.

- Chapter 3 summarizes a complete review on the torsional vibration suppression methods. The summary is limited to the approaches that tackle the resonance in a control system. The challenges of each method are listed and at the end of the chapter the differences between methods, advantages and disadvantages are reported.

- Chapter 4 covers the electrical aspect of the machine. In the first section the machine, "axial-flux permanent magnet machine", and its constructional configurations are reviewed. The electrical model of the axial machine consisting of the direct and quadrature

part is briefly reported. In the final two sections, the power source and the harmonics excitors originated from such a system are reported and linked to the mechanical resonance through Campbell diagram.

- Chapter 5 is the main contribution of this thesis, where the disturbance observer-based control scheme is analysed in the Laplace domain and time domain. The basic linear Luenberger observer is introduced and designed for our specific system in the third section. After the observer has been designed, the basic concept of the feedforward compensation is explained for the two-mass torsional mechanical system and then the system is simulated to test the feasibility of the DOBC method. Finally, an alternative observer type is presented named as “nonlinear extended state observer” and designed for our particular system. The second type observer is also simulated in MATLAB to be compared with the linear type observer.

Chapter 2: Problem Definition

This chapter covers the main issue under the study and the target of this work. Starting in the first section with the analysis of the torsional vibrations in the mechanical model for two mass systems. In the second section the sources of the mechanical resonance sources will be reviewed. Finally, in the last section Campbell diagram is reviewed with the construction of the diagram for our specific system.

2.1 Multi-mass systems and torsional vibrations

The shaft connecting two rotating masses, such as a motor and its load, is ideally assumed to have infinite stiffness, thus the two bodies are rigidly connected, and the mechanical model is referred to as one-mass system. The mentioned model is represented in Figure 2-1. Where the applied electromagnetic torque is given by T_M, T_L is the load torque, ω is the mechanical speed, B_t is the equivalent viscous damping, and J_t is the total inertia of the masses.

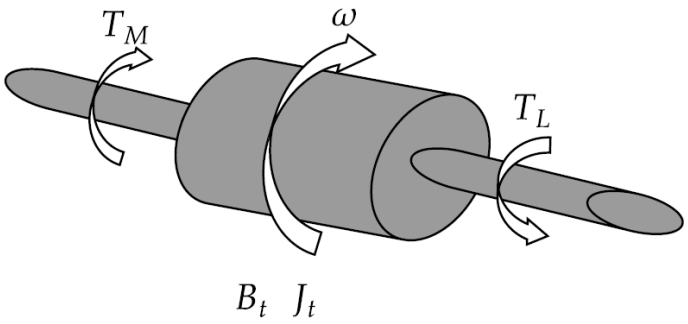

Figure 2-1 One-mass rotational model

The equation governing the one-mass system is based on the elementary principles in dynamics which is given by:

$$T_m - T_L = J_t \frac{d\omega}{dt} + B_t \omega \tag{2-1}$$

Usually such electrical motor systems are designed with the previous assumption. However, any shaft tends to twist as it transmits torque from one end to another giving rise to the problem of torsional vibrations. The phenomena rise in such rotational system where more than one mass is considered or when the mechanical system is a "multi-mass" system [1]. The torsional vibrations can be illustrated by considering the simplest torsional system consisting of two masses and a shaft connecting them, as shown in Figure 2-2, where the motor side, shaft, and the load side variables are defined in Table I.

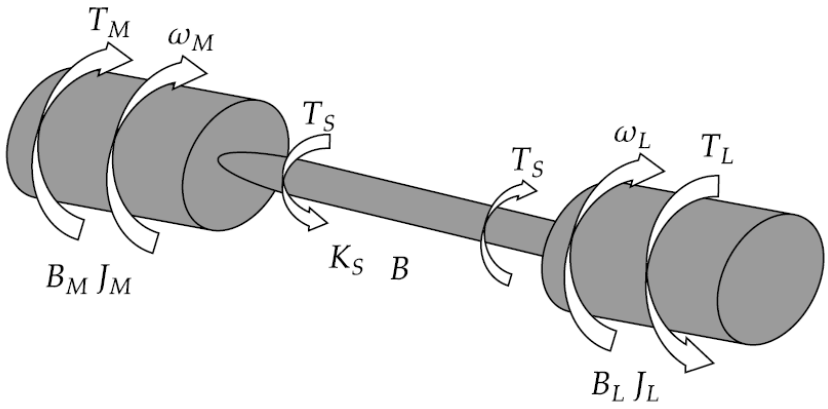

Figure 2-2 Two-mass system which consists of a motor and its load

Table I Two-mass system variables

Variable	Motor Side	Shaft	Load	Unit
Inertia	J_M		J_L	kgm^2
Torque	T_M	T_s	T_L	Nm
Speed	ω_M		ω_L	rad/s
Angle	θ_M	$\theta_M - \theta_L$	θ_L	rad
Stiffness		K_s		Nm/rad
Damping viscous friction	B_M	B	B_L	Nms/rad

The shaft variables: T_s and $(\theta_M - \theta_L)$ are referred to as torsional torque and torsional twist angle or angular deflection, respectively. In order to understand the cause of the torsional vibration problem, analysis of the transfer functions of the motor side and load side must be conducted. The study starts with the differential equations of rotational motion that govern the system, shown in Fig. 2.2; they are given by:

Motor side: $$J_M(\dot{\omega_M}) + B_M\omega_M = T_M - T_s \quad (2\text{-}2)$$

Load side: $$J_L(\dot{\omega_L}) + B_L\omega_L = -T_L + T_s \quad (2\text{-}3)$$

Torsional torque: $$T_s = K_s(\theta_M - \theta_L) + B(\omega_M - \omega_L) \quad (2\text{-}4)$$

The previous system can be transferred to the Laplace domain and represented in the block diagram shown in Figure 2-3.

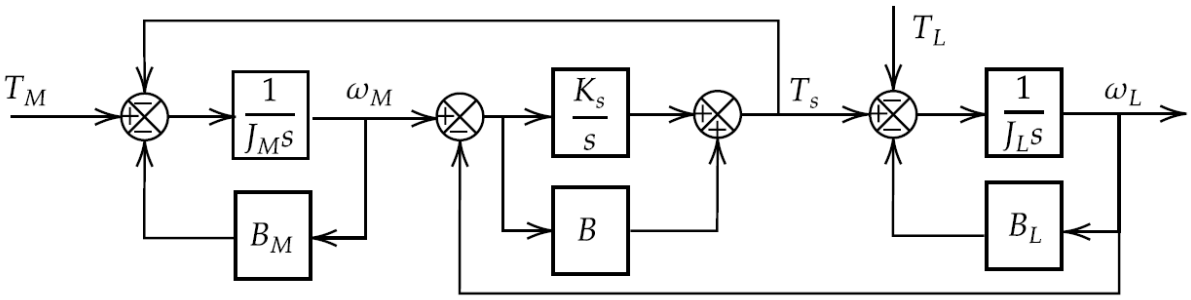

Figure 2-3 Two-mass system block diagram

Now the transfer function from the applied mechanical torque (T_M) to the motor speed (ω_M) and the transfer function from applied mechanical torque (T_M) to the load speed (ω_L) can be found by analysing Fig. 2.3 while neglecting the external disturbance of the load torque. Starting from the motor speed we have:

$$\omega_M = (T_M - T_s - B_M\omega_M)\frac{1}{J_M s}$$

$$\omega_M = (T_M - T_s)\left(\frac{1}{J_M s + B_M}\right) \tag{2-5}$$

Defining T_s:

$$T_s = (\omega_M - \omega_L)(\frac{K_s}{s} + B) \tag{2-6}$$

Where ω_L can be found as:

$$\omega_L = (-B_L\omega_L + T_s)\frac{1}{J_L s}$$

$$\omega_L = T_s\frac{1}{J_L s + B_L} \tag{2-7}$$

Substituting (2-7) into (2-6) we have:

$$T_s = (\omega_M - T_s\frac{1}{J_L s + B_L})(\frac{K_s}{s} + B)$$

$$T_s = \omega_M\frac{(K_s + Bs)(J_L s + B_L)}{J_L s^2 + B_L s + K_s + Bs} \tag{2-8}$$

Finally substituting (2-8) into (2-5) results:

$$\omega_M = \left(T_M - \omega_M\frac{(K_s + Bs)(J_L s + B_L)}{J_L s^2 + B_L s + K_s + Bs}\right)\left(\frac{1}{J_M s + B_M}\right)$$

$$\omega_M(1 + \frac{(K_s + Bs)(J_L s + B_L)}{(J_L s^2 + B_L s + K_s + Bs)(J_M s + B_M)} = T_M\left(\frac{1}{J_M s + B_M}\right)$$

$$\omega_M\left(\frac{(J_L s^2 + B_L s + K_s + Bs)(J_M s + B_M) + (K_s + Bs)(J_L s + B_L)}{(J_L s^2 + B_L s + K_s + Bs)}\right) = T_M$$

Solving for ω_M / T_M to find the first transfer function $G_1(s)$:

$$G_1(s) = \frac{\omega_M}{T_M} = \frac{J_L s^2 + B_L s + K_s + Bs}{J_L J_M s^3 + [B_L J_M + B_M J_L + B J_{tot}]s^2 + [K_s J_{tot} + B_M B_L + B B_{tot}]s + K_s B_{tot}} \tag{2-9}$$

Where $J_{tot} = J_M + J_L$ and $B_{tot} = B_M + B_L$. In a similar manner, the transfer function of from T_M to ω_L can be found starting by defining the load speed ω_L:

$$\omega_L = (-B_L \omega_L + T_s)\frac{1}{J_L s}$$

$$\omega_L = T_s \frac{1}{J_L s + B_L} \tag{2-10}$$

Defining T_s:

$$T_s = (\omega_M - \omega_L)\left(\frac{K_s}{s} + B\right) \tag{2-11}$$

and substituting the load speed from (2-5), we have:

$$T_s = \left((T_M - T_s)\left(\frac{1}{J_M s + B_M}\right) - \omega_L\right)\left(\frac{K_s}{s} + B\right)$$

$$T_s = T_s = \left(T_M\left(\frac{1}{J_M s + B_M}\right) - \omega_L\right)\frac{(K_s + Bs)(J_M s + B_M)}{J_M s^2 + B_M s + K_s + Bs} \tag{2-12}$$

Replacing T_s from the previous formula into (2-10) results:

$$\omega_L = \left(T_M\left(\frac{1}{J_M s + B_M}\right) - \omega_L\right)\frac{(K_s + Bs)(J_M s + B_M)}{J_M s^2 + B_M s + K_s + Bs}\frac{1}{J_L s + B_L}$$

After rearrangement and solving for the transfer function ω_L / T_M noted by $G_2(s)$:

$$\frac{\omega_L}{T_M} = G_2(s) = \frac{Bs + K_s}{J_L J_M s^3 + [B_L J_M + B_M J_L + B J_{tot}]s^2 + [K_s J_{tot} + B_M B_L + B B_{tot}]s + K_s B_{tot}} \tag{2-13}$$

The damping in the rotational systems is small and has little effect on the torsional phenomena. Hence, in the following analysis it is neglected [2]. Which transforms the obtained transfer functions $G_1(s)$ and $G_2(s)$ from (2-9) and (2-13) into the following:

$$G_1(s) = \frac{\omega_M}{T_M} = \frac{J_L s^2 + K_s}{J_M J_L s^3 + (J_M + J_L)K_s s} \tag{2-14}$$

$$G_2(s) = \frac{\omega_L}{T_M} = \frac{K_s}{J_M J_L s^3 + (J_M + J_L) K_s s} \tag{2-15}$$

The transfer function $G_1(s)$, has two complex conjugate zeros at:

$$\mathrm{s_{zeros}} = \pm j\sqrt{K_s\ 1/J_L} \tag{2-16}$$

Which were referred to as the anti-resonance frequency in the introduction noted by ω_{ares}, and in the denominator lie three poles at:

$$s_1 = 0\ , s_{2,3} = \pm j\sqrt{K_s(1/J_M + 1/J_L)} \tag{2-17}$$

As were they noted by the resonance frequency ω_{res} or as Torsional Natural Frequency (TNF). Notice the roots determining the anti-resonance frequency are absent in $G_2(s)$, while both of the resonance frequency and anti-resonance frequency exist in $G_1(s)$. In order to illustrate the phenomena, the amplitude and phase frequency response of the system are plotted in Figure 2-4[3].

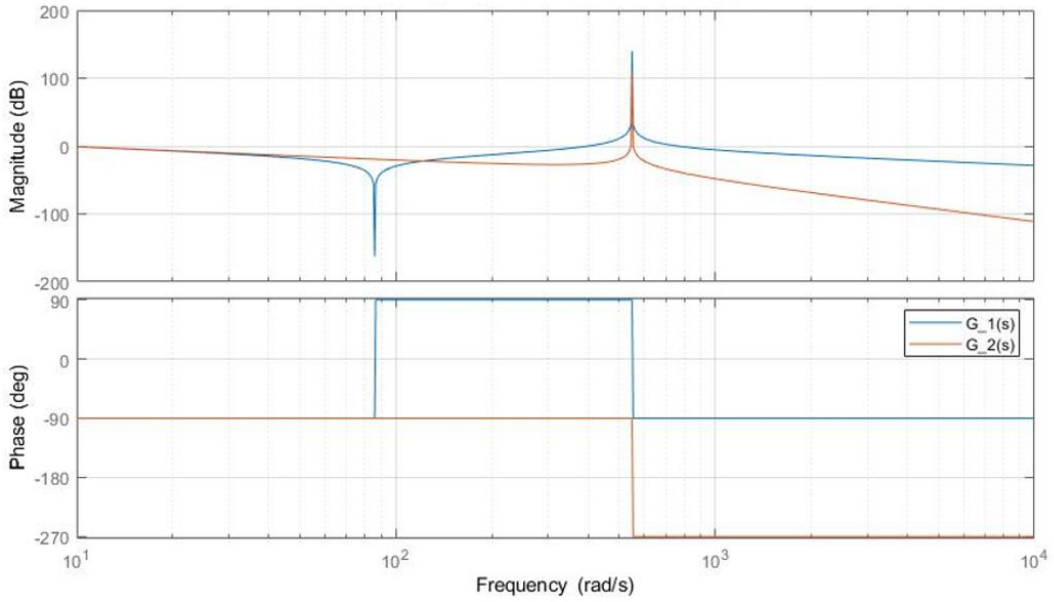

Figure 2-4 $G_1(s)$ and $G_2(s)$ Bode diagram indicating the resonance frequency and antiresonance frequency

As it can be noticed in Figure 2-4, the absence of the anti-resonance frequency in the transfer function $G_2(s)$ between the applied electromagnetic torque T_M and the load speed ω_L makes the response lag behind the input by more than 180 degrees. In contrast, the transfer function $G_1(s)$ has the anti-resonance frequency and the output is delayed by less than 180 degrees. The mismatch between the two transfer functions makes the motor speed and the load speed different. Moreover, at the resonance frequency ω_{res} this mismatch is amplified. Hence, if the system is operated under the resonance condition, i.e., the input electromagnetic T_M frequency coincides with the TNF, the speed difference between the motor speed (ω_M) and load speed (ω_L) increases and consequently the motor angle (θ_M) and load angle (θ_L). Having a large

angular deflection between the two mass applies a high torque on the shaft as it has been analysed with the torsional torque formula:

$$T_s = K_s(\theta_M - \theta_L) \tag{2-18}$$

If the system consists of additional masses, it is referred to as multi-mass system and it is characterized with additional torsional natural frequencies TNFs at higher frequencies. Most systems are analysed as two masses and then the study is extended to multi-mass. This is justified since the additional TNFs are easily suppressed and affected more by the natural damping of the system [4].

The number of poles of the mechanical system are proportional to the number of masses of system. As has been found in the previous analysis of the two-mass system there were three poles with the first one at zero and the others complex conjugate, meaning that if a rotational system has N masses then the number of TNFs in the system is $N - 1$.

The two-mass system used in the analysis has the specifications given in Table II.

Table II Machine system under the study specifications

Rated power	6.91	kW
Rated voltage	350	V
Rated speed	314	RPM
Motor's moment of inertia J_M	$2.7 * 10^{-3}$	$kgm2$
Load's moment of inertia J_L	0.1080	$kgm2$
Friction coefficient B	0	Nms/rad
Equivalent angular stiffness*	794	Nm/rad
Stall torque	22	Nm
Peak torque	88	Nm
Rated frequency	150	Hz
Number of poles p	6	$Poles$
Synchronous resistance R_s	0.39	Ω
Synchronous Inductance L_s	$4.8 * 10^{-3}$	H
Stall current I_{stall}	15.6	A
Peak Current I_{peak}	70	A

By using the defined mechanical system values in the previous table the resonance and anti-resonance frequencies can be calculated from (2-16) and (2-17) which gives:

$$\omega_{res} = \sqrt{K_s(1/J_M + 1/J_L)} = \sqrt{794(\frac{1}{2.7 * 10^{-3}} + \frac{1}{40 * 2.7 * 10^{-3}})} = 549\, rad/s \tag{2-19}$$

$$\omega_{ares} = \sqrt{\frac{K_s}{J_L}} = \sqrt{794/40 * 2.7 * 10^{-3}} = 85.74\, rad/s \tag{2-20}$$

* This low value of stiffness coefficient represents a modified physical system with elastic coupling in order to explore the torsional vibrations

The low value of resonance frequency (ω_{res}), is obtained on purpose to study the system under the influence of torsional vibrations.

The two-mass system is constructed in MATLAB Simulink in order to be ready for testing simulations. To retain some generality the Simulink model of the two mass system has been created by using the equations (2-2), (2-3), and (2-4) while neglecting the motor (B_M) and load (B_L) side dampings. The model is reported in Appendix B.

2.2 Electrical sources of resonance

Electrical excitors can rise from the variable frequency drives (VFDs). Typically a VFD consists of a rectifier, DC link and a voltage source inverter (VSI) or current source inverter (CSI) as seen in Figure 2-5. The rectifier in most cases is diode-bridge type of 6 or 12 pulses. The inverter can be operated using PWM or square wave modulation[5]. Referring to Figure 2-5 and neglecting the transformer, the rectifier will produce DC voltage with an amount of pulses of p_{rec} of the supply frequency (f_{supply}) to the DC-link. The VSI takes samples from the DC-link voltage and feeds the motor with the three phases at the motor frequency f_m. Since VSI input is not constant and contains pulses, the inverter output will not present constant maximum pulses but vary according to the dc-link variation. The closed form of the harmonics, named harmonic excitation, is:

$$f_{\text{excitation}} = \begin{cases} mf_{\text{supply}} \\ kf_m \end{cases} \quad m,k = 1,2,.. \tag{2-21}$$

Where m and k are integer coefficients and previous form gives rise to integer order of the mains frequency or the output of the inverter's frequency.

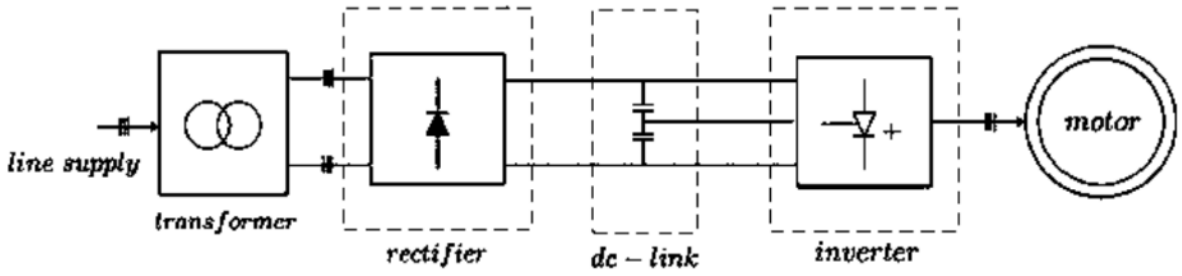

Figure 2-5 Double-stage conversion topology that consists of rectifier, DC link and inverter

Additionally, inter-harmonics excitations exist due to the modulation technique in the inverter, for example, PWM. The PWM VSI samples the voltage from the DC-link which is smoothed due to a capacitor with a finite value. The capacitors attenuate the high frequency components more than the lower ones. A more generalized form that include these inter-harmonics is:

$$f_{\text{excitation}} = |\underbrace{c_1 p_{rec} f_{supply}}_{m} \pm \underbrace{c_2 p_{inv} f_m}_{\text{k}}| \tag{2-22}$$

where

$$m = 0 \; and \; k \neq 0 \; \Rightarrow integer \; multiples \; of \; f_m$$

$$m \neq 0 \; and \; k = 0 \; \Rightarrow integer \; multiples \; of \; f_{supply}$$

$$m \neq 0 \; and \; k \neq 0 \; \Rightarrow non - integer \; harmonics$$

c_1, c_2 are integer multipliers and p_{inv} is number of pulses of the inverter. However, the amplitude of the inter-harmonics is often too low to excite the TNF.

In addition to the harmonics produced by the power converters, there are other harmonic orders that can exist as consequence from special cases. The second order harmonic of the mains frequency can result when the system is operating under unbalanced conditions or in the case of a fault. In synchronous machines equipped with a rotor cage, a harmonic order proportional to the slip is produced. A convenient form to study the excitation harmonics is to write the harmonics order in term of the speed and number of poles of the machine by replacing the motor frequency with the speed by using the following relationship:

$$\Omega = 120 \cdot \mathrm{f_m}/\mathrm{N_p}$$

Where f_m is the electrical frequency of the machine, and N_P is the number of poles. These harmonics give rise to torque pulsation that might coincide with the TNF and resonate which increases the displacement of the relative angle between the motor and load as explained in the previous section. Each mechanical system has a maximum angular deflection tolerance or maximum torsional torque it can handle before it leads to loss of energy, destroyed couples, compressed shaft, and downtime. Figure 2-6 shows the effect of the resonance on a shaft[5].

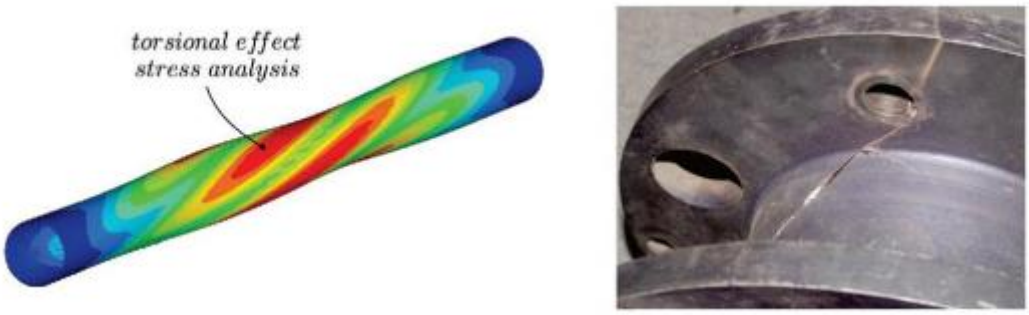

Figure 2-6 Torsional effect and the difference between angle on the two end of the shaft (left) and broken shaft due to the resonance (right)

In practical systems there are numerous sources of disturbances whose frequency can coincide with the TNF and excite the torsional vibration condition. These Excitors can be from the mechanical world like systems with gears, impellers, or propellers[6]. Excitors can be avoided in the plant design stage with solutions such as changing the coupling sizes or style, using flywheels or using different shaft material.

Chapter 3: Torsional vibration suppression methods

In the literature there are various methods to approach the problem of the torsional vibration. By looking at the problem from the mechanical perspective, the solution has to be analysed and implemented in the system during the design stage before the installation has been completed. The possible mechanical solutions are, for example, changing the coupling sizes or style, using flywheels, or changing shaft material or size. However, the aforementioned mechanical methods have the downsides such as the cost of additional materials and required periodic maintenance, which gives more popularity to solving the problem by using a control strategy.

The general control system for permanent magnet synchronous machine (PMSM) is shown in Figure 3-1. It mainly consists of two controllers: On the quadrature axis, there is the speed/torque controller. On the direct axis, there is a current controller

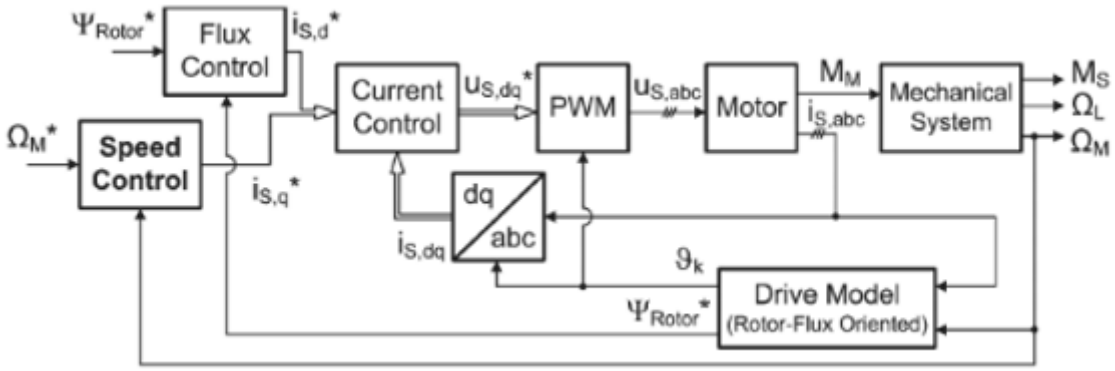

Figure 3-1 Conventional control scheme for PMSM

In most cases these two controllers are realized with Proportional-Integral (PI) regulators. Throughout the study of vibration suppression methods, the PI current controller behaviour is neglected, and the electromagnetic torque reference is applied directly to the mechanical system. In fact, many of the methods that will be discussed in the next sections are treating the current controller as a unity gain or as a first order time delay with small time constant.

3.1 Conventional PI/PID controller

The conventional approach to control the speed is by using a PI regulator. This control method works well only for one mass systems, where the system is treated as one block and both speeds of the motor and load are equal. The issue takes place in the first PI speed controller, where there are not enough control parameters to place all the poles of the system when considering two-mass system instead of one. As in the conventional system seen in Figure 3-2, only one of the mechanical parameters is measured and fed back to the speed controller which is the motor speed Ω_M. The constricted ability to place the poles limits the speed dynamics and the damping of the torsional vibrations is not fully achieved [7]. The downside of this method is that the poles cannot be freely placed, and it can only damp the torsional oscillations within certain ranges of the inertia ratio J_L/J_M. The reason behind the constricted poles in the regular PI regulator can be illustrated from Figure 3-2, by studying the transfer function from the motor

speed reference (ω_M^*) to the motor speed given by the measurement unit (ω_M) while taking into account the PI speed controller, in contrast to equation (2-9) where only the mechanical system was analysed. The electrical system is neglected as mentioned before, thus the transfer function is given by:

$$\frac{\omega_M(s)}{\omega_M^*(s)} = \frac{(K_I + s \cdot K_P)(s^2 \cdot \frac{1}{J_M} + \frac{K_s}{J_M J_L})}{s^4 + s^3 \cdot \frac{\mathrm{K_p}}{J_M} + s^2 \frac{K_I J_L + K_s J_M + K_S J_L}{J_L J_M} + s \frac{\mathrm{K_I} K_s}{J_M J_L} + \frac{K_I K_s}{T_M T_L}} \quad (3\text{-}1)$$

If the system in

(3-1), is rearranged to:

$$\frac{\omega_1^2 \omega_2^2}{(s^2 + 2\zeta_1\omega_1 s + \omega_1^2)(s^2 + 2\zeta_2\omega_2 s + \omega_2^2)} \quad (3\text{-}2)$$

The following parameters are identified:

The natural frequencies ω_1 and ω_2

The damping coefficients ζ_1 and ζ_2

The denominator in

(3-1) is a polynomial of 4th order. Therefore, four poles have to be placed to achieve the desired dynamics and disturbance rejection. In the conventional PI controller only two controls exist: the proportional K_P and the integral K_I. This means placing all of the four poles is not possible. However, in [8] tuning methods were proposed to achieve a satisfactory results for certain ranges of inertias. For example, choosing the damping coefficients to be identical for systems with inertia ratios above 2 results in optimum trade-off between the dynamics and disturbance rejection.

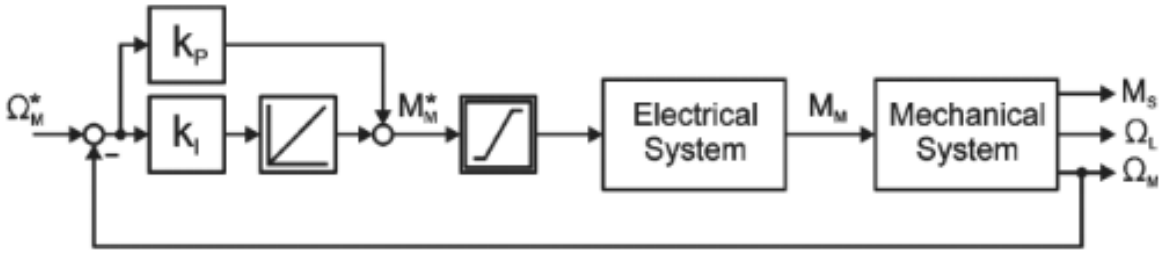

Figure 3-2 Conventional PI/PID controller

In other approaches with the conventional PID controller, for example in [[9] additional sensors are used to measure the load speed or torsional torque on the shaft to provide additional feedback for the system. However, the problems in using additional sensor are:

1- additional installation cost.

2- maintenance requirements

3- torque sensors are susceptible to noise and lack accuracy .

Instead of using sensors, with the help of observers the unmeasurable quantities can be estimated and used. In the next section we shall introduce them.

3.2 PI with DOB

One of the simplest solutions to torsional vibrations is to feedforward the torsional torque existing on the shaft which in some papers is referred to as the shaft torque[10]. By feedforwarding the torsional torque and multiplying it by the inverse of the torque constant (K_{tn}), the reference current will have additional component responsible for compensating the vibrations. However, the measurement of the shaft torque is not possible in some application as explained in the previous section. The approach is to use first order disturbance observer (DOB). It is basically an observer which estimates only one variable. In this case it estimates the disturbances on the motor side, which are often called internal (matched) disturbances. On the other hand, the disturbances on the load side are referred to as external (mismatched) disturbances, such as the load torque T_L. The internal disturbances consist of:

1- self inertia variation ΔJ_M

2-viscosity torque effect $D_M.\omega_M$

3- coulomb friction torque effect T_{fric}

4- variation of the torque coefficient ΔK_t

5- torsional torque T_s

The variation of the inertia and the torque coefficient are due to the modelling errors from the nominal values. i.e., they can be demonstrated as

$$\Delta J_M = J_M - J_{Mn} \text{ and } \Delta K_t = K_t - K_{tn}$$

Where J_M, and K_t are the actual values of the motor inertia and torque coefficient. J_{Mn} and K_{tn} are the nominal values accordingly.

The disturbance can be depicted in the following equation:

$$T_{dis} = \Delta J_M.\dot{\omega}_M + D_M.\omega_M + T_{fric} + \Delta K_t I_{ref} + T_s \quad (3\text{-}3)$$

where $\dot{\omega}_M$ is the motor angular acceleration, and I_{ref} is the motor reference current. The DOB in this case is simply realized by the difference between the nominal applied torque and the output torque, and then passed through a low pass filter to eliminate the high frequency measurement noise. The available output is the motor speed ω_M and the input is the reference current with the compensation component $I_{ref} + I_{comp}$. By studying the motor torque equation to reproduce the torsional vibration and other disturbances:

$$T_M = J_M.s.\omega_M + T_S \quad (3\text{-}4)$$

$$T_s = T_M - J_M.s.\omega_M \quad (3\text{-}5)$$

With the previous considerations the torsional torque is the disturbance or internal disturbance $T_s = T_{dis}$, and applied torque is $T_M = K_{tn}.(I_{ref} + I_{comp})$. Moreover, the torque constant and inertia values are the nominal values not the actual ones, now we have:

$$T_{dis} = K_{tn}(I_{ref} + I_{comp}) - J_{Mn}.s.\omega_M \tag{3-6}$$

The realization of equation (3-6) can be seen in Figure 3-3.

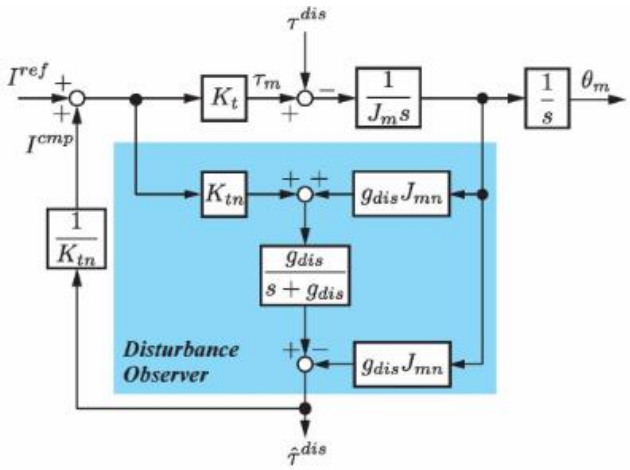

Figure 3-3 DOB implementation in the control scheme

The blue part of Figure 3-3 represents the described DOB Although it might seem different, in a closer study it is equivalent to:

$$T_{dis} = \frac{g_{dis}}{g_{dis}+s}\left[g_{dis}.J_{mn}.\omega_M + K_{tn}(I_{ref} + I_{comp})\right] - g_{dis}.J_{mn}.\omega_m$$

$$= \frac{g_{dis}}{g_{dis}+s}(g_{dis}.J_{mn}.\omega_M + K_{tn}(I_{ref} + I_{comp}) - \frac{(g_{dis}+s)}{g_{dis}+s}.g_{dis}.J_{mn}.\omega_m$$

$$= \frac{g_{dis}^2.J_{mn}.\omega_M + g_{dis}.K_{tn}(I_{ref} + I_{comp})}{g_{dis}+s} - \frac{g_{dis}^2.J_{mn}.\omega_m + s.g_{dis}.J_{mn}.\omega_m}{g_{dis}+s}$$

$$= \frac{g_{dis}.K_{tn}(I_{ref} + I_{comp}) - s.g_{dis}.J_{mn}.\omega_m}{g_{dis}+s}$$

$$= \frac{g_{dis}}{g_{dis}+s}(K_{tn}(I_{ref} + I_{comp}) - s.J_{mn}.\omega_m) \tag{3-7}$$

Where g_{dis} is the cutoff frequency of the low pass filter.

Comparing the last equation with (3-6), it has the same form with an additional part of the low pass filter. However, this method is not used often without an additional modification to make the suppression more effective as seen in the next section. The cutoff frequency is a critical design parameter in the DOB and a trade-off problem. Choosing g_{dis} too high will make the disturbance estimated and eliminated perfectly. However, this might pass the high frequency noise from the encoder due to the measurement noises.

3.3 Resonance Ratio Control (RRC)

RRC [11] is one of the widely used control methods for damping the torsional vibrations. RRC uses the same approach as in DOB. Nonetheless, in this method instead of using the total estimated disturbance in the feedforward compensation only a portion of it $(1 - K)$ is used. By only feedforwarding a portion of the disturbance, it modifies the motor's inertia in a virtual manner. Thus, the new equivalent inertia is:

$$J_M = J_{M0}/K \tag{3-8}$$

Where J_{M0} is the original nominal motor inertia. The inertia ratio has the new form:

$$R = \frac{J_L}{J_M} = \frac{J_L}{J_{M0}/K} = KR_0 \tag{3-9}$$

Therefore, it changes the resonance frequency to the following new value:

$$\omega_r = \sqrt{\frac{K_s}{J_L}\left(1 + \frac{J_L}{J_M}\right)} \tag{3-10}$$

The complete control scheme of RRC is in Figure 3-4.

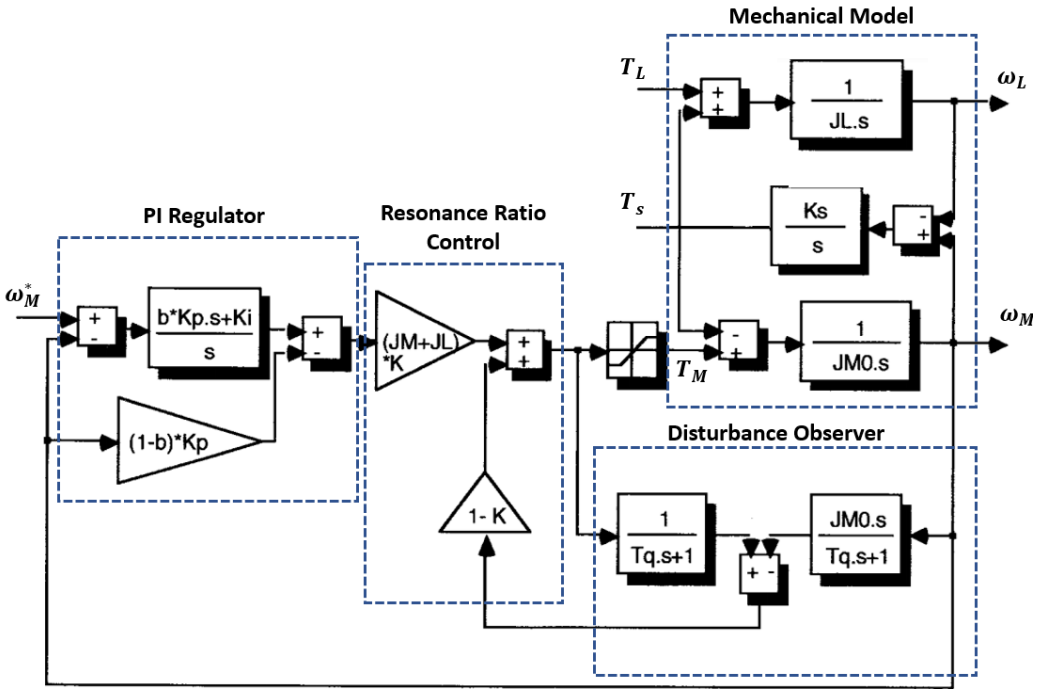

Figure 3-4 Resonance Ratio Control scheme

The challenge in choosing the value of the parameter K is keeping the peak gain value at the resonance frequency ω_r low, while having a reasonable value of T_q.

Notice the system is changed from Figure 3-4 to the following Figure 3-5.

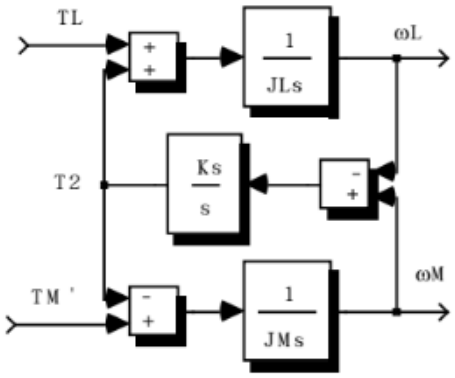

Figure 3-5 Equivalent two mass system after the usage of RRC

The described RRC is the fast type where the observation speed is set to maximum. In other words the time constant (T_q) of the filter in Figure 3-4 is too small. However, this can affect the vibration suppression for high frequency component. Moreover, it creates implementation problems since it cannot be realized in real applications with such high speed. A modified version which is referred to as slow RRC in [12], in this updated version the aforementioned downsides were tackled. The advantages of this scheme are the simplicity to implement since the DOB and RRC do not affect the original PI control design [13]. the problem in the RRC is that it is usually implemented in acceleration control where it requires high resolution encoder to realize it. Additionally, RRC does not consider higher order resonance frequencies other than the two-mass resonant system. Finally, the uncertainties in the system of the parameters (the inertia ΔJ_M, and the torque constant ΔK_t) deteriorate the control system performance.

3.4 PI State-space controller with an observer

As mentioned in the previous section PI controller lacks the ability to damp the torsional vibration effectively without any additional feedbacks. As an alternative to the conventional PI controller there is the PI state space controller [14][7][15], where all the states of the system are used in the feedback and each state has its own feedback gain, which should be implemented in the controller system with the appropriate gains. The PI state-space controller is implemented as seen in Figure 3-6 PI state space controller. The control scheme uses four states of system: motor speed ω_M, load speed ω_L, torsional torque (shaft torque) T_s and the motor torque T_M.

The additional feedbacks enable us to freely place the poles of the system and therefore high damping of the torsional vibrations and dynamic of the system is achieved.

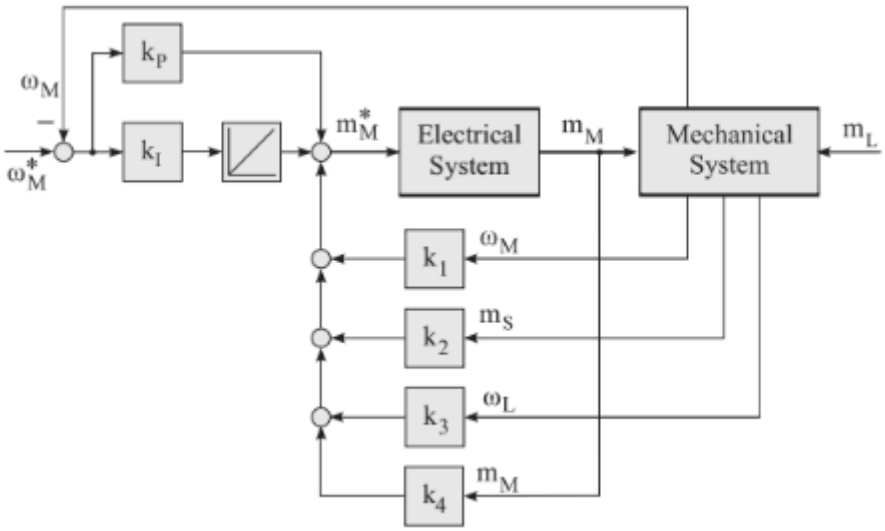

Figure 3-6 PI state space controller

The gain parameters $k_1, k_2, k_3, k_4, k_I, and\ k_p$ are found according to the damping coefficient and the natural frequencies using the pole placement method. The transfer function of the PI space controller in Figure 3-6 is referred to as 5th order. The most complicated task in the design of the state space controller is to choose suitable control coefficients. However, as mentioned in the previous section, the load speed ω_L and the torsional torque T_s are not available due to difficulties coming with those sensors. A common solution is to utilize a state observer, such as the Luenberger observer.

The observer has a similar formulation as the state space system. It uses the available or measured state variables which in the given case are motor speed ω_m and motor torque T_M. The motor speed is available from the encoder, and the motor torque is available from the quadrature current applied by electrical system multiplied by the torque coefficient.

Instead of having control gain parameters in the observer, the design parameters are the gain matrix. The pole placement method can be used to select the gain values. The poles of the observer should be chosen in such a way to ensure 2 to 3 times faster dynamics than the control system. However, similar to the cutoff frequency of the DOB, the task is to choose the gain matrix not too high, which amplifies the noise of the measurements, neither too low, which slows down the convergence of the estimates. Implementing the observer in Figure 3-7 is straight forward. As mentioned, it takes the available states as an input and gives the estimates of the ω_L and T_s as an output.

One of the advantages of the observer is that it acts as a patch to the control system. In other words, it does not affect the design of the baseline control system, thus all of the previous considerations are not affected [16].

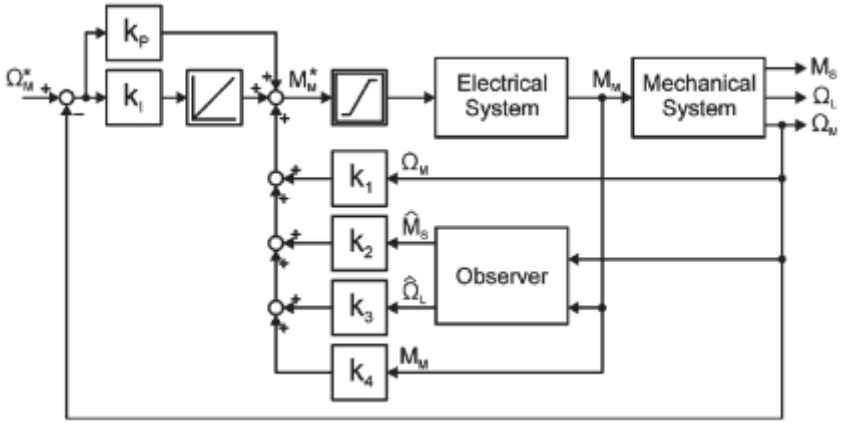

Figure 3-7 PI state space controller with an observer

This control achieves a good vibration suppression and excellent stability in comparison to the conventional PI control scheme. However, the trade-off is the complexity of the design, and additional computation power since it is necessary to design an observer to estimate all the state variables of the system.

A more robust control design which achieves a better performance under variation of the load, is the usage of the extended state observer (ESO) [17][18]. The difference between extended state observer and the mentioned state observer is the estimation of the load torque as-well. ESO has the same structure of the normal state observer. However, it treats the disturbances as an extra state variable. In our case the disturbance is the load torque T_L.

The control scheme is shown in Figure 3-8, the estimated disturbances and uncertainties are used to compensate the system in a feedforward manner.

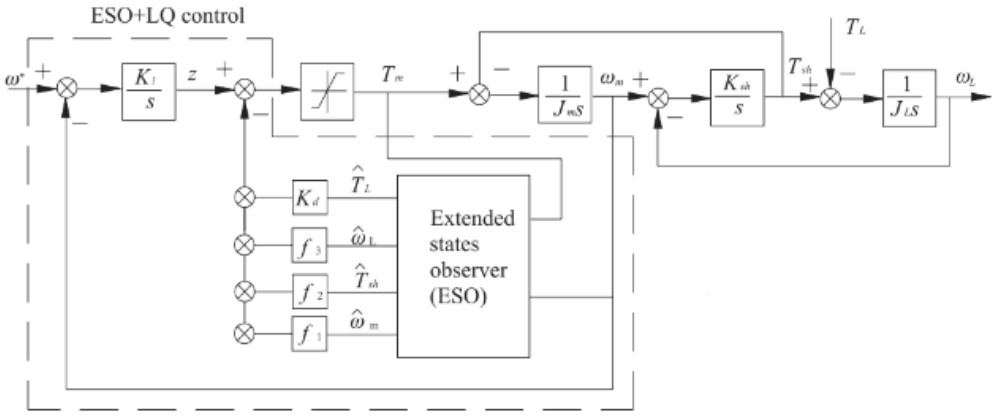

Figure 3-8 the usage of ESO

In the study [17], extra steps have been taken by trial and error to make the ESO more efficient by implementing a nonlinear function in the observer. Moreover, instead of using the mentioned pole-placement to design the state space controller, a linear quadratic regulation (LQR) was used. LQR requires the knowledge of the weighting matrices of Q and R in order to optimize the choice of the gain parameters to achieve the required design requirements with the minimum power. With the appropriate design steps, the control scheme in Figure 3-8 achieves better performances in vibration suppression than the normal observer in the aspect

of rejection of disturbances under load variation and to robustness against parameter variations. The system was tested with sinusoidal torque disturbance and 100% change in the load inertia J_L.

An even further upgrade to the previous methods, is the usage of the Kalman filter [19]. Kalman filter enhances the control scheme robustness and it is used when the system is characterised by process noise and subjected to measurement noises. The problem with Luenberger observer is that it cannot provide satisfactory estimation in systems with high parameter variations and measurement noises. Estimation methodology is based on prediction of the state variables and then updating the gains of the observer online. The complication in Kalman filter is that the covariance matrices of the process noise and measurement noise must be defined beforehand. These matrices, usually referred to as R and Q, are often determined for each specific system by trial and error, which means it requires the knowledge of these disturbances behaviours. Moreover, the computation time compared to the previous method is higher. Similar method is presented in [20], where the load inertia is also estimated by using Kalman filter and updated with each step. The control scheme is no different from the previous one as seen in Figure 3-9.

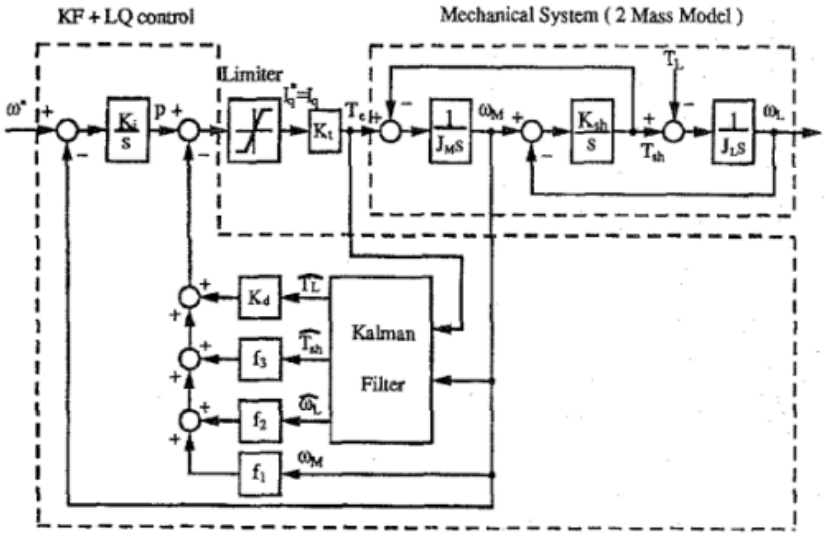

Figure 3-9 Kalman filter based control scheme

A final method which combines the use of DOB and state observer is analysed in [21], in which the DOB is used to estimate the disturbances separately and then is being fed to a normal state observer. This method is claimed to enhance the observer capability to exactly determine the value of the states.

In conclusion, before choosing the optimum control scheme for the suppression of the torsional vibration, three aspects must be considered:

1- How much disturbances are acting on the system,

2- The uncertainties existing in the system,

3- Measurement noise.

In case of no disturbances acting on the system and no existing uncertainties, the right choice is to use state space controller. In contrast, if there is a changing load torque as an external disturbance, then a DOB or ESO are more suitable. Finally, in case of system parameters variations and high measurements noises Kalman filter must be used.

Chapter 4: Electrical model of the system

In this chapter the machine under study, which is the axial flux permanent magnet machine (AFPM), will be described through its mathematical model. In the first section a brief description of the machine is reported with a comparison to the conventional radial flux permanent magnet machine (RFPM). The system's electrical model is derived analytically in the second section. Finally, in the last section a method that demonstrates and pinpoints the potential resonance points is introduced with Campbell diagram and constructed for our specific system.

4.1 Axial Flux Permanent Magnet Machine

The earliest invented electrical machines were in fact AFPM. However they were abandoned later on due to several reasons such as[22]:

- Strong axial magnetic attraction force between the stator and rotor.
- Manufacturing difficulties, such as cutting slots in laminated cores and other methods of making slotted stator cores.
- High costs involved in manufacturing the laminated stator cores.
- Difficulties in assembling the machine and keeping the uniform air gap.

The breakthrough in high quality energy density of the PM and their availability with the price decline is one of the reasons of bringing the old technology back. Axial Flux machine types are classified in three main categories where the last one is the most exploited type:

- PM DC commutator machines
- Induction machines
- PM brushless synchronous DC and AC machines

The AFPM DC commutator machine has the disadvantages over the conventional RFPM dc brushed machine in the terms of size and durability. The realization of the induction machine is a difficult task due to the complexity of the cage manufacturing. The AFPM brushless synchronous machine is the most used type among the mentioned categories. It follows the same topology as the RFPM machine where the DC type generates a trapezoidal EMF waveform and is operated with rectangular current waveform. The AC type, instead, generates a sinusoidal EMF waveform and it is operated with sinewave currents. The interest for AFPM machines is growing in the recent years due to their advantages over the RFPM machines in the terms of power density and compact size. This growth is especially focused on the applications in automobiles and distributed generations.

Similar to the RFPM machines, the AFPM has a rotor, stator, and a shaft. However, the design differs in the sense of the realization of orienting the magnetic flux. In RFPM the flux is radially oriented from the PM to the outer stator or in the case of outer rotor machines the flux is radially oriented outwards. In AFPM the magnetic flux is axially to the stator. In Figure 4-1 the flux directions are illustrated for the two machines.

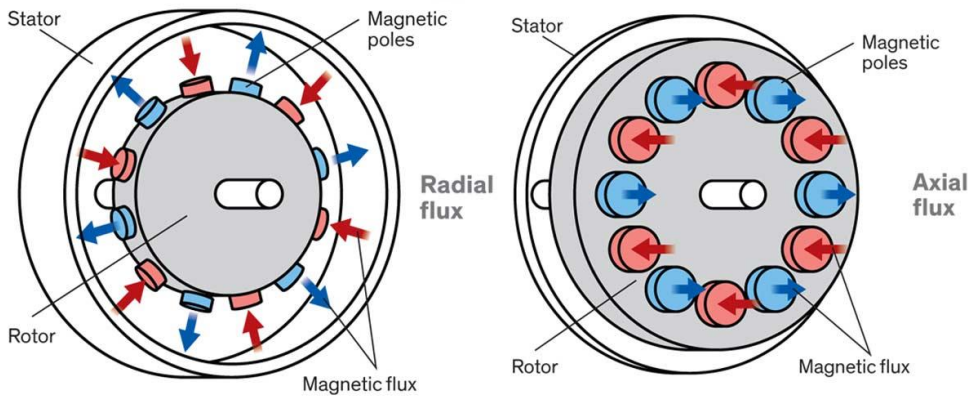

Figure 4-1 Flux directions of the RFPM (left) and AFPM (right)

The simplest structure of the AFPM is **single-sided AFPM** seen in Figure 4-2, where there are one rotor and one stator. However, the simple configuration of the AFPM machine fails at high power levels, since surface between the rotor and shaft becomes smaller as the power increases. Hence, increasing the power level of the machines requires the additional modules.

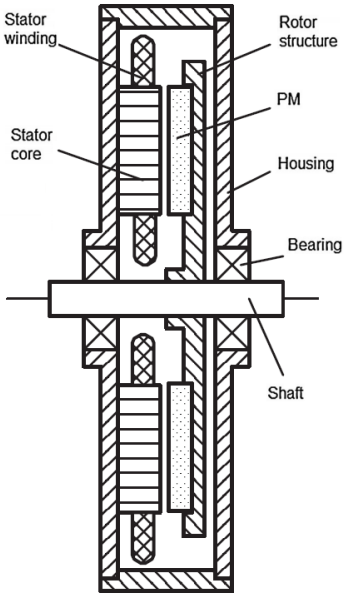

Figure 4-2 Structure of single sided AFPM machine

Adding additional module from the single-sided AFPM can be done in different ways, with a possibility of adding an extra rotor or stator. Adding extra rotor results in **double-sided internal stator AFPM**. On the contrary, the **double-sided internal rotor AFPM** machine has two stators and a sandwiched rotor. Double-sided internal stator type has better performance in terms of winding utilization than the first choice but at the cost of the usage of additional PMs. The two configurations with their compositions are represented in Figure 4-3.

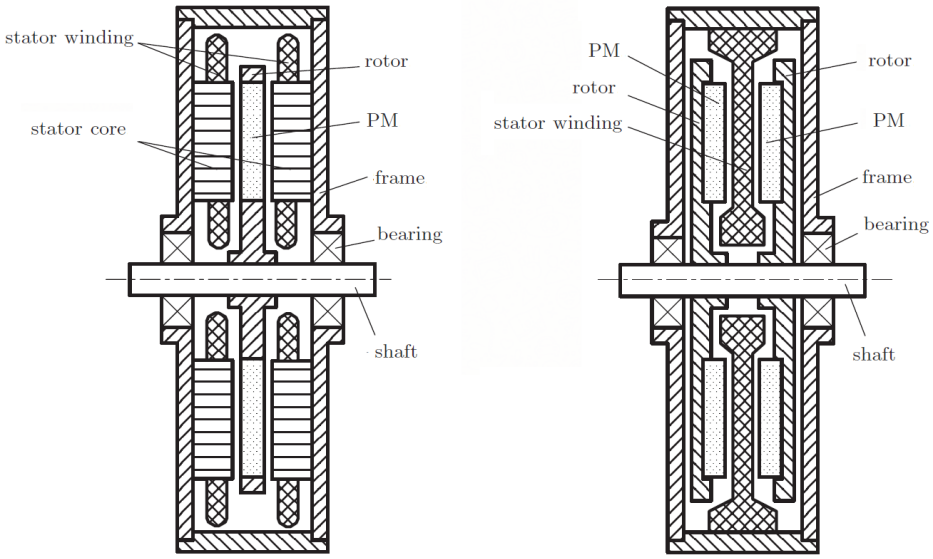

Figure 4-3 double-sided AFPM machine internal rotor (left), internal stator (right)

When the power requirement is even higher, the **multi-modular AFPM** is used where the number of modules are referred to as j. In the multi- modular machine, there exists j stators and $j + 1$ rotors. All the three phase terminals coming from the stator can be connected in series or in parallel depending on the machine operation. For example, Figure 4-4 represents a three stage AFPM with three stators and four rotors [23].

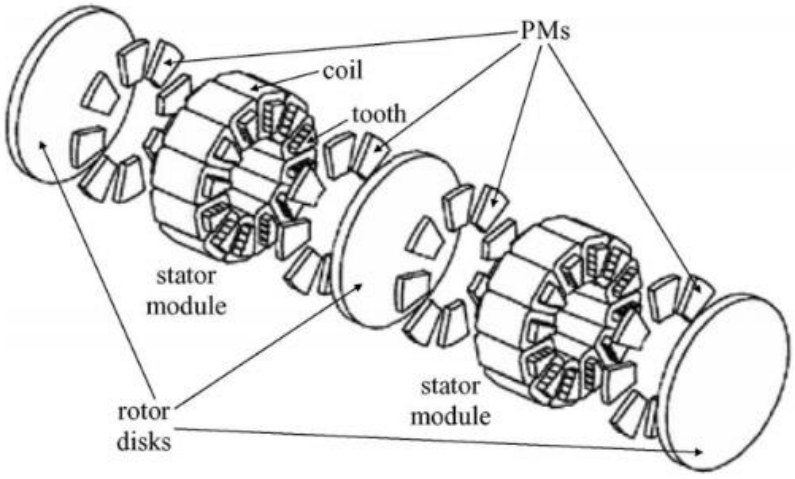

Figure 4-4 Exploded sketch of a portion of the a three stage AFPM machine

Putting the AFPM machine in comparison with the RFPM machine, the former has the advantages of better ventilation and cooling due to the fact that the machine diameter is greater than the shaft diameter. The ratio difference can be noticed from the previous figures of the AFPM. This is not the case for the RFPM machine where the heat is transferred from stator winding to the core and then to the frame. It needs forced cooling system. In addition, as mentioned in the previous section, the topology of an AFPM is ideal to design a modular machine where the machine system can be adjusted to meet specific criteria. The large diameter of the core of the AFPM machine allows the machine to accommodate large number of poles, which makes it suitable for low and medium speed applications as it can be used as a generator in wind turbines.

4.1.1 The electrical model of the AFPM machine

In this section the stator voltage and torque equations of the electrical model of the synchronous machine are briefly described and then used to build the model in Simulink. Since the electrical model of the AFPM is identical to that of the conventional RFPM machine, the same approach is followed.

4.1.1.1 Stator voltage equation of the synchronous machine

By using Kirchhoff law, the three phase voltage equations for the stator windings can be written taking into account the Lenz law:

$$v_{sk} = R_s i_k + \frac{d\phi_{sk}}{dt} \tag{4-1}$$

Where the magnetic flux ϕ_{sk} for $k = 1,2,3$ can be described as:

$$\frac{d\phi_{sk}}{dt} = \frac{l_s di_k}{dt} + \frac{d\phi_{mk}}{dt} \tag{4-2}$$

The first part on the right-hand side ($l_s i_k$) represents the leakage flux for each winding, and ϕ_m for the mutual flux. The complete evaluation of the previous expression is out of this thesis scope. However, it should be noted it was done by the author in [24] while assuming infinite permeability for the ferromagnetic materials for the stator and rotor. Hence, there are no magnetomotive force drops in the iron parts of the machine. The direct and quadrature components of the stator voltage based on the rotor reference frame are represented in Figure 4-5.

$$v_{sd} = R_s \mathrm{i}_{sd} + L_d \frac{d\mathrm{i}_{sd}}{dt} - \frac{p}{2}\omega_r \mathrm{i}_{sq} L_q \tag{4-3}$$

$$v_{sq} = R_s \mathrm{i}_{sq} + L_q \frac{d\mathrm{i}_{sq}}{dt} + \frac{p}{2}\omega_r \phi_M + \frac{p}{2}\omega_r \mathrm{i}_{sd} L_d \tag{4-4}$$

Where p is the number of poles, and ω_r is the electrical speed of the rotor. The PM flux is noted by ϕ_M. L_d and L_q represent the direct and quadrature inductance components of the PM machine. As for the case of the isotropic machine, we have the case where inductances are equal $L_d = L_q = L_s$. The stator voltage equations for the isotropic machine becomes:

$$v_{sd} = R_s \mathrm{i}_{sd} + L_s \frac{d\mathrm{i}_{sd}}{dt} - \frac{p}{2}\omega_r \mathrm{i}_{sq} L_s \tag{4-5}$$

$$v_{sq} = R_s \mathrm{i}_{sq} + L_s \frac{d\mathrm{i}_{sq}}{dt} + \frac{p}{2}\omega_r \phi_M + \frac{p}{2}\omega_r \mathrm{i}_{sd} L_s \tag{4-6}$$

In order to be able to build the electrical machine model in Simulink, the stator flux equation must be identified. Hence, it is useful to recall the vector stator voltage equation for the isotropic machine:

$$\boldsymbol{v}_s = R_s \mathbf{i}_s + \frac{p}{2}\phi_s + j\omega_r \phi_s \tag{4-7}$$

Where the bold notation for the stator quantities of the voltage and current represents the vector space quantities referred to the rotor frame.

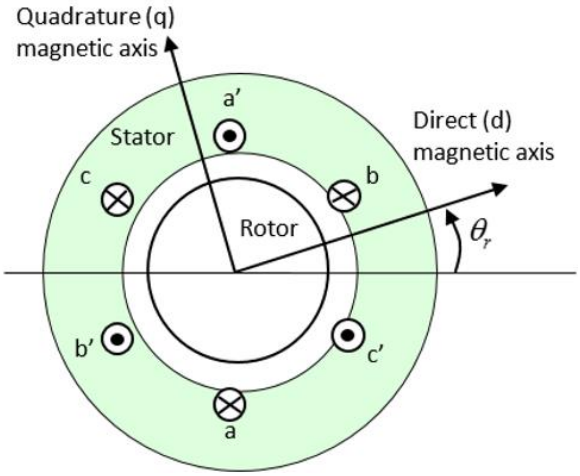

Figure 4-5 Direct and quadrature axis on the rotor reference frame

The stator flux of the machine is represented by ϕ_s variable and it is given by the sum of the PM flux and the flux produced by the stator windings as in:

$$\begin{aligned} \boldsymbol{\phi_s} &= \phi_M + L_s \mathbf{i}_s \\ \phi_{sd} + j\phi_{sq} &= \phi_M + L_s i_{sd} + jL_s i_{sq} \end{aligned} \tag{4-8}$$

4.1.1.2 Torque equation of the PM synchronous machine

As it regards the torque inside the machine, the derivation can be done by using Lorentz force

$$T = -\frac{p}{2}\frac{D}{2}\ell_{ax}\int_0^{\frac{2\pi}{p}} B(\alpha)\Gamma_s(\alpha)d\alpha \tag{4-9}$$

The details of the calculations are reported in [24], where the final formula for the torque equation for PM machine is given by:

$$T = \frac{1}{2}p\mathbf{i}_{sq}\phi_M + \frac{1}{2}p\frac{L_q - L_d}{2}2(\mathbf{i}_{sd}\mathbf{i}_{sq}) \tag{4-10}$$

And for the isotropic machine, the expression is simplified to

$$T = \frac{1}{2}p\Im m\{\mathbf{i}_s\boldsymbol{\phi_s}\} \tag{4-11}$$

Which leads to the control of the isotropic synchronous machine by making the quadrature component of the i_{sq} be the sole responsible for the torque production without the direct component i_{sd} as in:

$$T = \frac{1}{2}p\mathbf{i}_{sq}\phi_M \tag{4-12}$$

The data of the electrical parameter of the machine which will be used for analysis in this thesis are found in Table II.

In order to simulate the system with the proposed solution for the torsional problem, a Simulink model of the reviewed electrical model has been set, the details of this model is reported in Appendix B.

4.2 Pulse width modulation DC/AC inverter

The electrical machine described in the previous section can be driven by variable frequency drives (VFDs), such as square wave modulation inverter or a typical three-phase Pulse Width Modulation (PWM) DC/AC inverter. The inverter used in this study is supplied by an ideal DC source as shown in the configuration of Figure 4-5.

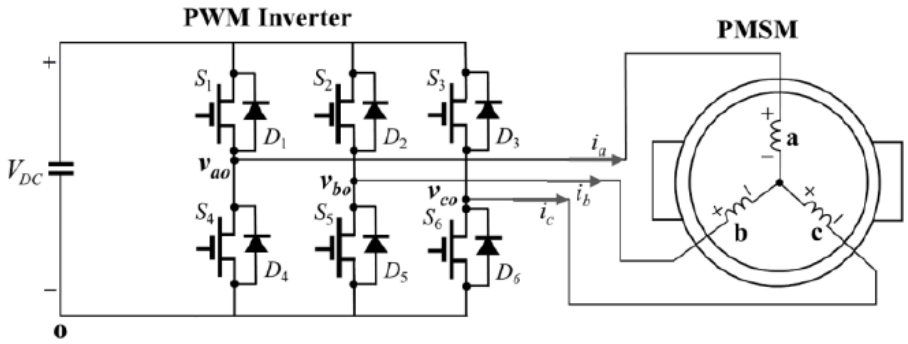

Figure 4-6 PWM inverter supplying a PMSM

As described in the introduction, the VFDs are source of the harmonics. The output voltage of the VFDs is characterised by harmonics contents superimposed to the fundamental frequency. The harmonic order for a square wave modulation inverter can be given in a closed form as in [25]:

$$n\omega_e \qquad n = 6l \pm 1, \text{ with } l = 1,2,3,\ldots \tag{4-13}$$

Where ω_e is the fundamental frequency of the output voltage or current. On the other hand, the harmonics found in the output of a PWM inverter are proportional to the frequency modulation index, which denotes the ratio of the carrier frequency to the fundamental frequency, i.e., $m_f = f_c/f_o$. Where f_c denotes the switching frequency and f_o is the inverter output frequency, the order of harmonics are given as [24]:

$$\begin{aligned} &m_f, m_f \pm 2, m_f \pm 4, m_f \pm 6, \ldots \\ &2m_f \pm 1, 2m_f \pm 3, 2m_f \pm 5, 2m_f \pm 7, \ldots \\ &3m_f, 3m_f \pm 2, 3m_f \pm 4, 3m_f \pm 6, \ldots \\ &4m_f \pm 1, 4m_f \pm 3, 4m_f \pm 5, 4m_f \pm 7, \ldots \end{aligned} \tag{4-14}$$

The previous expression is referred to as the baseband and sidebands harmonics contents which are the main focus in this thesis. Additional harmonics can appear from VFDs and specifically for the PWM inverters due to the non-integer modulation index value or the nonideal DC source. These harmonics are referred to as the inter-harmonics, which have insignificant amplitudes compared to the rest of harmonics and are not considered in the analysis of this thesis. Since the electromagnetic torque in the electrical machine is a consequence of the interaction of the PM flux and the quadrature current component in air the gap of the machine described by equation (4-11), the torque harmonics order can be found. The baseband current harmonics given in the expression (4-13) are of the positive and negative sequence component,

and give rise to a torque component at one frequency located at $n = 6l\omega_o$ with an amplitude of their average value. An illustration of the torque harmonic generation is shown in Figure 4-7.

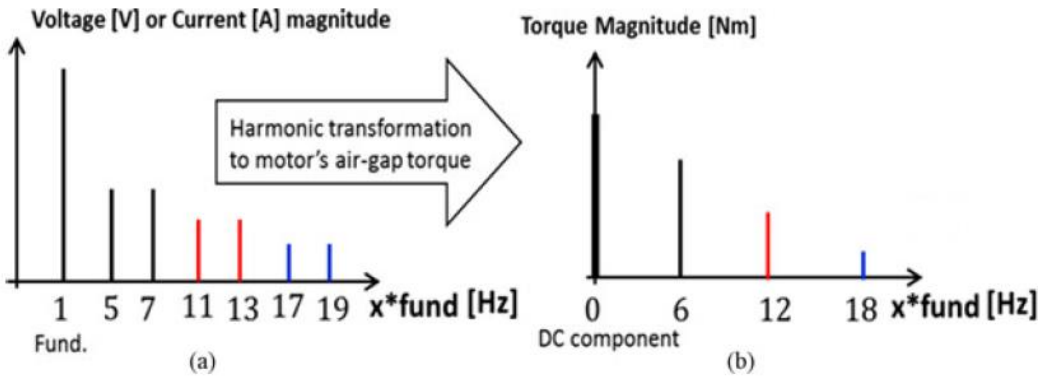

Figure 4-7 Current and torque harmonics in case of a square wave modulation

As for the PWM case the torque harmonics take the form:

$$\begin{matrix} m_f \pm 3 \\ 2m_f \\ 3m_f \pm 3 \\ 4m_f \end{matrix} \tag{4-15}$$

In a typical PWM converter the switching frequency (f_s) is not always proportional to the operating frequency (f_o), but it is set to be constant at the beginning or at the starting of the machine and then it increases linearly as the motor accelerates. Such behaviour can be illustrated in Figure 4-8. In this thesis the software simulation is done to test the proposed solution of the torsional vibrations, in order to implement the suppression method to an actual laboratory setup. The laboratory setup consists of two machines that mimic the operation of an AFPM, where the coupling is realized through some springs to have low value of stiffness. This implies relatively large torsional oscillations and a low resonant frequency (2-17), which can be crossed only at low machines speeds (then at low frequencies). For our particular system the switching frequency lower limit is set at $4Hz * m_f$ with $m_f = 15$.

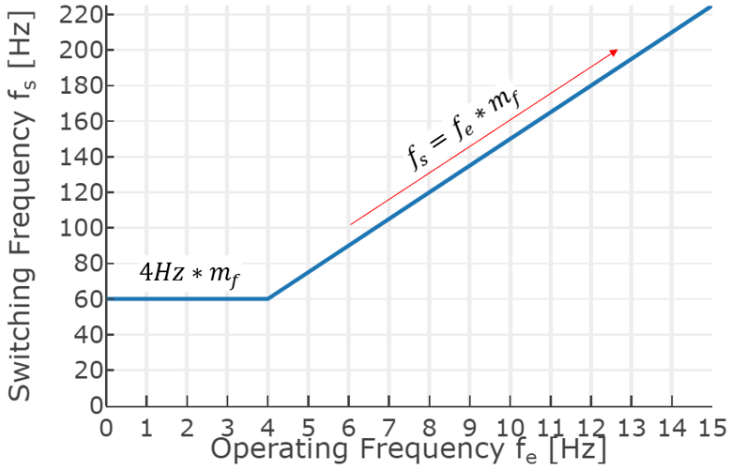

Figure 4-8 Switching frequency and operating frequency relationship

The aforementioned PWM inverter is modelled into Simulink software reported in Appendix B, the details of this implementation are given in [4].

4.3 Campbell diagram

Campbell diagram is a useful tool that pinpoints the potential resonance occurrence between the electrical and mechanical system. In the diagram the natural frequencies of the mechanical system are plotted as horizontal lines. The operating speed range is designated by vertical lines, which limits the active regions at two sides of the diagram. On one hand, the lower limit is due to the minimum switching frequency of the VFD which makes the harmonics excitors in this region inactive. On the other hand, the upper limit is the rated speed of the machine. The slope lines represent the system harmonic potential excitors [6]. System harmonic can be the result of other components in the plant as explained at the introduction in section 0. However, the only harmonic excitors considered in this study are the torque harmonics produced by the VFD.

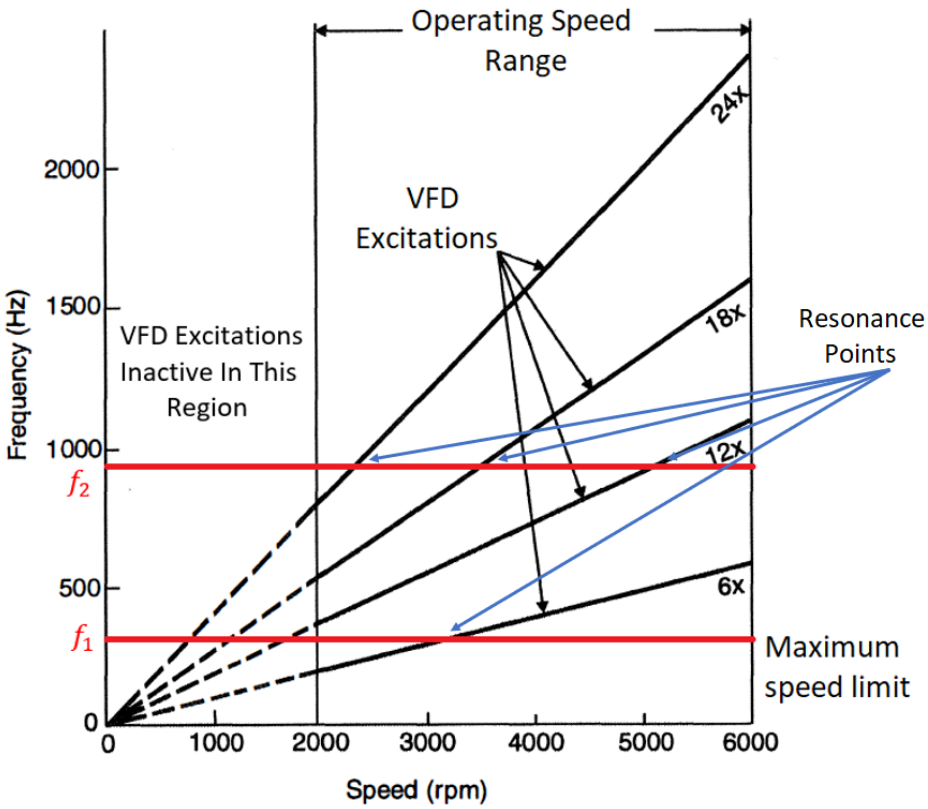

Figure 4-9 Campbell diagram regions, excitors, and resonance points

Finally, the intersection between the slope harmonic lines and the natural frequencies are the potential system resonance. Figure 4-9 shows a typical Campbell diagram with two different natural frequencies at f_1 and f_2 indicated by red horizontal lines for a three-mass system, resulting in four potential resonance intersections from four different harmonic orders.

With the concept being introduced of Campbell diagram, it is now useful to build it for our system. With the torque pulsation harmonics order identified in 4.2 with chosen modulation index ($m_f = 15$), as well as the resonance frequency of the mechanical system section 2.1, one more ingredient is needed to find the link between the electrical excitation frequencies and the

mechanical speed. Since a synchronous machine is analysed, the electrical frequency relationship with the mechanical speed is:

$$f_e = \omega_M \cdot \frac{p}{4 \cdot \pi} \tag{4-16}$$

Where ω_M is the motor speed in rad/s, and p is the number of poles. By using MATLAB code given in Appendix A-1, the constructed Campbell diagram for our system is shown in Figure 4-10.

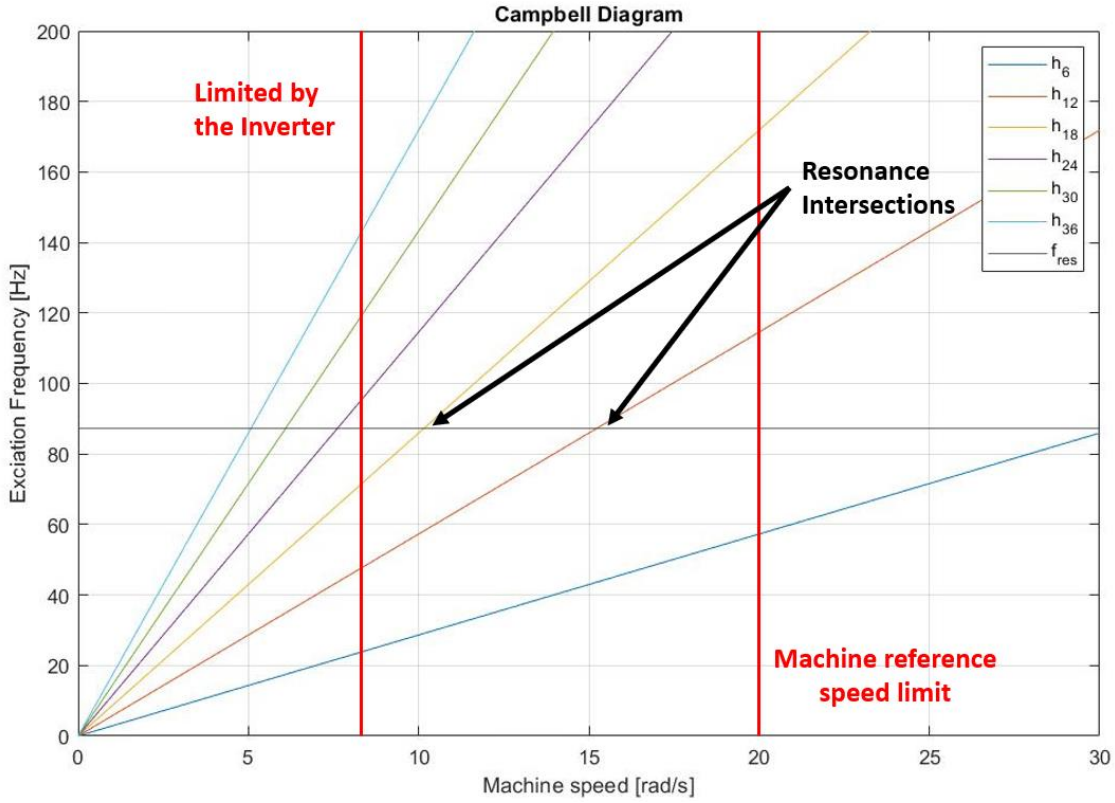

Figure 4-10 Campbell diagram for the system under study

The diagram shows two potential resonance points that resulted from the twelfth and eighteenth harmonic of the electromagnetic torque corresponding to the mechanical speeds: $15.25\,rad/s$ and $10.16\,rad/s$ or in electrical corresponding frequencies: $7.28\,Hz$ and $4.85\,Hz$,respectively. Regarding to the harmonics order of $h = 36,\ 30\,,24$ there is indeed an intersection with the mechanical natural frequency, but as mentioned in section 0 the VFD switching frequency has set a lower limit for the switching frequency at $4Hz$ ($\omega_m = 8.38\,rad/s$) which makes them inactive and the resonance is avoided. Finally, the harmonic $h = 6$ is noticeably way far from the machine rated speed.

Chapter 5: Design of the control system

In this chapter different the control methods are explained in detail to approach the problem of the torsional vibrations in axial machines. In the first section a review of proportional integral (PI) controllers is conducted, and a simple tuning method is explained and built for the base PI regulators of the control system. The main contribution in this work starts with the concept of disturbance observers-based control (DOBC) systems in the second section of this chapter, where the methodology of building such systems along with the design of two types of the disturbance observers are reported.

5.1 Proportional Integral controller

PI controllers are the most conventional to be used in any industry due to their intelligible structure and robustness. However, the downside of the PI controllers is the performance under uncertainties and external disturbances which is the focal point of this study. In this thesis a frequency domain approach is followed to tune the PI parameters based on phase margin criterion to assure robustness. The general form of the PI controller transfer function is:

$$G_{PI}(s) = K_p + \frac{K_i}{s}$$

where the proportional gain term is noted by K_p, which is responsible for generating a faster tracking response and smaller offset in the presence of disturbances. However, to ensure mitigation of disturbances a high gain must be used which requires a high amount of power. The integral control $\frac{K_i}{s}$ is the complement to the proportional term and it is implemented to remove offset disturbances and uncertainties. However, the integral control has poor performance in the presence of time-varying disturbances and uncertainties.

5.1.1 Current controllers

Firstly, the current controllers are designed for the PM synchronous machine. As it was discussed in the last section, the current is divided into two parts: direct and quadrature component represented by the equations (4-3) and (4-4) respectively. The equations are decoupled, and they can be controlled via two different PI controllers (in addition to some compensation terms illustrated in the next analysis). Recalling the direct equation and transferring it into the Laplace domain results:

$$\boldsymbol{v_{sd}} = r_s \mathbf{i}_{sd} + L_d \frac{d\mathbf{i_{sd}}}{dt} - \frac{p}{2}\omega_r \mathbf{i_{sq}} L_q$$

$$\boldsymbol{V_{sd}}(s) = \mathbf{I_{sd}}(s)(r_s + L_d s) - \frac{p}{2}\omega_r L_q \mathbf{I_{sq}}(\boldsymbol{s})$$

The previous expression can be split into two parts; the first part noted by $G_{Isd}^{-1} = (r_s + L_d s)$, and the second part as the coupling term. Then we have:

$$G_{Isd}(s) = \frac{\mathbf{I_{sd}}(s)}{\boldsymbol{V_{sd}}(s)} = \frac{1}{L_d s + r_s} \qquad (5\text{-}1)$$

$$C_{Isd}(s) = -\frac{p}{2}\omega_r \mathbf{I_{sq}} L_q \tag{5-2}$$

Equation (5-1) is used to describe the direct part of the electrical machine current and for designing the current regulator. In addition to the aforementioned equation the coupling term in (5-2) is used as compensation term. However, if the control scheme is left without compensating the coupling term, it will work and produce acceptable responses due to the integral term from the PI controller which will compensate the offset error. However, it should be noted that if the system starts from a different point than zero it might lead to undesired effects. For example, at starting of the machine the integral part of PI regulator gives a small output which can be lower value than the back electromagnetic force of the machine and as a consequence negative torque will be generated due to the negative value of the current.

In addition to the previous model equations, a first order delay term is also included in the current loop to describe the effect of the inverter as in the following equation:

$$G_{inv}(s) = \frac{1}{1 + T_{inv}s} \tag{5-3}$$

Where the switching frequency is represented by f_s and $T_{inv} = \frac{1}{f_s}$

Referring to the control scheme in Figure 5-1, the open-loop transfer function without the controller has the following form:

$$\begin{aligned} L_{i_{sd}}(s) &= G_{Isd}(s)G_{inv}(s) \\ &= \left(\frac{1}{L_s s + r_s}\right)\left(\frac{1}{1 + T_{inv}s}\right) \end{aligned} \tag{5-4}$$

Including the controller, we have:

$$\begin{aligned} L_{PI_{Isd}}(s) &= G_{PI_{Isd}}(s)G_{Isd}(s)G_{inv}(s) \\ &= \left(K_{pI} + \frac{K_{iI}}{s}\right)\left(\frac{1}{L_s s + r_s}\right)\left(\frac{1}{1 + T_{inv}s}\right) \end{aligned} \tag{5-5}$$

The closed-loop transfer function takes the form:

$$F_{i_{sd}}(s) = \frac{L_{i_{sd}}(s)}{1 + L_{i_{sd}}(s)} \tag{5-6}$$

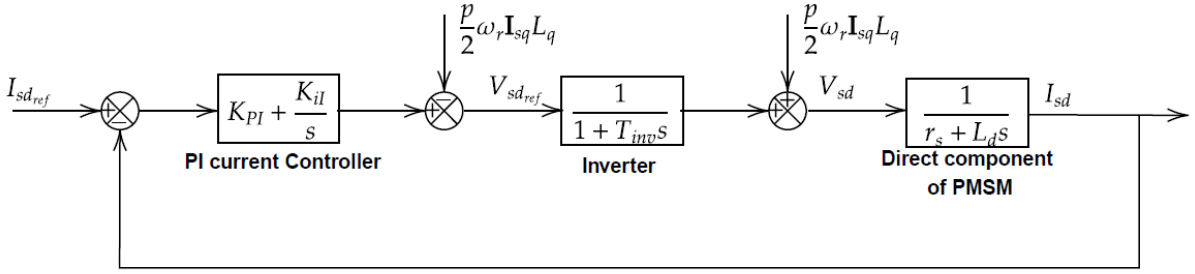

Figure 5-1 Control scheme of the PMSM direct current component

Similarly, transferring the quadrature voltage component equation (4-6) results in:

$$\boldsymbol{v_{sq}} = r_s \mathbf{i_{sq}} + L_q \frac{d\mathbf{i_{sq}}}{dt} + \frac{p}{2}\omega_r \phi_M + \frac{p}{2}\omega_r \mathbf{i_{sd}} L_d$$

$$\boldsymbol{V_{sq}}(s) = \mathbf{I_{sq}}(s)(r_s + L_q s) + \frac{p}{2}\omega_r \phi_M + \frac{p}{2}\omega_r L_d \mathbf{I_{sd}}(s)$$

The first part of the expression can referred to as $G_{Isq}(s)^{-1} = (r_s + L_q s)$, and the rest of the expression as a coupling term, then:

$$G_{Isd}(s) = \frac{\mathbf{I_{sq}}(s)}{\boldsymbol{V_{sq}}(s)} = \frac{1}{L_q s + r_s} \tag{5-7}$$

$$C_{Isq}(s) = \frac{p}{2}\omega_r \phi_M + \frac{p}{2}\omega_r \mathbf{I_{sd}}(s) L_d = \frac{p}{2}\omega_r (\phi_M + \mathbf{I_{sd}} L_d) \tag{5-8}$$

The block diagram of the PI regulator for the quadrature current component of PMSM is shown in Figure 5-2.

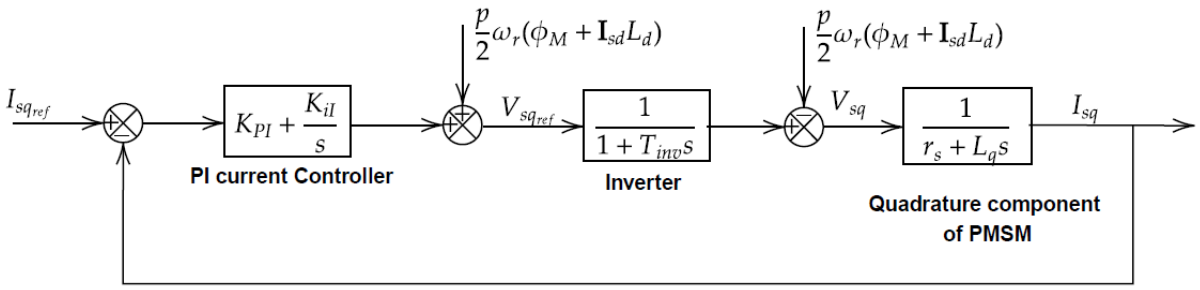

Figure 5-2 Control scheme of the PMSM quadrature current component

Since the machine is isotropic ($L_q = L_d = L_s$), tuning the PI current regulators for the direct and quadrature current components follows the same procedure and leads to the same results. In addition, having different compensation terms does not affect the parameters selection process. Choosing the values of K_{PI} and K_{iI} is done by ensuring the open-loop system has a positive phase margin and therefore the closed-loop system is stable. . The choice is done by the help of MATLAB code reported in Appendix A-3. The first step is to choose the appropriate cutoff frequency for the controller several times higher than the system bandwidth to avoid the risk of attenuation in the response. From the characteristics of the system parameters from the Table II and equation (5-2), the bode plot is shown in Figure 5-3.

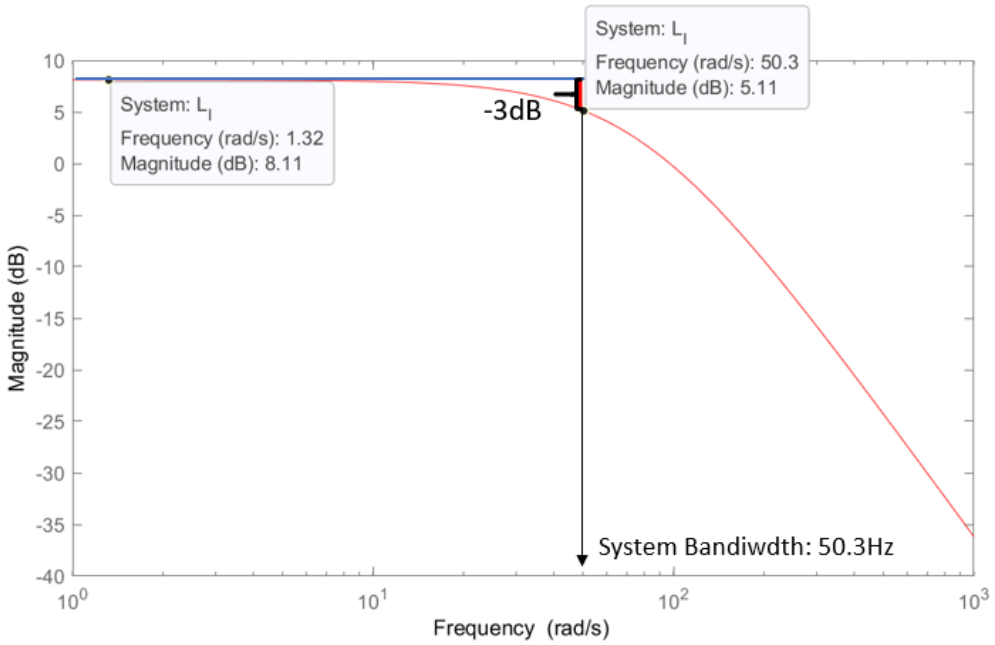

Figure 5-3 Open-loop transfer function of the electrical model of the system under control by the PI current regulator

The bandwidth of the system under control is found to be $BW_I = 50.3\ rad/s$, then the current closed-loop cutoff frequency is chosen to be $\omega_{cI} = 80 rad/s$. The phase margin is chosen $\phi_I = 70^o$. Appendix A section: "Current and speed PI-regulators m-files" reports the details of the tuning, from which it is found that the suitable parameters of the PI current regulator are:

$$K_{PI} = 0.7604\ \Omega$$
$$K_{II} = 20.73\ \Omega/s \qquad (5\text{-}9)$$

Checking the design values from the open- and closed-loop transfer functions frequency response by plotting the bode diagram of the equations (5-5) and (5-6) is shown in Figure 5-5. It can be noticed the phase margin criterion is fulfilled at the chosen cutoff frequency.

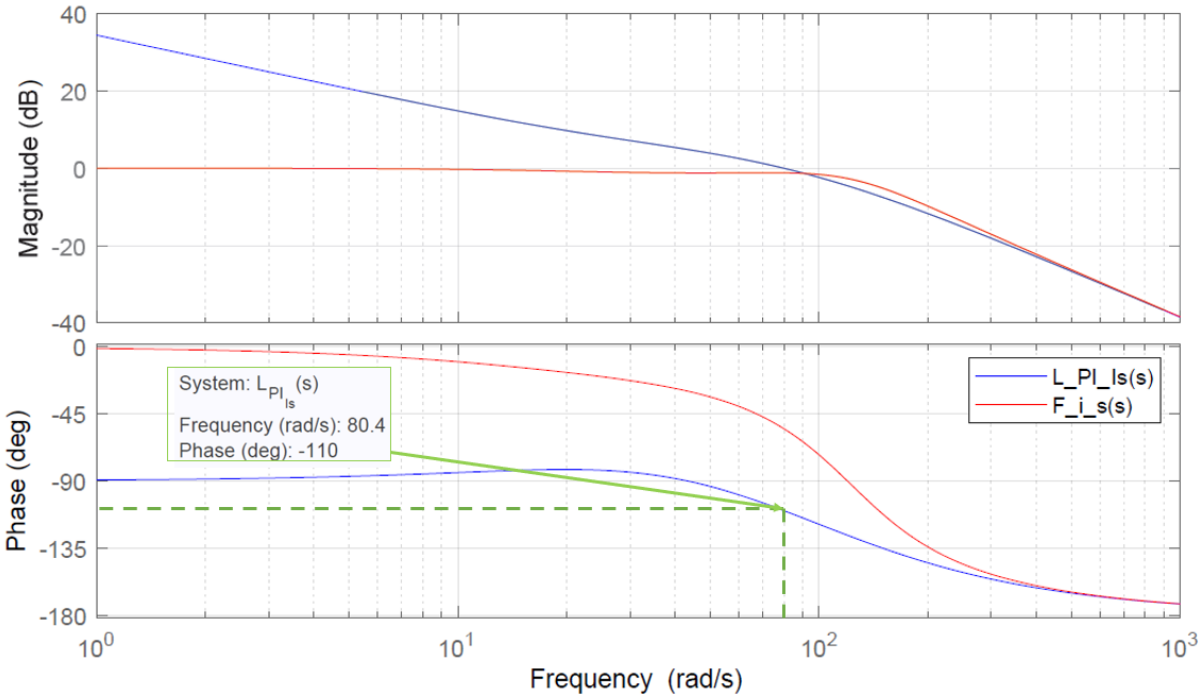

Figure 5-4 Bode plot of the open-loop and closed-loop of the current regulator

5.1.2 Speed controllers

5.1.2.1 One-mass system

Secondly, the speed controller is designed considering the mechanical model as a simple first order system. It means assuming that the motor speed is equal to the load speed and the shaft stiffness is infinite as described earlier in the first chapter. The simple model is represented by:

$$T_m - T_L = J_{tot}\frac{d\omega}{dt} + B\omega \tag{5-10}$$

where $J_{tot}[kg.m^2]$ is the total moment inertia of the machines, and $B[N.m.s/rad]$ is the motor viscous friction constant. Transferring equation (5-10) into Laplace domain, and setting the load torque to 0 ($T_L = 0$) results:

$$T_m(s) = J_{tot}s\omega + B\omega$$

Solving for the speed ω:

$$\omega(s) = T_m(s).\frac{1}{Js + B}$$

Hence the transfer function is:

$$G_\omega(s) = \frac{\omega(s)}{T_m(s)} = \frac{1}{J_{tot}s + B} \tag{5-11}$$

Multiplying the previous equation by the closed-loop transfer function of the current from equation (5-6) results:

$$L_\omega(s) = G_\omega(s)F_{i_{sq}}(s) \tag{5-12}$$

And including the speed regulator:

$$L_{PI_\omega}(s) = (K_{p\omega} + \frac{K_{i\omega}}{s})L_\omega(s) \tag{5-13}$$

The closed-loop transfer function becomes:

$$F_\omega(s) = \frac{L_{PI\omega}(s)}{1 + L_{PI\omega}(s)} \tag{5-14}$$

The overall control scheme for the speed regulator is shown in Figure 5-5.

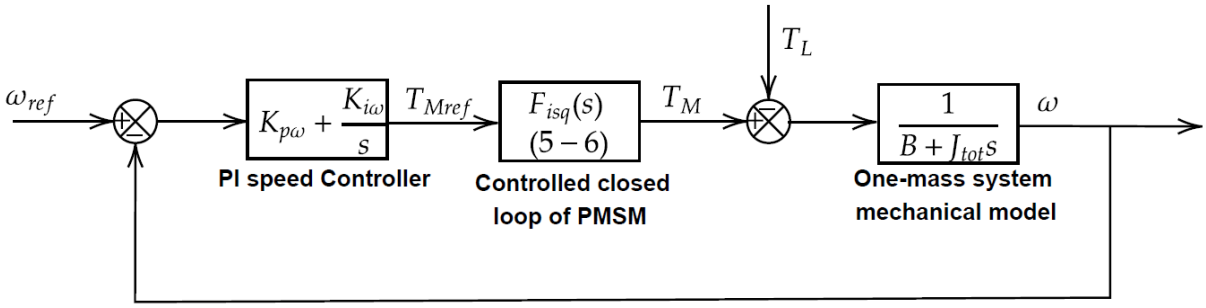

Figure 5-5 Control scheme for of the PI speed regulator for one-mass mechanical system

Tuning the PI speed regulator follows the same procedure as the current regulators. Firstly, the cutoff frequency of the speed closed-loop is chosen to be at least one decade lower than the inner loop, in this case are the current controllers with the cutoff frequency $\omega_{cI} = 80 rad/s$. Therefore, and after some calibration the cutoff frequency of the speed closed loop is set at $\omega_{c\omega} = 3\, rad/s$ which provides an acceptable performance. The phase margin is chosen to be $\phi_\omega = 60^o$. Appendix A section: "Current and speed PI-regulators m-files" reports the details of the tuning, which results in the following PI constants:

$$\begin{aligned} K_{P\omega} &= 0.2975\ Nms/rad \\ K_{I\omega} &= 0.4503\ Nms/rad \end{aligned} \tag{5-15}$$

The phase margin design requirement is met by analyzing the bode plot of the open-loop transfer function in Figure 5-6

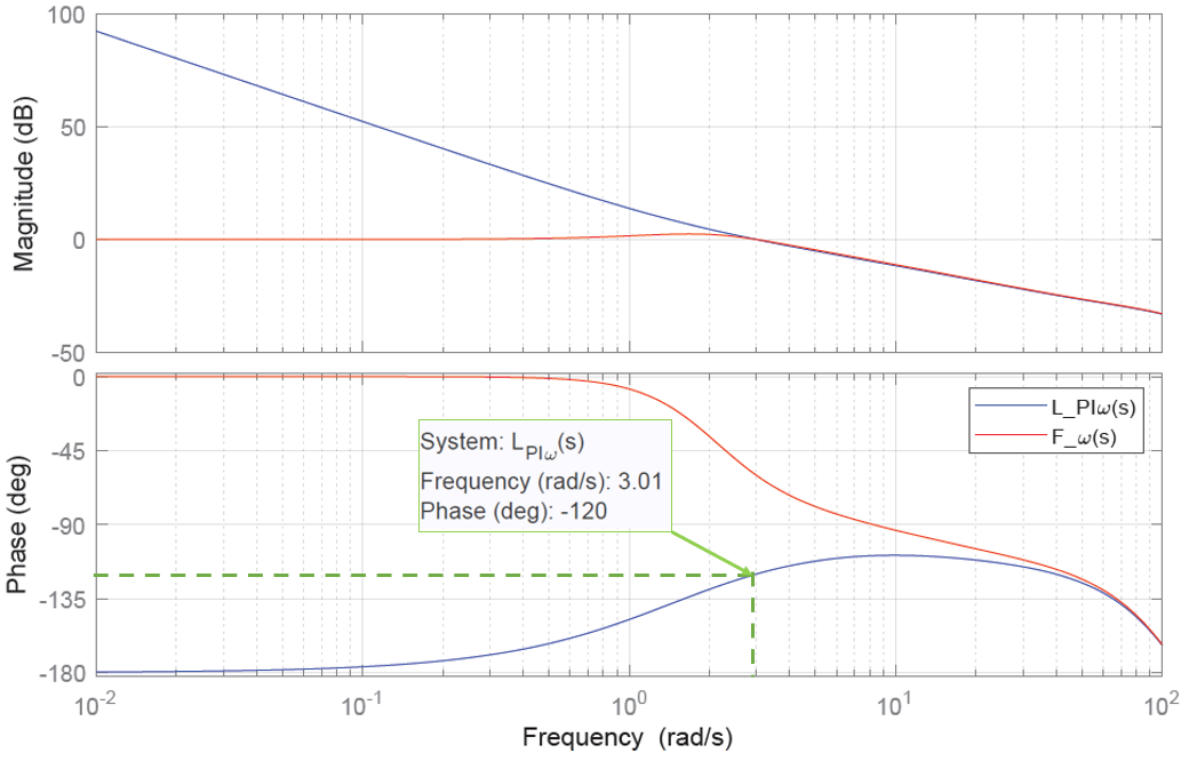

Figure 5-6 Frequency response bode plots of the open-loop and closed-loop speed regulator system of one-mass model

5.1.2.2 Two mass system

Since the problem under the study focuses on the two-mass mechanical system, the chosen control parameters in the previous section are also tested on a two-mass system by using the derived two-mass model from section 2.1. The transfer function which links the input electromagnetic input torque (T_M) and output load speed (ω_L) noted by $G_2(s)$ is recalled from equation (2-13):

$$\frac{\omega_L}{T_M} = G_2(s) = \frac{Bs + K_s}{J_L J_M s^3 + [B_L J_M + B_M J_L + B J_{tot}]s^2 + [K_s J_{tot} + B_M B_L + B B_{tot}]s + K_s B_{tot}} \tag{5-16}$$

Multiplying the previous equation by the closed-loop transfer function of the current from equation (4-6) results in:

$$L_{\omega 2}(s) = G_2(s) F_{i_{sd}}(s) \tag{5-17}$$

And including the speed regulator:

$$L_{PI_{\omega 2}}(s) = (K_{p\omega} + \frac{K_{i\omega}}{s}) L_{\omega}(s) \tag{5-18}$$

The closed-loop transfer function becomes:

$$F_{\omega 2}(s) = \frac{L_{PI\omega 2}(s)}{1 + L_{PI\omega 2}(s)} \tag{5-19}$$

From Figure 5-5 the one-mass mechanical model is replaced by the two-mass model represented in Figure 2-3, which results in the control scheme in Figure 5-7.

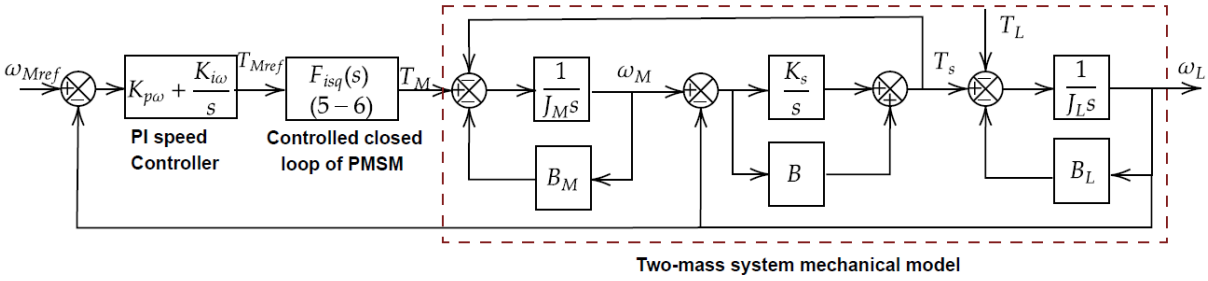

Figure 5-7 Control scheme of the PI speed regulator for two-mass mechanical system

With the replacement of the mechanical model, the same tuned regulators parameters are used ($K_{PI} = 0.7604\,\Omega\ \ K_{II} = 20.728\,\Omega/s\ K_{P\omega} = 0.2975\ Nms/rad\ \ K_{I\omega} = 0.4503\ Nm/rad$) obtained by the setup of the cutoff frequency and phase margin reported in the previous sections. The bode plots for the open and closed loop transfer functions are reported in Figure 5-8.

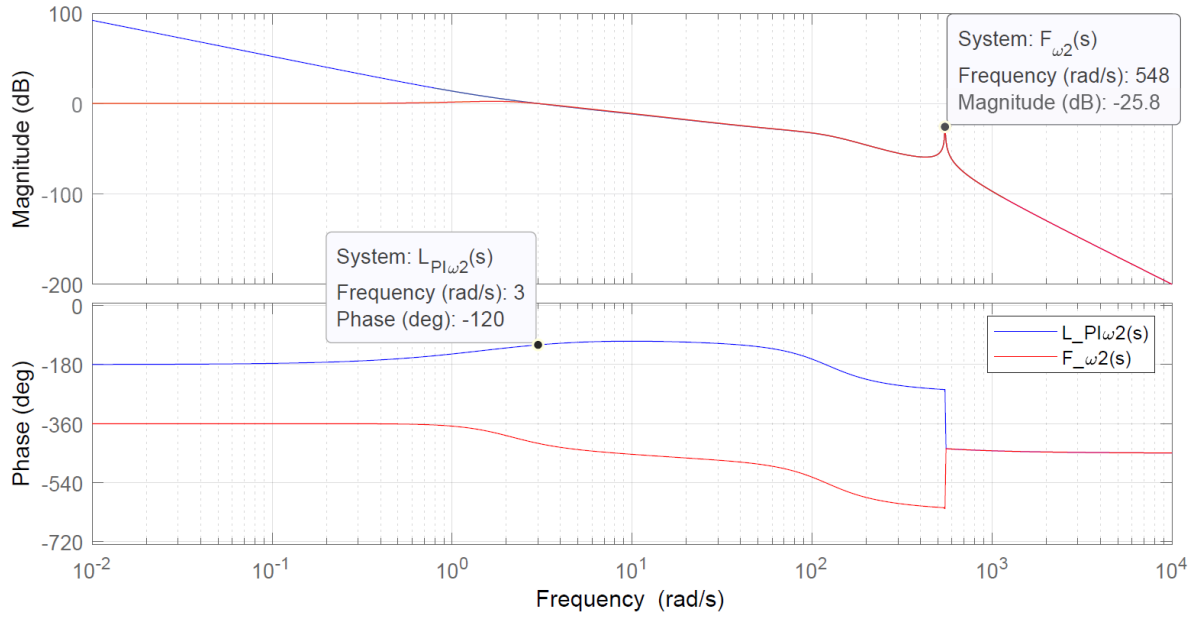

Figure 5-8 Frequency response bode plots of the open-loop and closed-loop speed regulator system of two-mass model

The key criterion for the two-mass system regulator design for PI controllers is to have the cutoff frequency of the speed regulator well below the resonance frequency of the mechanical system as it were found to be $\omega_{res} = 549 rad/s$ from (2 19) or as it can be obtained from the

bode plot in Figure 5-8. As well, the bode plot shows that the system is stable at the zero crossing with a phase margin of 60^o and there are no additional zero crossings around the resonance frequency. Hence, the designed control parameters of the cutoff frequency $\omega_{c\omega} = 3\ rad/s$ are suitable for one-mass and two-mass mechanical models.

However, as mentioned at the beginning of the section, the sole use of PI regulators is not effective against disturbances, since the basis of the PI control is minimizing the error between the set point and measured signals. The error tracking controllers are classified as feedback controllers which are characterised as relatively slow in case of strong or varying disturbance. As for this reason the PI regulators are placed under the category of passive anti-disturbance control (PADC).

5.2 Disturbance observer-based control system

The approach to overcome the disadvantages of the PADC is by using an active anti-disturbance control (AADC), which is a control method that consists of using the measurement of the disturbance or its estimation to counteract it. The approach is also referred to as feedforward compensation. Since most of the disturbances are difficult to be measured, observers are usually used to estimate them. In this study case, an observer is used to estimate the torsional torque of the shaft, due to the unavailability of this measurement for the reasons mentioned in the first chapter [16]. In the following section the basis of DOBC is explained. Suppose a system represented in state-space model:

$$\begin{aligned} \dot{\boldsymbol{x}} &= \boldsymbol{A}\boldsymbol{x} + \boldsymbol{B}_u u + \boldsymbol{B}_d d \\ \boldsymbol{y} &= \boldsymbol{C}\boldsymbol{x} \end{aligned} \tag{5-20}$$

where $\boldsymbol{x} \in R^n$, $u \in R^m$, $d \in R^m$, and $\boldsymbol{y} \in R^l$ represent state, control input, disturbance, and output vectors $\boldsymbol{A}$, $\boldsymbol{B}_u$, $\boldsymbol{B}_d$ and $\boldsymbol{C}$ represent system matrices with the following dimensions:

- $n \times n$ for the system matrix $\boldsymbol{A}$
- $n \times m$ for the control matrix $\boldsymbol{B}_{\mathrm{u}}$ and disturbance matrix $\boldsymbol{B}_d$
- $l \times n$ for the output matrix $\boldsymbol{C}$.

and the dot on the vector variable $\boldsymbol{x}$ represents the first time derivative. The system in (5-20) tries to follow the set point or the reference value which is noted by y_r via the control signal u. This signal depicted by:

$$u = k_1 e_y + k_0 \int_0^t e_y(\tau) d\tau - \hat{d} \tag{5-21}$$

Where the first two terms on the right-hand side of the equation represent the conventional PI controller while the last term represents the disturbances estimated by the observer. The task of the disturbance observer-based control is to estimate the disturbance d as accurately as possible in order to mitigate its influence on the system response. Although an integral part of the PI controller is responsible for mitigating any offset from the set points, it is not able to reduce variable disturbances. Hence, the additional term in the control signal can remove this kind of disturbances if estimated accurately. The implementation of DOBC does not require any excessive amount of control energy and can achieve a good disturbance-rejection

performance without sacrificing the performances at nominal conditions. The block diagram of the DOBC is shown in Figure 5-9.

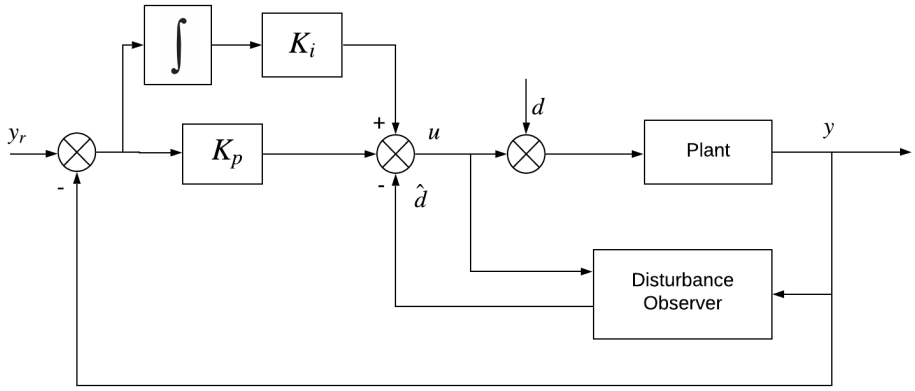

Figure 5-9 Basic structure of the disturbance observer-based control scheme

Two parts can be identified from Figure 5-9: the feedback control which is set by the PI regulators with their control variables and the feedforward control which consists of the feedforward compensation with the implementation of the observer. One of the advantages of using a control that is based on disturbance observers is that the system can benefit from the separation principle. This principle gives the control designer the possibility to design the feedback controllers independently from the feedforward. The common practice is to design the feedback regulators at first without considering the disturbances and uncertainties of the system, and the regulators will be responsible for the tracking and stabilization of the nominal dynamics of the plant. After the design of the feedback regulators is completed, the feedforward compensation part is designed to tackle the variable disturbances in the system. The implementation of the DOBC has the following advantages over the conventional PADC [16]:

- Faster response in handling the disturbances: the direct counteract of the feedforward compensation provides an estimation of the disturbances which cancels out the unwanted responses and therefore achieves faster dynamics than the passive feedback regulators.
- Patch features: the addition of the feedforward compensation does not affect the original loop of the control system. The design consists of the already tuned PI regulators with the considered models. No verification or certification process is needed to develop the DOBC.
- Less conservativeness: DOBC is not a worst-case-based design that can estimate and compensate disturbances online, thus has prominent adaptiveness and low conservativeness. Most of the existing robust control methods are worst-case-based design, where promising robustness is achieved with the price of degraded nominal performance, and thus have been criticized as being overconservative. In DOBC approach, the nominal performance of the baseline controller is recovered in the absence of disturbances or uncertainties, thus a better nominal dynamic performance can be achieved.

The state space representation depicted by equation (5-20) is going to be used to construct the system matrices and vector for our two-mass system. Recalling the differential equations which describe the mechanical system behaviour according to Newton's law and neglecting the motor and load damping:

$$J_M(\dot{\omega_M}) + B(\dot{\theta_M} - \dot{\theta_L}) + K(\theta_M - \theta_L) = T_M$$
$$J_L(\dot{\omega_L}) + B(\dot{\theta_L} - \dot{\theta_M}) + K(\theta_L - \theta_M) = -T_L \quad (5\text{-}22)$$

Choosing the state variable $\boldsymbol{x}$ as:

$$\boldsymbol{x} = \begin{bmatrix} \omega_M \\ (\theta_M - \theta_L) \\ \omega_L \end{bmatrix} \quad (5\text{-}23)$$

Where the angular deflection $(\theta_M - \theta_L)$ is referred to as the internal disturbance of the system.

The input control signal of the system is:

$$u = T_{Mref}$$

the output is the measured motor speed ω_M. Hence the output y and its matrix $\boldsymbol{C}$ are:

$$y = \boldsymbol{C}\boldsymbol{x} = [1 \quad 0 \quad 0] \begin{bmatrix} \omega_M \\ (\theta_M - \theta_L) \\ \omega_L \end{bmatrix} = \omega_M$$

In order to build the system matrix $\boldsymbol{A}$ and the control matrix $\boldsymbol{B_u}$, the equation (5-22) is rearranged to follow the chosen state variable from (5-23) as:

$$J_M(\dot{\omega_M}) + B(\dot{\theta_M} - \dot{\theta_L}) + K_s(\theta_M - \theta_L) = T_M$$
$$\dot{\omega_M} = \frac{-B(\dot{\theta_M} - \dot{\theta_L}) - K_s(\theta_M - \theta_L) + T_M}{J_M}$$

The angular deflection derivative $\left(\widehat{\dot{\theta_M}} - \widehat{\dot{\theta_L}}\right)$ is simply the difference between the motor speed and load speed:

$$\widehat{(\dot{\theta_M} - \theta_L)} = \omega_M - \omega_L$$

Similarly to the motor speed, the load speed ω_L can be expressed as follows:

$$J_L(\dot{\omega_L}) + B(\dot{\theta_L} - \dot{\theta_M}) + K_s(\theta_L - \theta_M) = -T_L$$
$$\dot{\omega_L} = \frac{-B(\dot{\theta_L} - \dot{\theta_M}) - K_s(\theta_L - \theta_M) - T_L}{J_L}$$

Where the load torque T_L is considered as an external disturbance to the system. Therefore, the two-mass sytem in the state-space representation is:

$$\frac{d}{dt}\begin{bmatrix} \omega_M \\ (\theta_M - \theta_L) \\ \omega_L \end{bmatrix} = \begin{bmatrix} -\frac{B}{J_M} & -\frac{K_s}{J_M} & \frac{B}{J_M} \\ 1 & 0 & -1 \\ \frac{B}{J_L} & \frac{K_s}{J_L} & -\frac{B}{J_L} \end{bmatrix} \cdot \begin{bmatrix} \omega_M \\ (\theta_M - \theta_L) \\ \omega_L \end{bmatrix} + \begin{bmatrix} \frac{1}{J_M} \\ 0 \\ 0 \end{bmatrix} \cdot T_M + \begin{bmatrix} 0 \\ 0 \\ -\frac{1}{J_L} \end{bmatrix} \cdot T_L \quad (5\text{-}24)$$

$$y = [1 \quad 0 \quad 0] \begin{bmatrix} \omega_M \\ (\theta_M - \theta_L) \\ \omega_L \end{bmatrix}$$

Building a DOBC requires to construct the observer at first. The state observer is used to estimate the states of the system which are not available by measurements such as the torsional torque (T_s) and the load speed (ω_L). If the observer is used for estimating all the n state variables, it is called a full-order state observer. If it estimates less than n states, it is known as reduced-order observer [26]. An observer can be formed either in the frequency domain or time domain. In the following sections the two approaches are analysed, and key design parameters are identified.

5.2.1 Frequency domain formulation

Designing a frequency domain observer starts with transforming the system variables into the s Laplace domain. A typical s domain control system is shown in Figure 5-10 [16]. Analysing the block diagram, which represents a single-input single-output linear system, its output is given by:

$$Y(s) = G_p(s)[U(s) + D(s)] \tag{5-25}$$

where $U(s)$ is the control input signal, $Y(s)$ the controlled output, $D(s)$ the disturbance, and $G_p(s)$ is the actual system model. In contrast to $G_P(s)$, the nominal system model indicated with $G_n(s)$ in Figure 5-10 refers to the modelled system which contains the model uncertainties swaying from the actual model $G_p(s)$. The system controller depicted by $C(s)$ can be a PI regulator as it was explained in the previous section. The key parameter in designing the frequency domain disturbance observer lies in the filter $Q(s)$. The issue of tuning the filter will be explained later in this section.

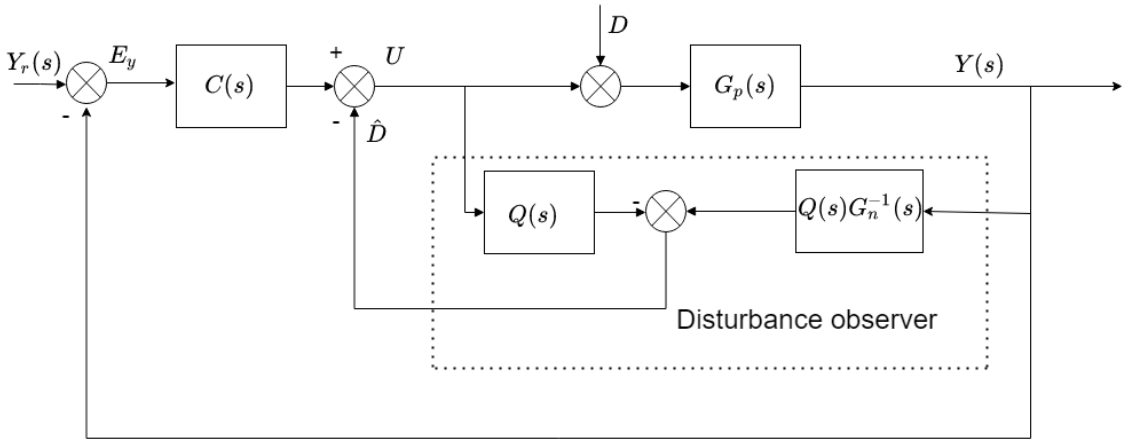

Figure 5-10 Block diagram of disturbance observer-based control in frequency domain

The output of the block diagram of the system in Figure 5-10 can be described by separating the output $Y(s)$ in two parts: the first part $Y_{yr}(s)$ which is due to the system reference input $Y_r(s)$, and the second part $Y_{yd}(s)$ which results from the system disturbance (D). This separation can be represented as:

$$Y(s) = Y_{yr}(s) + Y_{yd}(s) \tag{5-26}$$

Two transfer functions can be found with respect to the reference and disturbance as in:

$$Y(s) = T_{yr}(s)Y_r(s) + T_{yd}(s)D(s) \tag{5-27}$$

The first transfer function can be found by setting $\boldsymbol{D(s) = 0}$, and with simple substitution:

$$Y_{yr}(s) = G_P U \tag{5-28}$$

Where U:

$$U = CE_y - \widehat{D} \tag{5-29}$$

$\widehat{D}$ is:

$$\widehat{D} = QG_n^{-1}Y - UQ \tag{5-30}$$

and E_Y:

$$E_y = Y_r - Y \tag{5-31}$$

Substituting (5-31) and (5-30) into (5-29) results in:

$$U = C(Y_r - Y) + UQ - QG_n^{-1}Y$$

$$U(1 - Q) = C(Y_r - Y) - QG_n^{-1}Y$$

$$U = \frac{C(Y_r - Y) - QG_n^{-1}Y}{(1 - Q)} \tag{5-32}$$

With (5-32) ,(5-28), and neglecting the disturbance ($D(s) = 0$), then (5-26) is:

$$Y(s)|_{D(s)=0} = \frac{G_P C(Y_r - Y) - G_P Q G_n^{-1}Y}{(1 - Q)}$$

$$Y(s)(1 - Q + G_P Q G_n^{-1} + G_P C) = G_P C Y_r$$

Since $Y(s) = Y_{yr}(s)$ when $D(s) \neq 0$ then:

$$Y_{yr}(s) = \frac{G_n G_p C Y_r}{G_n[1 + CG_p] + Q[G_p - G_n]}$$

and the transfer function $T_{yr}(s) = Y_{yd}/Y_r$ is:

$$T_{yr}(s) = \frac{G_n G_p C}{G_n[1 + CG_p] + Q[G_p - G_n]} \tag{5-33}$$

Since the task of the observer is to estimate a disturbance in the medium or low frequency range and block the high frequency noise produced by the measurement units, the disturbance observer filter $Q(s)$ is designed with a low to medium cutoff frequency. The choice of the cutoff frequency in this range is reasoned by two points. Firstly, if the plant is indeed subjected to a high frequency disturbance, then the high frequency will not have an effect on the system since it is normally filtered by the inertia of the physical system ($G_P(s)$). Secondly, the compensating of such high frequency can be a challenge for the limited bandwidth of the actuators [27].

By analysing equation (5-33) and assuming the filter has a steady-state unity gain meaning that:

$$\lim_{\omega \to 0} Q(j\omega) = 1 \tag{5-34}$$

equation (5-33) results in:

$$\lim_{\omega \to 0} T_{ry}(j\omega) = \lim_{\omega \to 0} \frac{G_n(j\omega)C(j\omega)}{1 + G_n(j\omega)C(j\omega)} \tag{5-35}$$

which is the appropriate system response in the absence of the disturbance observer and compensation. Regarding the system transfer function in the presence of disturbance, it can be found in similar manner by setting $Y_r(s) = 0$ and finding the transfer function of the system block diagram as in:

$$Y_{yd}(s) = G_p(D + U) \tag{5-36}$$

Where U:

$$U = -\widehat{D} - CY_{yd} \tag{5-37}$$

and $\widehat{D}$:

$$\widehat{D} = QG_n^{-1}Y_{yd} - QU \tag{5-38}$$

Substituting (5-38) into (5-37) we have:

$$U = -QG_n^{-1}Y_{yd} + QU - CY_{yd}$$

$$U(1 - Q) = -QG_n^{-1}Y_{yd} - CY_{yd}$$

$$U = \frac{-QG_n^{-1}Y_{yd} - CY_{yd}}{(1 - Q)} \tag{5-39}$$

Replacing U with (5-39) in (5-36):

$$Y_{yd}(s) = G_p\left(D + \frac{-QG_n^{-1}Y_{yd} - CY_{yd}}{(1 - Q)}\right)$$

$$Y_{yd}(s) = \frac{G_nG_p[1 - Q]D}{G_n[1 + CG_p] + Q[G_p - G_n]}$$

and the transfer function $T_{yd}(s) = Y_{yd}/D$ is:

$$T_{yd}(s) = \frac{G_nG_p[1 - Q]}{G_n[1 + CG_p] + Q[G_p - G_n]} \tag{5-40}$$

In the ideal case the transfer function (5-40) equals:

$$\lim_{\omega \to 0} T_{yd}(j\omega) = 0 \text{ because } \lim_{\omega \to 0} Q(j\omega) = 1 \tag{5-41}$$

Hence, the effect of disturbance is completely neutralized and the system behaves as the baseline regulator design, without any external disturbance affecting it. An additional criterion to the filter $Q(s)$ is that it shall be designed with a relative degree (i.e, the order difference

between the denominator and the numerator of its transfer function) higher than that of the nominal plant $G_n(s)$ in order to ensure the transfer function $Q(s)G_n^{-1}(s)$ in the block diagram in Figure 5-10 is implementable.

5.2.2 Time domain formulation

The design of the observer in time domain can be straightforward by proceeding with the state-space representation of the system given in (5-20). However, the system must be observable in order to reconstruct the unmeasurable states from the system outputs. A system is said to be completely observable if and only if there exists a finite time T such that the initial state $\boldsymbol{x}(t_0)$ can be determined from the observation history $\boldsymbol{y}(t)$ given the control $\boldsymbol{u}(t)$, $t_0 \leq t \leq T$ [26]. The observability of a system can be tested by finding the rank of the observability matrix given by:

$$\boldsymbol{P_O} = \begin{bmatrix} \boldsymbol{C} \\ \boldsymbol{CA} \\ \vdots \\ \boldsymbol{CA}^{n-1} \end{bmatrix} \tag{5-42}$$

Where $\boldsymbol{A}$ and $\boldsymbol{C}$ are the system matrix and the output matrix, respectively, defined in system equation (5-20). The observability matrix $\boldsymbol{P_o}$ is an $n \times n$ matrix. If the rank of $\boldsymbol{P_o}$ is equal to n, then the system is observable. The system passes the observability check as well if the determinant of $\boldsymbol{P_o}$ is not zero. The observer task is to construct all the state variables from the available inputs. The mathematical model of the observer is the same as that of the plant as were given in system equation (5-20), except for an additional term that includes the error between the exact measured output and the estimated one as in:

$$\begin{aligned} \hat{\boldsymbol{x}} &= \boldsymbol{A}\hat{\boldsymbol{x}} + \boldsymbol{B}_u u + \boldsymbol{K}_e(y - \boldsymbol{C}\hat{\boldsymbol{x}}) \\ &= (\boldsymbol{A} - \boldsymbol{K}_e\boldsymbol{C})\hat{\boldsymbol{x}} + \boldsymbol{B}_u u + \boldsymbol{K}_e y \end{aligned} \tag{5-43}$$

$\hat{\boldsymbol{x}}$ are the estimated states derivatives, $\boldsymbol{C}\hat{\boldsymbol{x}}$ are the estimated outputs, and $\boldsymbol{B}_u$ is the control matrix as defined in (5-20). The matrix $\boldsymbol{K}_e$ is the observer gain which is a weighing matrix for the correction term involving the difference between the measured output (y) and the estimated output $\boldsymbol{C}\hat{\boldsymbol{x}}$. The whole term $\boldsymbol{K}_e(y - \boldsymbol{C}\hat{\boldsymbol{x}})$ in the previous equation indicates the observation error, which is responsible for correcting the model output and improving the system performance. However, the observer given in (5-43) is ideal when the actual matrices of the system are equal to the nominal, i.e., $\boldsymbol{A} = \boldsymbol{A_n}, \boldsymbol{B_u} = \boldsymbol{B_{un}}$, and $\boldsymbol{C} = \boldsymbol{C_n}$. Where the subscripts in the previous matrices indicate the nominal values. It is worth mentioing that the observer form in (5-43) does not include the external disturbance as it can bee seen in system given in (5-20). Hence if the external disturbances exist, the preformance of the estimation accuarcy will be affected. Finding the estimation error of the observer by subtracting the estimated state variables from the actual ones leads to:

$$\begin{aligned} \dot{\boldsymbol{x}} - \dot{\hat{\boldsymbol{x}}} &= \boldsymbol{A}\boldsymbol{x} + \boldsymbol{B}_u u - ((\boldsymbol{A} - \boldsymbol{K}_e\boldsymbol{C})\hat{\boldsymbol{x}} + \boldsymbol{B}_u u + \boldsymbol{K}_e y) \\ &= \boldsymbol{A}\boldsymbol{x} - \boldsymbol{A}\hat{\boldsymbol{x}} - \boldsymbol{K}_e(\boldsymbol{C}\boldsymbol{x} - \boldsymbol{C}\hat{\boldsymbol{x}}) \\ &= (\boldsymbol{A} - \boldsymbol{K}_e\boldsymbol{C})(\boldsymbol{x} - \hat{\boldsymbol{x}}) \end{aligned} \tag{5-44}$$

Defing the estimation error as:

$$\boldsymbol{e} = \boldsymbol{x} - \widehat{\boldsymbol{x}}$$

Then equation (5-44) becomes:

$$\dot{\boldsymbol{e}} = (\boldsymbol{A} - \boldsymbol{K}_e\boldsymbol{C})\boldsymbol{e}$$

The dynamic behavior of the error vector from the previous equation is determined by the eigenvalues of the matrix $(\boldsymbol{A} - \boldsymbol{K}_e\boldsymbol{C})$**.** If the observer gain matrix $\boldsymbol{K}_e$ is chosen properly in such a way to ensure a fast dynamic behaviour and it is asymptotically stable, then the error vector will converge to zero for any initial values of $\boldsymbol{e}(0)$. It means that $\widehat{\boldsymbol{x}}(t)$ will converge to $\boldsymbol{x}(\boldsymbol{t})$ with any initial values of state estimation $\widehat{\boldsymbol{x}}(0)$ or of the states $\boldsymbol{x}(0)$. It is possible to place the desired eigenvalues of the term $(\boldsymbol{A} - \boldsymbol{K}_e\boldsymbol{C})$ if the plant has been verified as observable [28]. Obtaining the observer gain matrix can be done by several methods such as the Transformation approach, Ackermann's formula or with the direct approach. In this thesis the latter is used due to the fact that the order of the system is 3 which means the direct approach is sufficient. As for a third order system the observer gain matrix is represented as:

$$\boldsymbol{K}_e = \begin{bmatrix} k_{e1} \\ k_{e2} \\ k_{e3} \end{bmatrix} \tag{5-45}$$

The gain values of the matrix $\boldsymbol{K}_e$ are obtained by equating the characteristic polynomial with the determinant of the characteristic equation:

$$|s\mathbf{I} - (\mathbf{A} - \mathbf{K}_e\mathbf{C})| = (s - \mu_1)(s - \mu_2)(s - \mu_3) \tag{5-46}$$

Where μ_i are the desired observer poles. The desired eigenvalues of the characteristic equation should be chosen at two to five times faster rate than those of the closed-loop system [27]. The design challenge of the time domain observer follows the same steps as in the frequency domain, where the observer gain matrix should not be chosen too large in case of having unreliable noisy measurements in the outputs y. A similar approach can be adopted by defining the damping coefficient ζ_o, the natural frequency ω_o, and α_o for the observer characteristic equation and then comparing the equation given in (5-46) as in:

$$B_{\mathrm{o}}(s) = (s + \alpha_{\mathrm{o}})(s^2 + 2\zeta_{\mathrm{o}}\omega_{\mathrm{o}}s + \omega_{\mathrm{o}}^2) \tag{5-47}$$

Which results in a combination of real and complex conjugate poles. In order for the observer to converge, the damping coefficient ζ_o is chosen high enough (≈ 1), and the natural frequencies are chosen to be higher than the cutoff frequency of the inner loop [29]. Once all the state variables have been estimated by the observer, the obtained variables can be used to compensate for the disturbances as can be seen in the block diagram in Figure 5-11.

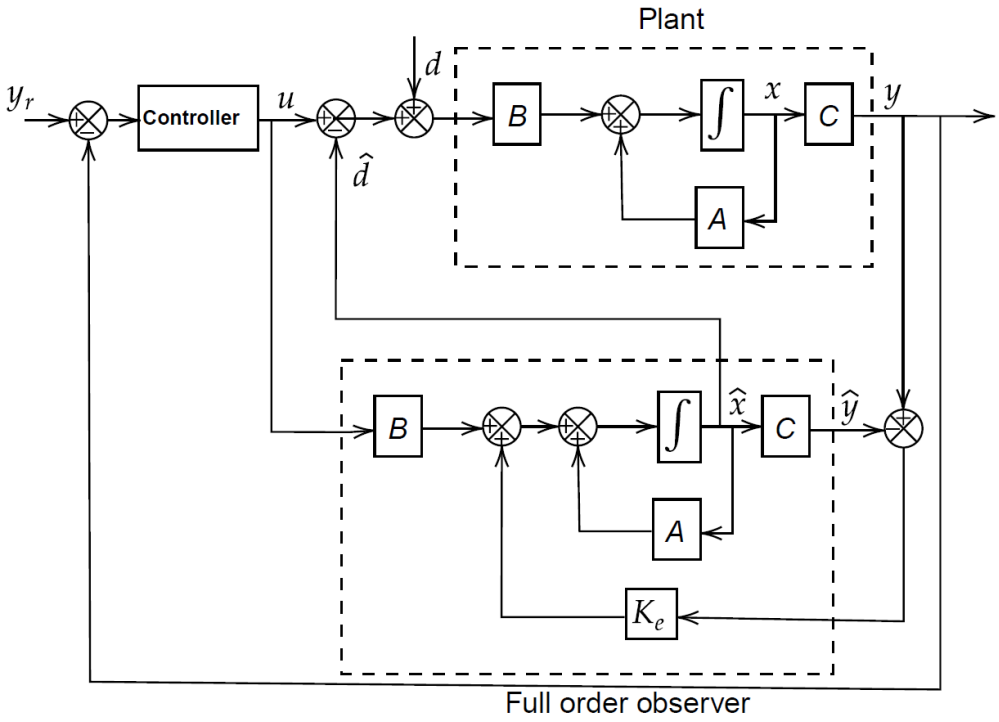

Figure 5-11 Block diagram of disturbance observer-based control in time domain

The aforementioned time domain disturbance observer is known as the linear Luenberger observer which can be used to estimate the internal system disturbances such as the torsional torque (T_s) in our system without taking into consideration the influence of external disturbances. Another type of observer called extended state observer, which can perform better under the existence of external disturbances, and it can be also used to estimate them external disturbances acting on the system such as the load torque (T_L). The extended state observer will be introduced in this work after the testing of the linear observer. However, in the case of Luenberger observer the system will be left without estimating and compensation for the load torque. The load torque will be considered as a disturbance to the estimation.

5.2.3 Observer design

In this subsection the time domain observer is constructed for our system starting with the observability check. Recalling the system matrices $\boldsymbol{A}$ and $\boldsymbol{C}$ from (5-24) to evaluate the observability matrix $\boldsymbol{P_o}$ (5-42):

$$\boldsymbol{A} = \begin{bmatrix} -\frac{B}{J_M} & -\frac{K_s}{J_M} & \frac{B}{J_M} \\ 1 & 0 & -1 \\ \frac{B}{J_L} & \frac{K_s}{J_L} & -\frac{B}{J_L} \end{bmatrix}$$

$$\boldsymbol{C} = [1 \quad 0 \quad 0]$$

$$\boldsymbol{C}.\boldsymbol{A} = [-B/J_M \quad -K_s/J_M \quad B/J_M] \text{ and}$$

$$\boldsymbol{C}.\boldsymbol{A^2} = \left[\left(\frac{B}{J_M}\right)^2 - \frac{K_s}{J_M} + \frac{B^2}{J_L J_M} \quad \frac{BK_s}{J_M^2} + \frac{BK_s}{J_M J_L} \quad -\frac{B^2}{J_M^2} + \frac{K_s}{J_M} - \frac{B^2}{J_L J_M}\right]$$

Then:

$$\boldsymbol{P_o} = \begin{bmatrix} [1] & [0] & [0] \\ [-\frac{B}{J_M}] & [\frac{1}{J_M}] & [\frac{B}{J_M}] \\ [\left(\frac{B}{J_M}\right)^2 - \frac{K_s}{J_M} + \frac{B^2}{J_L J_M}] & [\frac{BK_s}{J_M^2} + \frac{BK_s}{J_M J_L}] & [-\frac{B^2}{J_M^2} + \frac{K_s}{J_M} - \frac{B^2}{J_L J_M}] \end{bmatrix}$$

Substituting the values from Table II, we have:

$$\boldsymbol{P_o} = \begin{bmatrix} 1 & 0 & 0 \\ 0 & 370 & 0 \\ 2.9 * 10^5 & 0 & -2.9 * 10^5 \end{bmatrix}$$

And the determinant of $\boldsymbol{P_o}$ is:

$$|\boldsymbol{P_o}| = \boldsymbol{-2.18 * 10^8 \neq 0}$$

Hence, the system is observable, and the observer design can be conducted. The observer gain matrix $\boldsymbol{K_e}$ will be chosen according to the natural frequency ω_o, α_o and the damping factor ζ_o. However, the cutoff frequency of the system control must be known. The observer will be constructed to be implemented with the already designed control system from section 5.1, where the inner loop of the current regulators was selected to have a cutoff frequency of $\omega_{cI} = 80\ rad/sec$. Therefore, the observer cutoff frequency is selected to be higher than ω_{cI} in order for the observer to follow the current regulators and compensate for the disturbance. The observer poles are found by equating the equations (5-46) and (5-47):

$$|s\mathbf{I} - (\mathbf{A} - \mathbf{K}_e\mathbf{C})| = (s - \mu_1)(s - \mu_2)(s - \mu_3)$$

$$B_{\mathrm{o}}(s) = (s + \alpha_{\mathrm{obs}})\left(s^2 + 2\zeta\omega_{\mathrm{obs}}s + \omega_{\mathrm{obs}}^2\right)$$

$$\left|\begin{bmatrix} s & 0 & 0 \\ 0 & s & 0 \\ 0 & 0 & s \end{bmatrix} - \left(\begin{bmatrix} -\frac{B}{J_M} & -\frac{K_s}{\mathrm{J_M}} & \frac{B}{J_M} \\ 1 & 0 & -1 \\ \frac{B}{J_L} & \frac{K_s}{J_L} & -\frac{B}{J_L} \end{bmatrix} - \begin{bmatrix} k_{e1} \\ k_{e2} \\ k_{e3} \end{bmatrix} [1 \quad 0 \quad 0]\right)\right|$$
$$= (s + \alpha_{\mathrm{obs}})\left(s^2 + 2\zeta\omega_{\mathrm{obs}}s + \omega_{\mathrm{fo}}^2\right)$$

$$\left|\begin{bmatrix} s & 0 & 0 \\ 0 & s & 0 \\ 0 & 0 & s \end{bmatrix} - \left(\begin{bmatrix} -\frac{B}{J_M} & -\frac{K_s}{\mathrm{J_M}} & \frac{B}{J_M} \\ 1 & 0 & -1 \\ \frac{B}{J_L} & \frac{K_s}{J_L} & -\frac{B}{J_L} \end{bmatrix} - \begin{bmatrix} k_{e1} & 0 & 0 \\ k_{e2} & 0 & 0 \\ k_{e3} & 0 & 0 \end{bmatrix}\right)\right|$$
$$= (s + \alpha_{\mathrm{obs}})\left(s^2 + 2\zeta\omega_{\mathrm{obs}}s + \omega_{\mathrm{obs}}^2\right)$$

$$\begin{vmatrix} s + \frac{B}{J_M} + k_{e1} & \frac{K_s}{\mathrm{J_M}} & -\frac{B}{J_M} \\ -1 + k_{e2} & s & 1 \\ -\frac{B}{J_L} + k_{e3} & -\frac{\mathrm{K_s}}{J_L} & s + \frac{B}{J_L} \end{vmatrix} = (s + \alpha_{\mathrm{obs}})\left(s^2 + 2\zeta\omega_{\mathrm{obs}}s + \omega_{\mathrm{obs}}^2\right)$$

$$s^3 + \left(k_{e1} + \frac{B}{J_L} + \frac{B}{J_M}\right)s^2 + \left(\frac{Bk_{e3}}{J_M} + \frac{Bk_{e1}}{J_L} - \frac{K_s k_{e2}}{J_M} + \frac{K_s}{J_M} + \frac{K_s}{J_L}\right)s + \frac{K_s k_{e3}}{J_M} + \frac{K_s k_{e1}}{J_L} = s^3 + (2\zeta_{obs}\omega_{obs} + \alpha_{obs})s^2 + (2\zeta\omega_{obs}\alpha_{obs} + \omega_{obs}^2)s + \omega_{obs}^2\alpha_{obs} \quad (5\text{-}48)$$

The three parameters can be found by comparing the coefficients on both sides of the equality, starting from the first gain parameter k_{e1}:

$$s^3 + \left(k_{e1} + \frac{B}{J_L} + \frac{B}{J_M}\right)s^2 + \left(\frac{Bk_{e3}}{J_M} + \frac{Bk_{e1}}{J_L} - \frac{K_s k_{e2}}{J_M} + \frac{K_s}{J_M} + \frac{K_s}{J_L}\right)s + \frac{K_s k_{e3}}{J_M} + \frac{K_s k_{e1}}{J_L} = s^3 + (2\zeta_{obs}\omega_{obs} + \alpha_{obs})s^2 + (2\zeta_{obs}\omega_{obs}\alpha_{obs} + \omega_{obs}^2)s + \omega_{obs}^2\alpha_{obs}$$

$$\left(k_{e1} + \frac{B}{J_L} + \frac{B}{J_M}\right) = (2\zeta_{obs}\omega_{obs} + \alpha_{obs})$$

Which gives:

$$k_{e1} = 2\zeta_{obs}\omega_{obs} + \alpha_{obs} - \frac{B}{J_L} - \frac{B}{J_M} \quad (5\text{-}49)$$

k_{e2} can be found in a similar manner:

$$\frac{Bk_{e3}}{J_M} + \frac{Bk_{e1}}{J_L} - \frac{K_s k_{e2}}{J_M} + \frac{K_s}{J_M} + \frac{K_s}{J_L} = 2\zeta\omega_{obs}\alpha_{obs} + \omega_{obs}^2$$

Hence, the second gain parameter k_{e2} is:

$$k_{e2} = -\frac{J_M}{K_s}(2\zeta\omega_{obs}\alpha_{obs} + \omega_{obs}^2) + \frac{Bk_{e3}}{K_s} + \frac{BJ_M k_{e1}}{K_s J_L} + 1 + \frac{J_M}{J_L}$$

$$k_{e2} = -\frac{J_M}{K_s}(2\zeta\omega_{obs}\alpha_{obs} + \omega_{obs}^2) + \frac{B}{K_s}(k_{e3} + \frac{J_M k_{e1}}{J_L}) + \frac{J_M}{J_L} + 1 \quad (5\text{-}50)$$

Finally, the 3rd observer gain constant is found by:

$$\frac{K_s k_{e3}}{J_M} + \frac{K_s k_{e1}}{J_L} = \omega_{obs}^2\alpha_{obs}$$

After some operations, k_{e3} is found with the following equation:

$$k_{e3} = \frac{J_M}{K_s}\alpha_{obs}\omega_{obs}^2 - \frac{J_M k_{e1}}{J_L} \quad (5\text{-}51)$$

The final step is to select appropriate values for the parameters ω_{obs} and α_{obs}, and the damping coefficient (ζ_{obs}) . In [29] it is suggested to placeα_{obs} at the resonance frequency of the mechanical system (ω_{res}) defined by equation (2-19), and the frequency ω_{obs} to be placed between the resonance frequency and the anti-resonance frequency (ω_{ares}). From (2-20) the following equation can be obtained:

$$\omega_{obs} = \frac{2\omega_{\text{ares}}}{3} + \frac{\omega_{\text{res}}}{3}$$

By using the suggested method, we evaluate the characteristic parameters:

$$\begin{gathered}\alpha_{obs1} = \omega_{res} = 549.0\ rad/s \\ \zeta_1 = 1 \\ \omega_{obs1} = \frac{2\omega_{\text{ares}}}{3} + \frac{\omega_{\text{res}}}{3} = \frac{2 * 85.74}{3} + \frac{549.0}{3} = 240.2\ rad/s\end{gathered} \tag{5-52}$$

The characteristic parameters result in the observer gain constants as follows, where the second subscript (1) indicates the first observer poles selection method to be compared with other methods:

$$\begin{gathered}k_{e11} = 2\zeta_{obs}\omega_{obs1} + \alpha_{obs1} - \frac{B}{J_L} + \frac{B}{J_M} = 2 * 1 * 240.2 + 549.0 = 1029\ rad/s \\ k_{e21} = -\frac{J_M}{K_s}\left(2\zeta\omega_{obs}\alpha_{obs} + \omega_{obs}^2\right) + \frac{Bk_{e3}}{K_s} + \frac{BJ_Mk_{e1}}{K_sJ_L} + 1 + \frac{J_M}{J_L} = -0.06791\ p.u \\ k_{e31} = \frac{J_M}{K_s}\alpha_{obs}\omega_{obs}^2 - \frac{J_Mk_{e1}}{J_L} = 81.95\ rad/s\end{gathered} \tag{5-53}$$

However, in [29] the effect of the non-ideal inverter of the electrical system is not considered. Hence in this thesis, the proposed selection of the poles is tested, although it is not considered as a benchmark. An alternative observer poles selection is also considered by placing the poles as twice to five times further than the current inner loop of our system on s-plane, i.e. the observer response time is set to be faster than any other inner loops [27]. If the previous criterion is fulfilled, the stability of the system is ensured. Hence, the observer cutoff frequencies are selected to be:

$$\alpha_{obs} = \omega_{obs} = 2 * \omega_{cI}$$

Hence the characteristic equation parameters for the observer are evaluated as:

$$\alpha_{obs2} = \omega_{obs2} = 2 * 80 = 160\ rad/s \tag{5-54}$$

And the damping coefficient is $\zeta_{obs2} = 1$. The calculation of the observer gains is done in the same manner as in (5-53):

$$\begin{gathered}k_{e12} = 480\ rad/s \\ k_{e22} = 0.7638\ p.u \\ k_{e32} = 1.928\ rad/s\end{gathered} \tag{5-55}$$

5.2.4 Compensation action

The idea behind the AADC is to directly counteract disturbances by feedforward compensation control design based on disturbance measurements or estimations. Once the observer design is completed, it is possible to add a compensating term to the control signal. In other words, the estimated torsional torque will be added to the reference motor torque as an input to the current controllers as explained in the motivation of the observers at the beginning of section 5.2. The action of adding the estimated torsional torque to the reference torque signal is justified by recalling the motor mechanical equation from (2-2):

$$J_M(\dot{\omega_M}) + B_M\omega_M = T_M - T_s \tag{5-56}$$

We add the estimated torsional torque ($\widehat{T_s}$) to include it as additional part of the reference torque in order to counteract the torsional vibration disturbance. As a result, the total reference torque will be:

$$T_{tot,ref} = T_{Mref} + \widehat{T_s} \tag{5-57}$$

Substituting T_{tot} into (5-56) as the new value of the motor torque, it results:

$$J_M(\dot{\omega_M}) + B_M\omega_M = T_{Mref} + \widehat{T_s} - T_s \tag{5-58}$$

Now instead of having only T_{Mref} as input to the current regulator, it will also include the feedforward compensation part of the torsional torque $\widehat{T_s}$. If the time delay of the observer is negligibly small and the observer is able to estimate the torsional torque correctly then $\widehat{T_s}(t) \approx T_s(t)$ and the system will be able to compensate for the disturbance. Since the cutoff frequency of the observer has been designed twice fast as than the inner loop of the current regulators, the previous condition is certainly met. The overview of the compensation operation is shown in Figure 5-12.

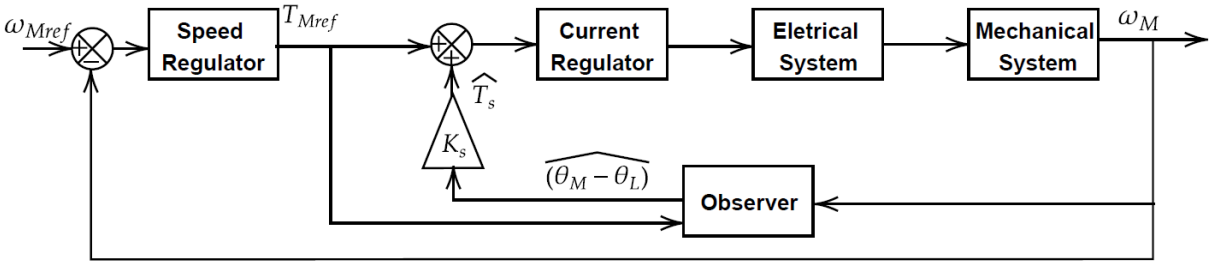

Figure 5-12 Compensation action block diagram

5.2.5 Observer simulation results

Implementing the time domain observer in Simulink is a straightforward procedure identical to the creation of the block diagram in Figure 5-11 with the usage of the observer definition from the equation (5-43). The details to implement the system in Simulink are reported in Appendix B, as well as the simulation configuration parameters reported in Appendix A. To evaluate the feasibility of the built system, four tests will be performed with two different settings. The tests differ in the applied speed reference values. The first one is shown in Figure 5-13.

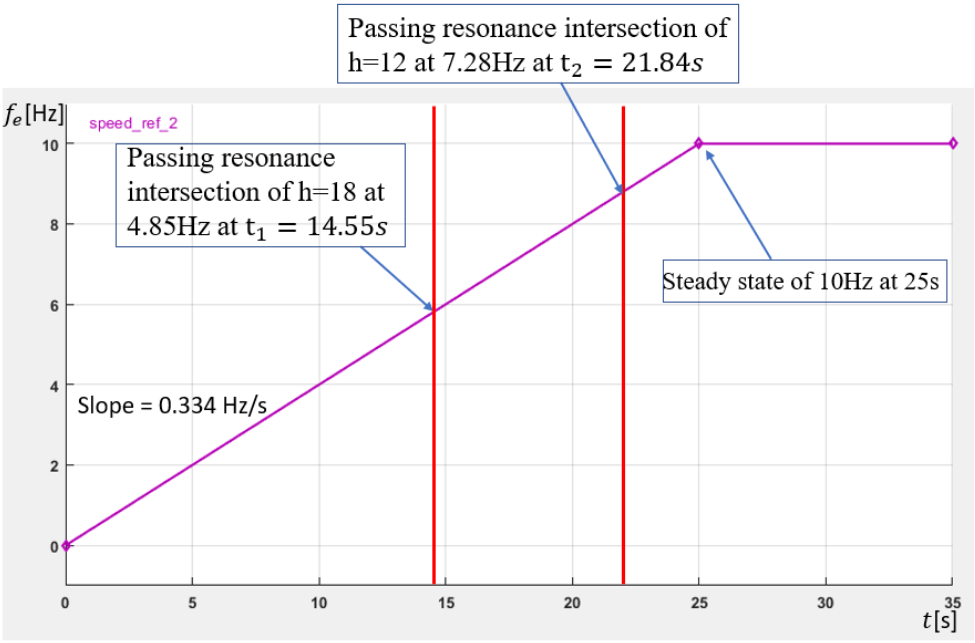

Figure 5-13 First reference speed test signal

The first test signal is designed to have the reference speed signal crossing the critical points which excite the system resonance at time $t_1 = 14.55s$ and $t_2 = 21.84s$ due to the harmonic contents of order h=18 and h=12, respectively.

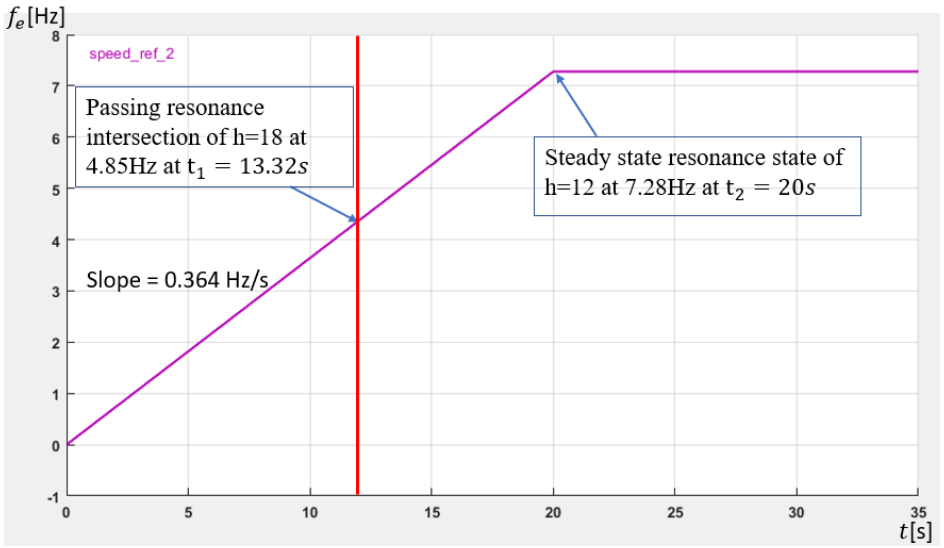

Figure 5-14 Second reference speed test signal

In contrast to the first signal, the second reference signal is designed in order to have the steady-state condition at the mechanical resonance frequency at $t_2 = 20s$ and pass by the first resonance intersection at $t_1 = 13.32s$. Both of the speed reference values shown in the previous figures were given as electrical frequency, and then, simply by multiplying the frequency by $4\pi/p$, were converted into mechanical speed in rad/s.

Each of the two signals will be simulated with two different observer parameters settings to test the effect of changing the observer poles. However, all the tests will be performed with an applied load torque that is 10% of the machine rated torque. The torque is implemented as ramp function that is initiated after $1.5s$ and with a slope of $0.5\ Nm/s$ represented in Figure 5-15.

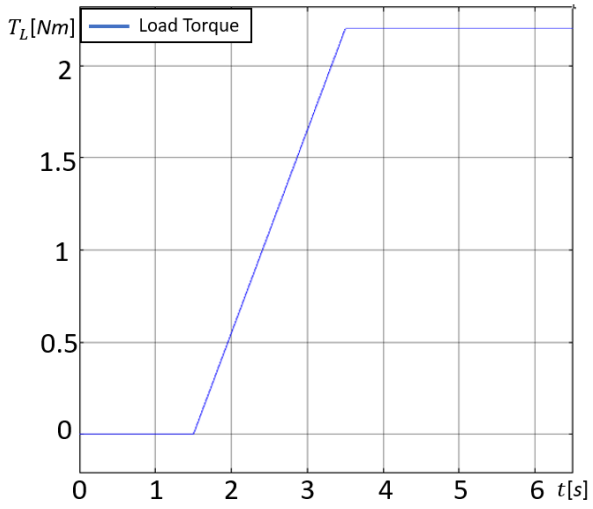

Figure 5-15 Simulation load torque

The simulations were done to test two types of mechanical models. Firstly, the behaviour of the system is observed while having two separated mechanical models (Figure 5-16), where a single degree-of-freedom mechanical model which accounts for a concatenated system inertia ($J_{tot} = J_M + J_L$) is used to obtain the system speed. A two-degree of freedom model instead, accounts for the coupling characteristics, i.e., stiffness and damping, and is used to obtain the angular deflection. The latter model takes the machines inertias separately.

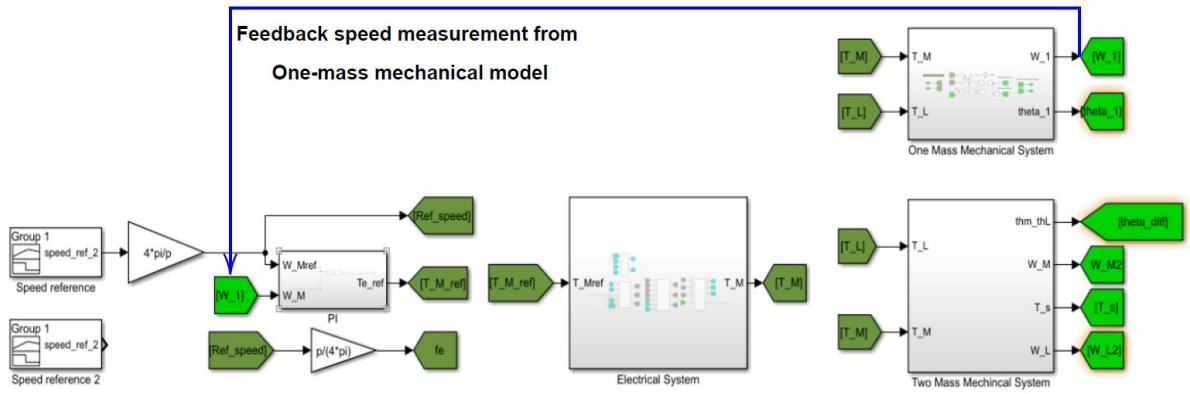

Figure 5-16 Separated mechanical models

For the second case, only the two-mass mechanical model is involved in the simulation with the motor speed ω_M as feedback to the speed regulator. Such a configuration is demonstrated in Figure 5-17.

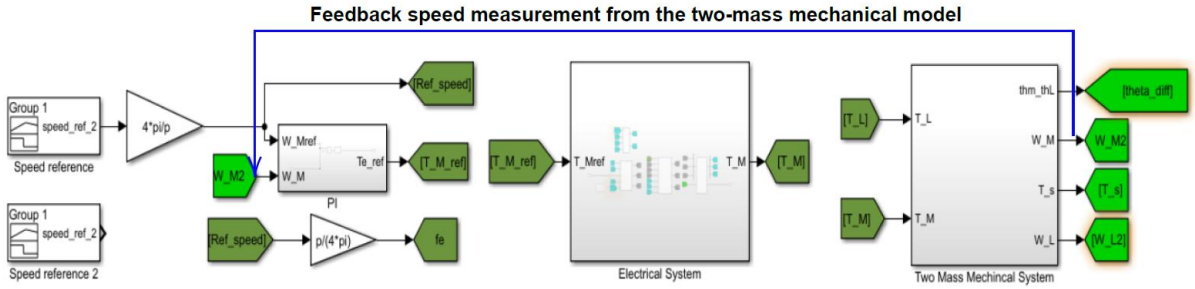

Figure 5-17 Single model mechanical system

The simulation tests will be as follows:

Firstly, the system will be tested without the insertion of the feedforward compensation from the observer estimation of the torsional torque (or shaft torque)($\widehat{T_s}$). After the baseline simulations have been done, the feedforward compensation is added to system as shown in Figure 5-12.

The previous steps are made twice for the two selected observer poles from (5-53) and (5-55). For each stage, the speed response of the one-mass and two-mass mechanical models are reported and compared. In addition, the actual angular deflection ($\theta_M - \theta_L$), the observer estimation ($\widehat{\theta_M - \theta_L}$), and estimation error ($(\theta_M - \theta_L) - (\widehat{\theta_M - \theta_L})$) are shown. A summary of simulations is reported in the chart in Table III.

Table III Simulation tests breakdown

Configuration	Test 1		Test 2		Test 3		Test 4	
Mechanical model	One and two-mass separated		Two mass		One and two-mass separated		Two mass	
Reference signal	First signal Figure (5-13)				Second signal Figure (5-14)			
Poles	a)	b)	a)	b)	a)	b)	a)	b)

Where the poles of a) and b) are recalled from equations (5-52) and (5-54), which are $\omega_{obs1} = 240rad/s$, $\alpha_{obs_1} = 549rad/s$ and $\omega_{obs2} = \alpha_{obs_2} = 160rad/s$) , respectively. For the sake of simplicity, the observer with poles a) is named as observer 1 while the observer with poles b) is named observer 2.

5.2.5.1 Test 1: Two separated mechanical models, first reference speed signal

In these results, the base model speed response of the one-mass mechanical model and load speed of the two-mass mechanical model are reported to be compared. The load speed was chosen in the comparison over the motor speed due to the fact that the load speed shares more characteristics with the one-mass speed while showing the resonance occurrences. In addition,

the angular deflection, the observer estimation, and the estimation error of the two-mass mechanical model are reported in the same graph.

5.2.5.1.1 Base model response

Figure 5-18 shows the output speed of the one-mass model (ω) following the reference speed as attended with a slight drop as the load torque is inserted at $t = 1.5s$. On the contrary, the load speed (ω_L) of the two-mass model is following the reference speed in identical manner to that of the one-mass speed until it approaches the first resonance intersection at $t_1 = 14.55s$ where it experiences a large oscillation increment. The same behaviour repeats for the second time as it approaches the second resonance intersection at $t_2 = 21.84s$. It can be noticed (Figure 5-18) that a beating phenomenon occurs once the speed is approaching the resonance condition. Since all dampings in the two-mass system have been neglected, it is evident from the load speed plot that the increased oscillation persists along the simulation time.

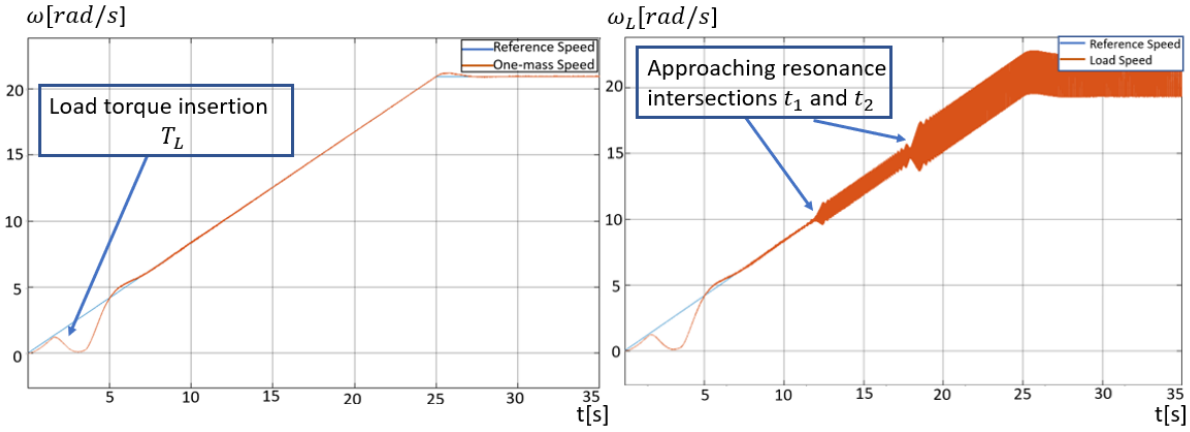

Figure 5-18 Reference speed, one-mass speed ω (left), and load speed ω_L of the two-mass system (right) of test 1

The actual, the estimated angular deflection, and the error for the first observer and the second observer poles are reported in Figure 5-19 and Figure 5-20 , respectively. Where the angular deflection ($\theta_M - \theta_L$) show a similar behaviour of the load speed. The first resonance point increases the angular deflection to a peak value of around $0.06\ rad$ and up to approximately $0.15\ rad$ at the second resonance intersection. The large value of the angular deflection can be a critical condition for the shaft material and can cause damage to the machine as it has been reviewed in the second chapter. Regarding the estimation accuracy, both the observer poles choices seem to follow the actual values. However, it is possible to calculate the estimation error for the two observers when the system reaches the steady-state condition (around $t \approx 26s$). For the first observer the estimation error at the steady-state is highlighted from Figure 5-19, and the actual value of the angular deflection at that point is $1.21 * 10^{-1}\ rad$. Hence the estimation error can be evaluated as:

$$e_{obs} = \frac{(\theta_M - \theta_L)}{(\theta_M - \theta_L) - (\widehat{\theta_M - \theta_L})}$$

$$e_{obs1} = \frac{1.27 * 10^{-3} rad}{1.21 * 10^{-1} rad} = 1.05 * 10^{-2} \quad (5\text{-}59)$$

Observer 1 estimation error in the bottom part of Figure 5-19 shows a constant error of $0.6 * 10^{-3} rad$ appears at $t = 1.5s$, which is due to the unmodeled load torque (T_L) in the linear Leuenberger observer design. It can be verified that this error follows the shape of T_L (Figure 5-15). On the other hand, the estimation performance of observer 2 in Figure 5-20 gives a steady-state error of:

$$e_{obs2} = \frac{2.60 * 10^{-3} rad}{1.21 * 10^{-2} rad} = 2.15 * 10^{-2} \quad (5\text{-}60)$$

and a constant error appearing from $t = 1.5s$ reaching the maximum at $t = 3.5s$ with $2.14 * 10^{-3}\ rad$, as being highlighted in Figure 5-20. The second choice of poles shows a high error at steady state and it is largely affected by the unmodeled load torque. However, it as it can be noticed by comparing Figure 5-19 and Figure 5-20, the latter choice of observer poles holds an advantage over the former resulting in lower oscillations. It can be approximated that the peak-to-peak error value at steady-state from Figure 5-19 is around $1.5 * 10^{-3} rad$ compared to $0.5 * 10^{-3} rad$ from Figure 5-20. Hence, the latter choice of observer poles has less oscillation.

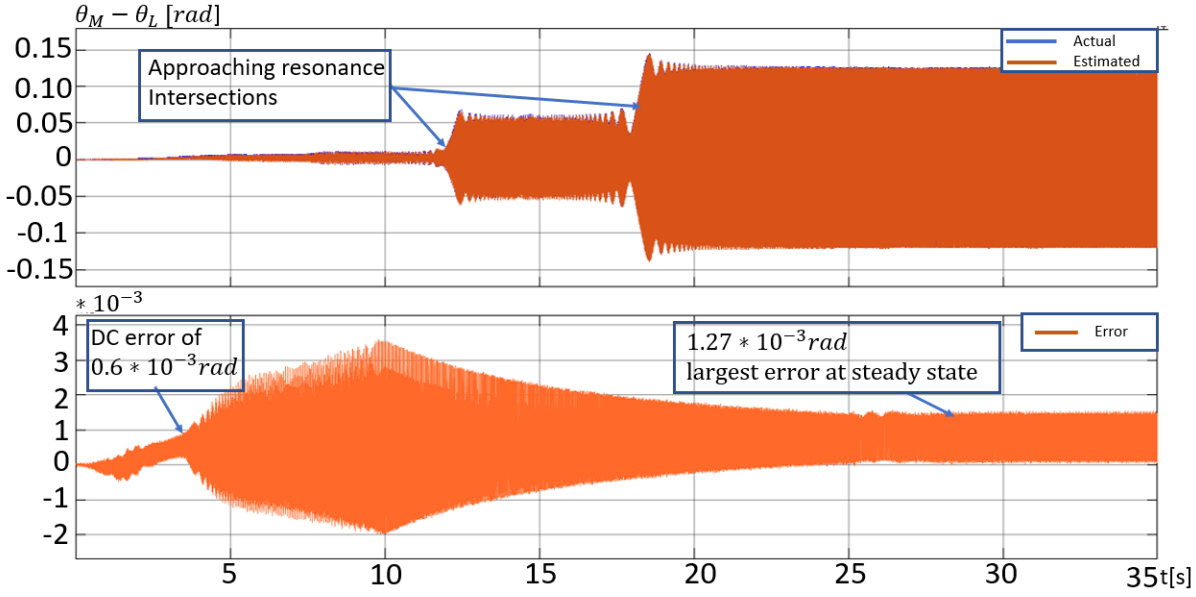

Figure 5-19 Actual and estimated angular deflection (top) and the estimation error (bottom) of test 1 of first observer poles

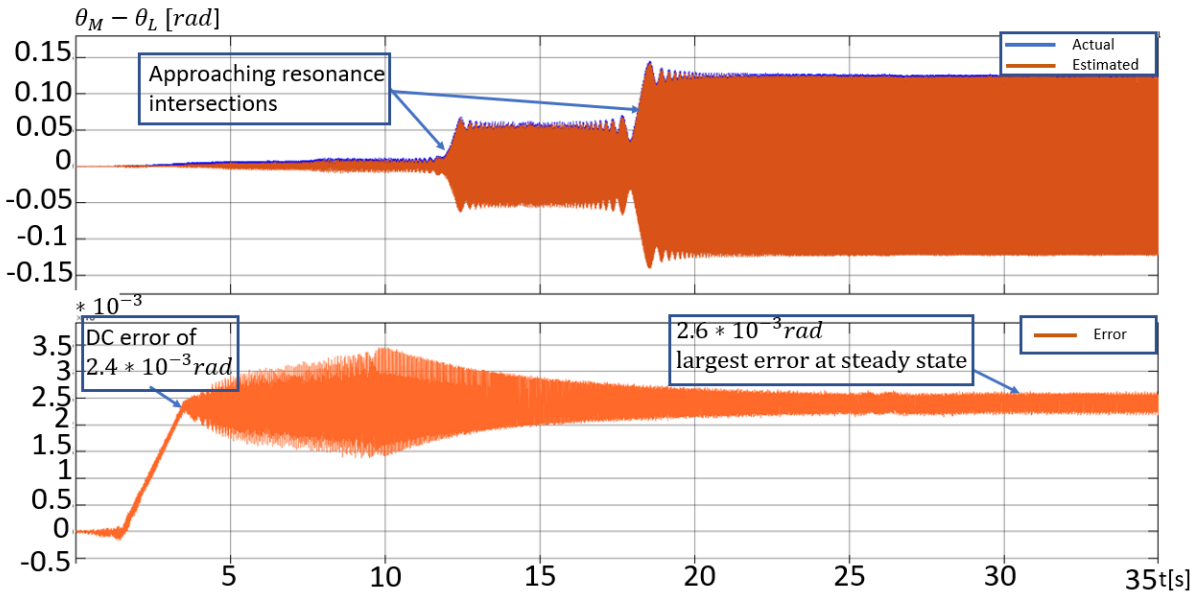

Figure 5-20 Actual and estimated angular deflection (top) and the estimation error (bottom) of test 1 of second observer poles

5.2.5.1.2 Compensated response

In the previous section the observed design was validated for both the pole choices. Now, the effectiveness of such an observer in damping the torsional vibrations can be tested. In another words, the observer is implemented in the control system, as explained in 5.2.4, and provides an estimate of the shaft torque which is added as a feedforward term. The speed output for the one-mass system (ω) and load speed (ω_L) for the two-mass system of observer 1 reported in Figure 5-21 and for the observer 2 is shown in Figure 5-22. It can immediately be recognized from the load speed plots that both the resonance intersections effects are suppressed by the usage of the feedforward compensation. In addition, the one-mass speed has not been affected by the action in any noticeable value if we compare the reported load speed in Figure 5-21 and Figure 5-22 with the baseline response in Figure 5-18. As it was stated in the introduction of the DOBC, the implementation of the feedforward compensation via observer does not affect the original system dynamics. Regarding the two choices of observer poles, it appears that the small error measurement differences between them do not affect the output speeds.

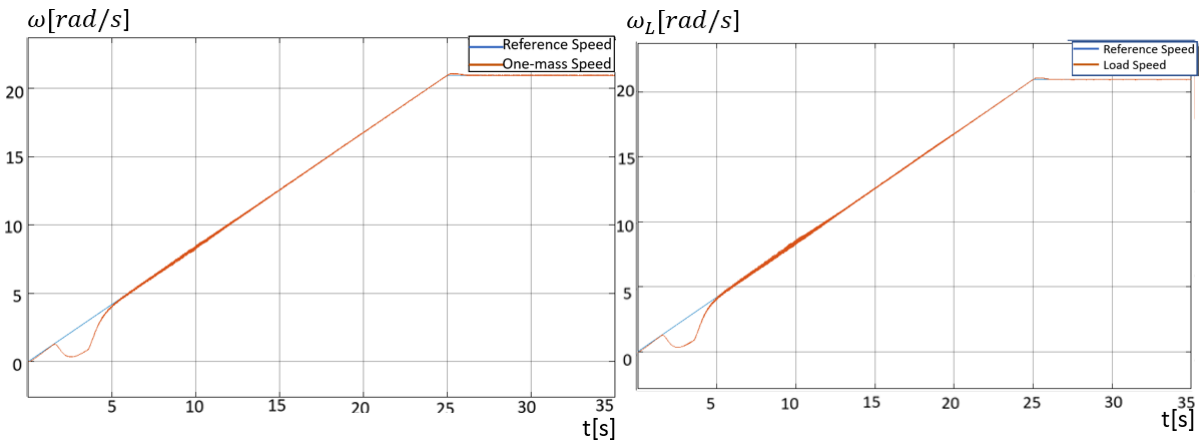

Figure 5-21 Reference speed, one-mass speed (left), and load speed of the two-mass system (right) of test 1 with observer 1

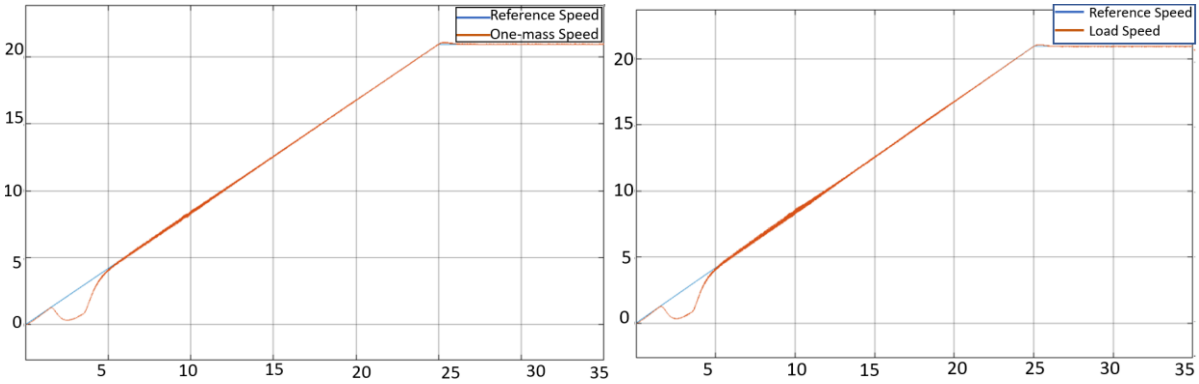

Figure 5-22 Reference speed, one-mass speed (left), and load speed of the two-mass system (right) of test 1 with observer 2

The angular deflection of the two poles settings can be seen in Figure 5-23 and Figure 5-24, The suppression of the resonance is noticeable, as the peaks the system experiences in Figure 5-19 are reduced from 0.06 rad and 0.15 rad to around 0.006 rad for both the intersections. However, a new deflection peak of 0.014 rad is now noticeable at $t = 10s$ which does not occur as a consequence of a mechanical resonance condition. In conclusion of the first test, the feedforward compensation effectively reduces the angular deflection caused by the TNF by at least a factor of ten.

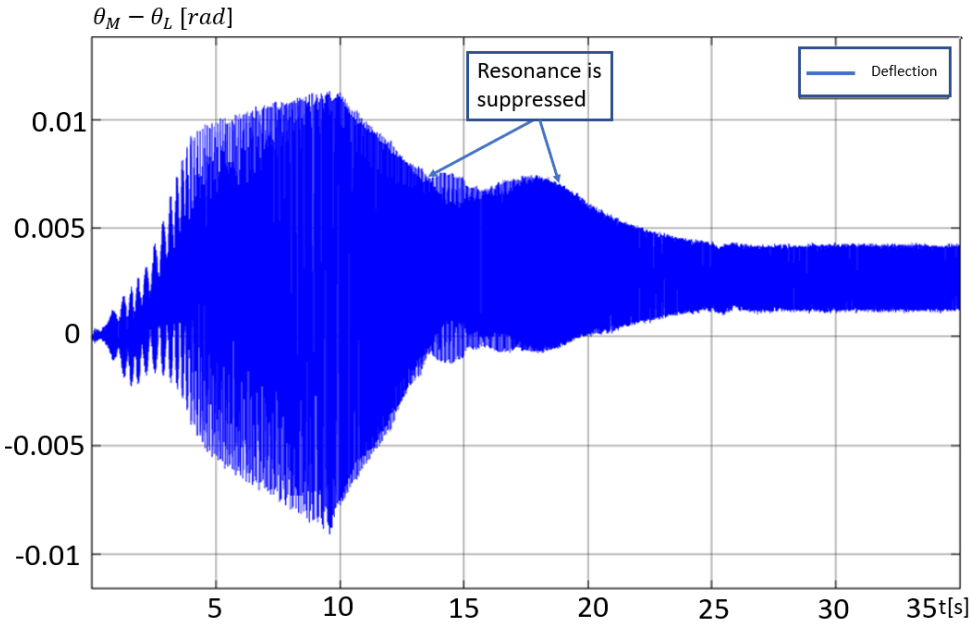

Figure 5-23 Angular deflection of test 1 with observer 1

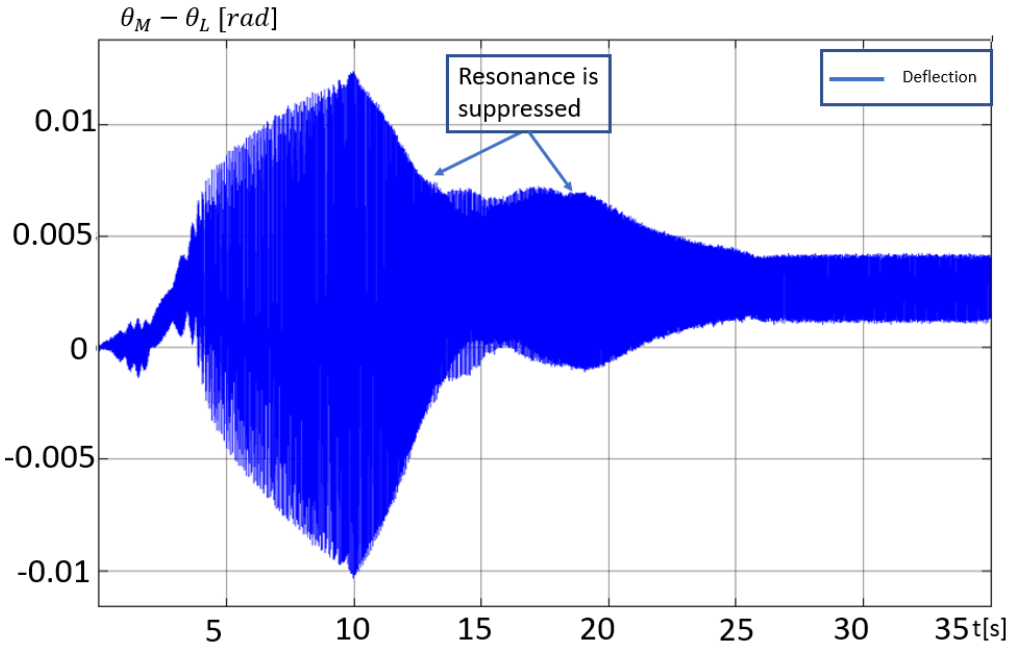

Figure 5-24 Angular deflection of test 1 with observer 2

5.2.5.2 Test 2: Two-mass mechanical model, the first reference speed signal

In this test, more realistic simulation is performed where the speed feedback signal is taken from the two-mass mechanical system model instead of the one-mass. Other simulation parameters, such as the PI regulator parameter of both the speed and current controllers are left unchanged. The motor speed (ω_M) now will be included along with the same reported figures of test 1.

5.2.5.2.1 Base model response

The motor speed (ω_M) and the load speed (ω_L) are reported side by side in Figure 5-25. It can be noticed that the motor speed experiences large oscillations compared to the stability of the load speed. In contrast to the first test, now the resonance intersections can be noticed by a sudden increase in the motor speed oscillation reaching a peak at $t_1 = 14.55s$ and $t_2 = 21.84s$. These angular increments appear to be damped in two seconds, as the control system attempts to follow the reference speed again once the resonance intersection has been passed. The resonance is also affecting the load speed but at a lower rate as it can be seen in the figure below. The same behaviour of speed sags of test 1 is experienced at $t = 1.5s$ once the load torque is inserted in the system.

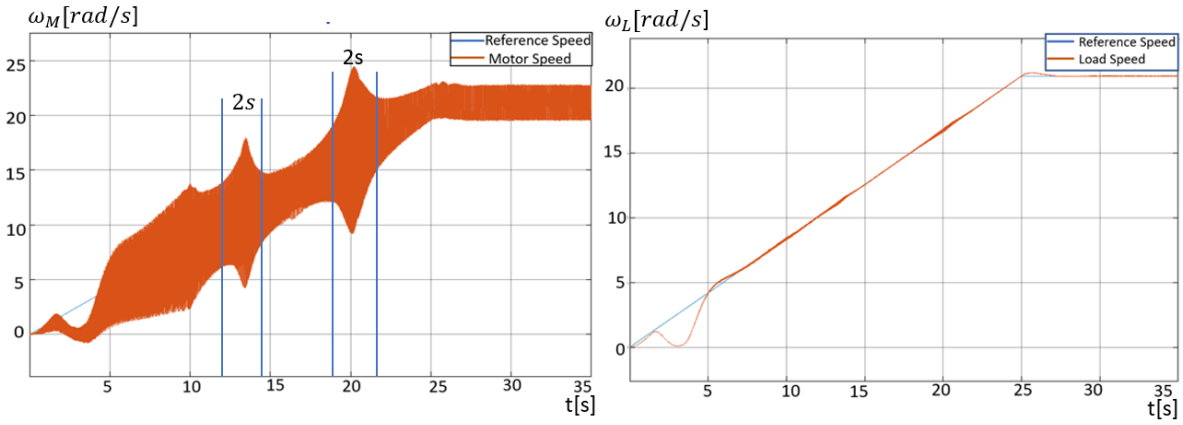

Figure 5-25 Reference speed, motor speed (left), and load speed (right) of the two-mass system of test 2

The same effect of resonance is mirrored on the angular deflection in Figure 5-26 and Figure 5-27 for the two observer pole choices, where the large peaks are presented when the system speed crosses the critical points. The first surge peaks at $0.012\,rad$ at $14s$ and the second angular increment reaches around $0.015\,rad$ at around $t = 22s$. The observer estimation accuracy shows a similar behaviour of the constant error which was explained in the first test. However, there a significant difference in the error at steady state error since the angular deflection value is no longer have a large magnitude. The estimation error of observer 1 is:

$$e_{obs1} = \frac{1.617 * 10^{-3} rad}{4.094 * 10^{-3} rad} = 39.50 * 10^{-2} \tag{5-61}$$

And the second:

$$e_{obs2} = \frac{2.606 * 10^{-3} rad}{4.406 * 10^{-3} rad} = 59.15 * 10^{-2} \tag{5-62}$$

The observer estimation error for the two cases differ by approximately 20%. A similar behaviour to test 1 is evident regarding the peak to peak oscillation error at steady state, where the first case shows of approximately $2 * 10^{-3}\,rad$ compared to the latter case with $0.5 * 10^{-3}\,rad$.

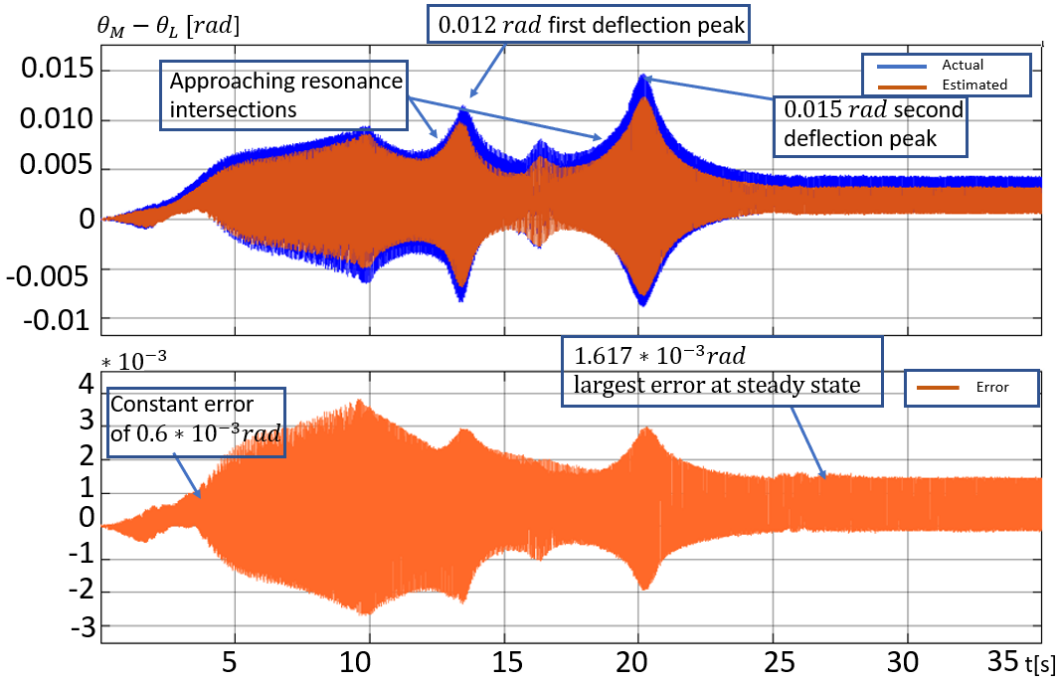

Figure 5-26 Actual and estimated Angular deflection (top) and the estimation error (bottom) of test 2 of first observer poles

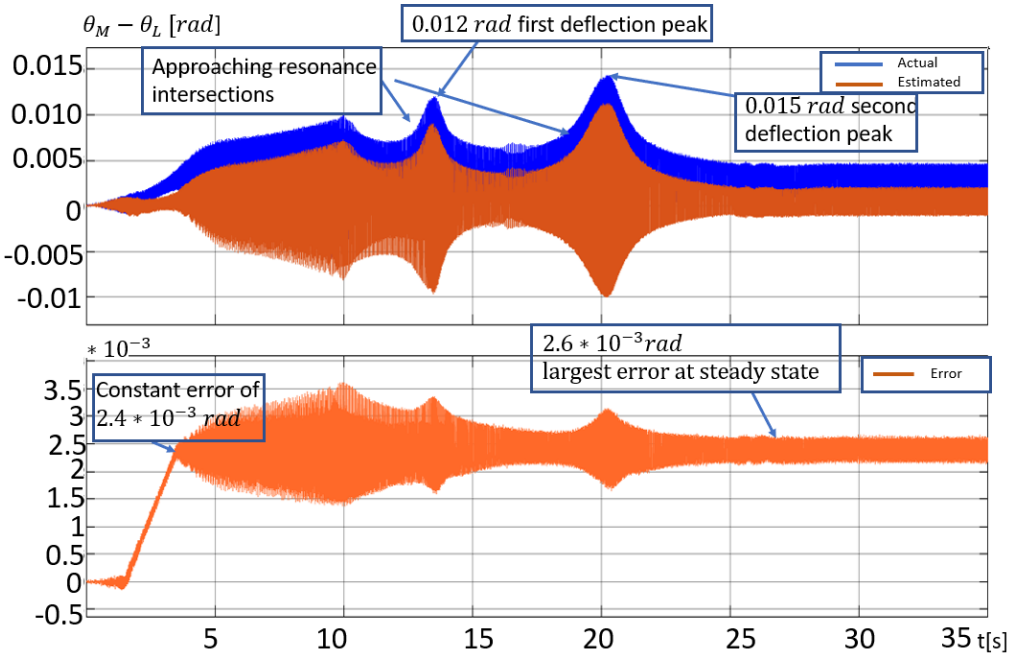

Figure 5-27 Actual and estimated Angular deflection (top) and the estimation error (bottom) of test 2 of second observer poles

5.2.5.2.2 Compensated response

With the same configuration of test 1, the feedforward compensation from observer estimated torsional torque is applied. Again, for the sake of comparison the results of the two observer settings are reported.

As it can be noticed the resonance excitations from the 12th and 18th harmonic are completely suppressed and cannot be seen in the motor speed in the Figure 5-28 and Figure 5-29. The

control system is able to suppress the resonance effects immediately and no increase in the motor speed is experienced. The two choices of observer gains show identical behaviour in the effectiveness of cancelling the disturbance as it was concluded in the first test.

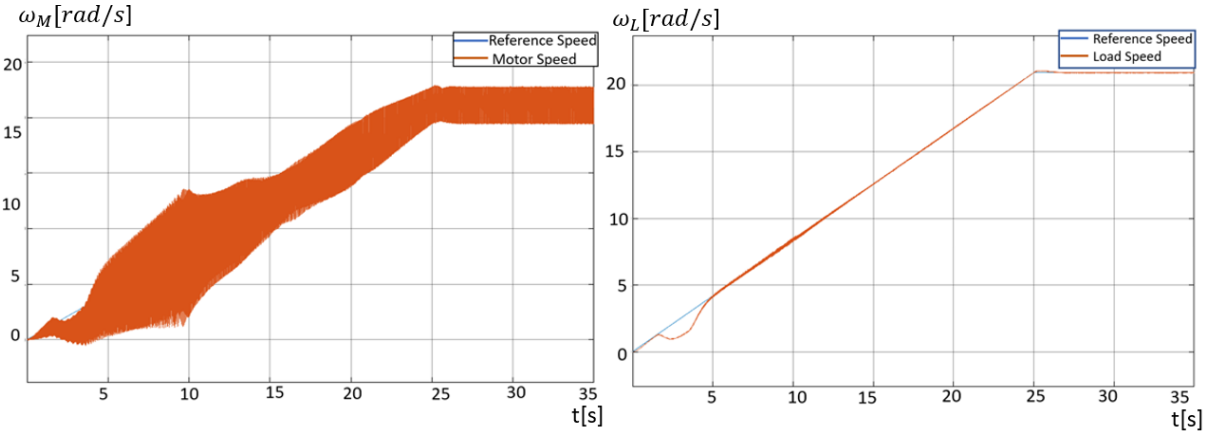

Figure 5-28 Reference speed, motor speed (left), and load speed (right) of the two-mass system of test 2 with observer 1

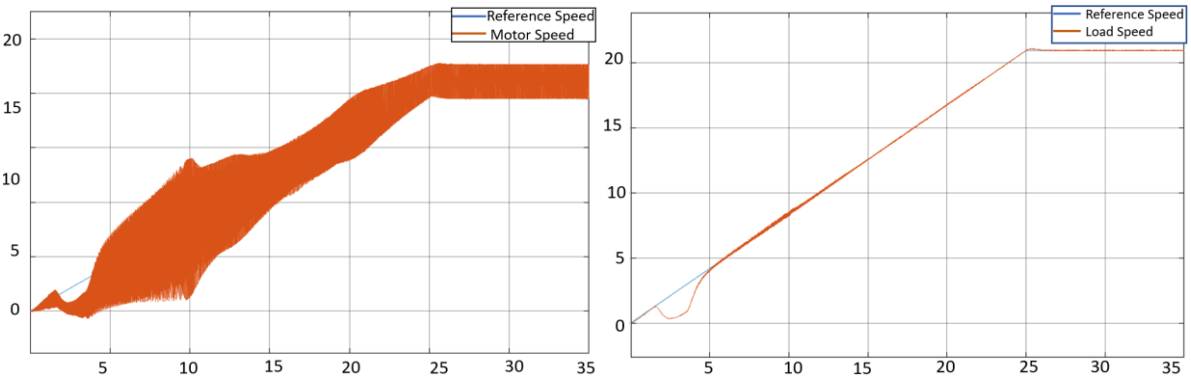

Figure 5-29 Reference speed, motor speed (left), and load speed (right) of the two-mass system of test 2 with observer 2

The angular deflection values from Figure 5-30 and Figure 5-31, show an identical behaviour to test 1, where the arrows on the figures indicate where the peaks were supposed to be, as in baseline system response shown in Figure 5-26. The feedforward compensation action has decreased the torsional angle from $0.012\,rad$ to approximately $0.006\,rad$ for the first resonance and the second resonance intersection peak has been decreased from $0.015\,rad$ to around $0.0055\,rad$. At first glance, the observer poles placement has little to no effect on the torsional vibration suppression. However, the design criteria where the poles should be two to five times larger than the inner loops poles of the control system still hold as it determines the stability of the observer.

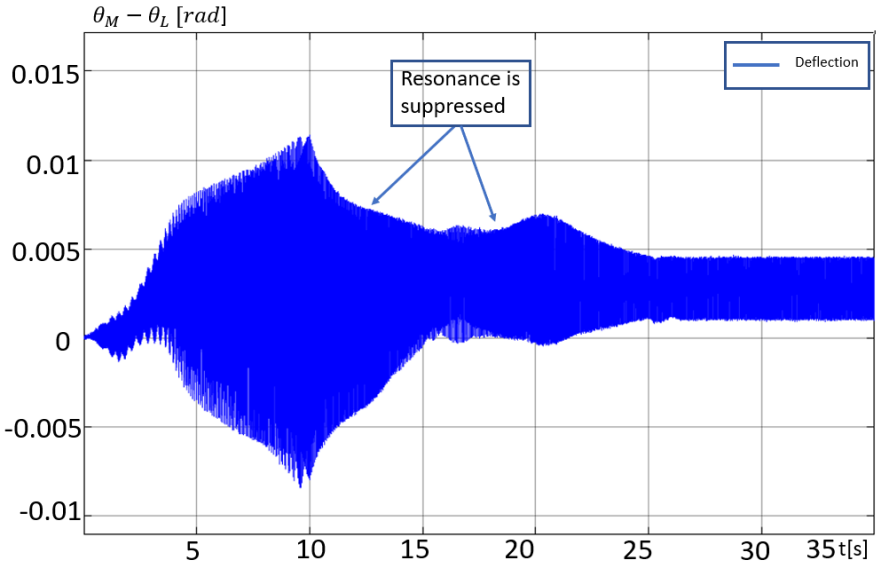

Figure 5-30 Angular deflection of test 2 with observer 1

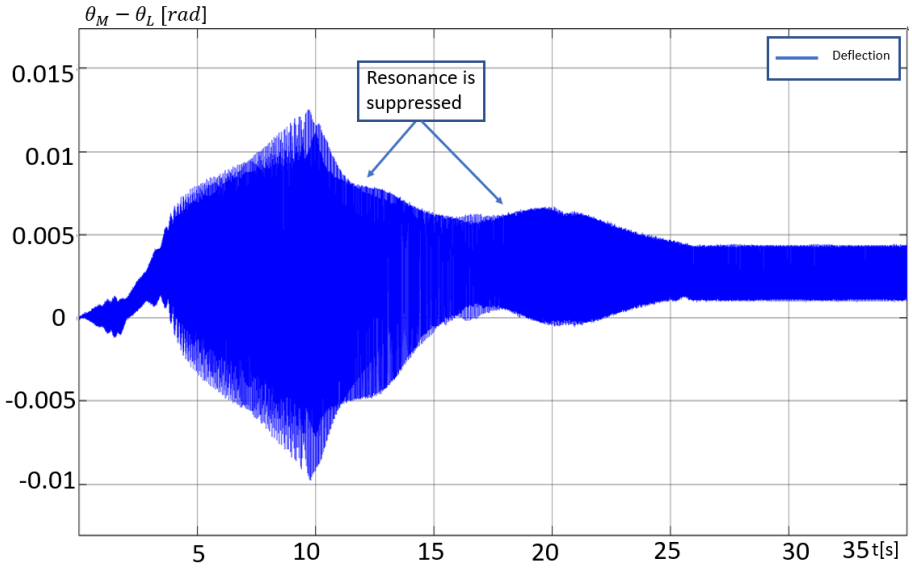

Figure 5-31 Angular deflection of test 2 with observer 2

5.2.5.3 Test 3: Two separated mechanical models, second reference speed signal

In the second half of the simulation tests, once again the system has two separated mechanical system as represented in Figure 5-16 but the reference signal has been modified to be as specified in Figure 5-14. We are interested in studying the system under steady state of torsional resonance, in contrast to the first reference speed signal where the resonance intersections were only passed through.

5.2.5.3.1 Base model response

The base response of one-mass speed (ω) and two-mass load speed (ω_L) of the two mechanical models configuration is reported in Figure 5-32. From the load speed plot , it can be noticed that the mechanical system approaches the first resonance at around $t_1 = 13s$, and a sudden

increase is experienced in the angular deflection and it remains since no damping exists in the system. At time $19s$ the system approaches the second resonance condition and the beating phenomenon occurs. Once the system reaches steady state the resonance condition is met, and the angular deflection is largely increased over time. On the other hand, the speed of the one-mass system (ω) is following the reference speed as intended.

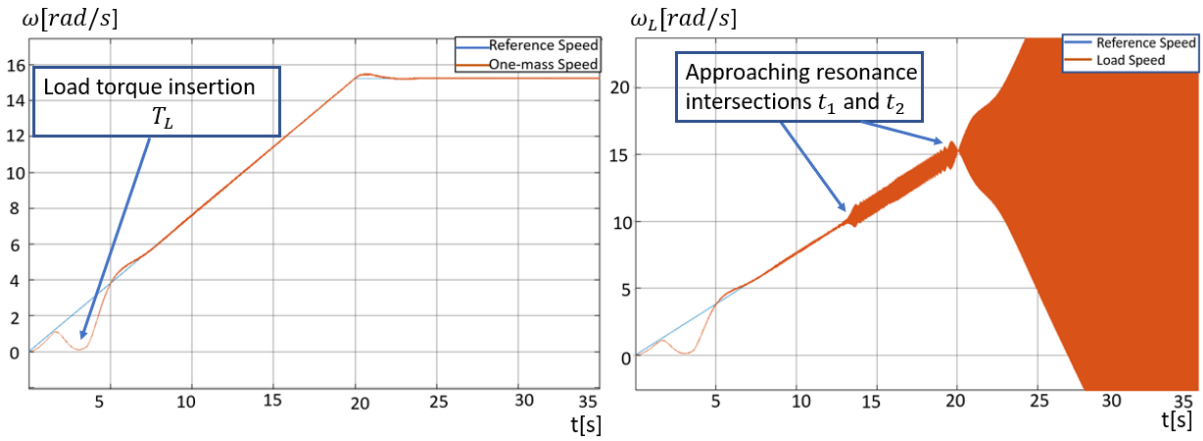

Figure 5-32 Reference speed, one-mass speed (left), and load speed of the two-mass system (right) of test 3

The angular deflection measurements are reported in Figure 5-33 and Figure 5-34 for both of the observer poles selections, which show the same behaviour of what was reported for load speed. The observer estimation accuracy remains at the same level of what was calculated in test 1.

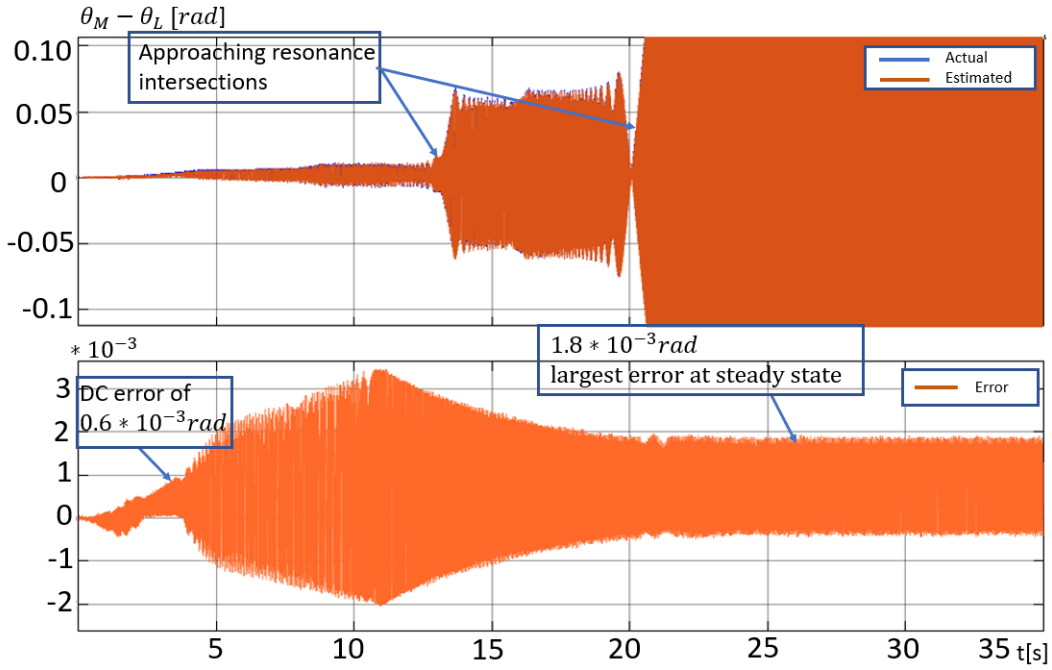

Figure 5-33 Actual and estimated angular deflection (top) and the estimation error (bottom) of test 3 of first observer poles

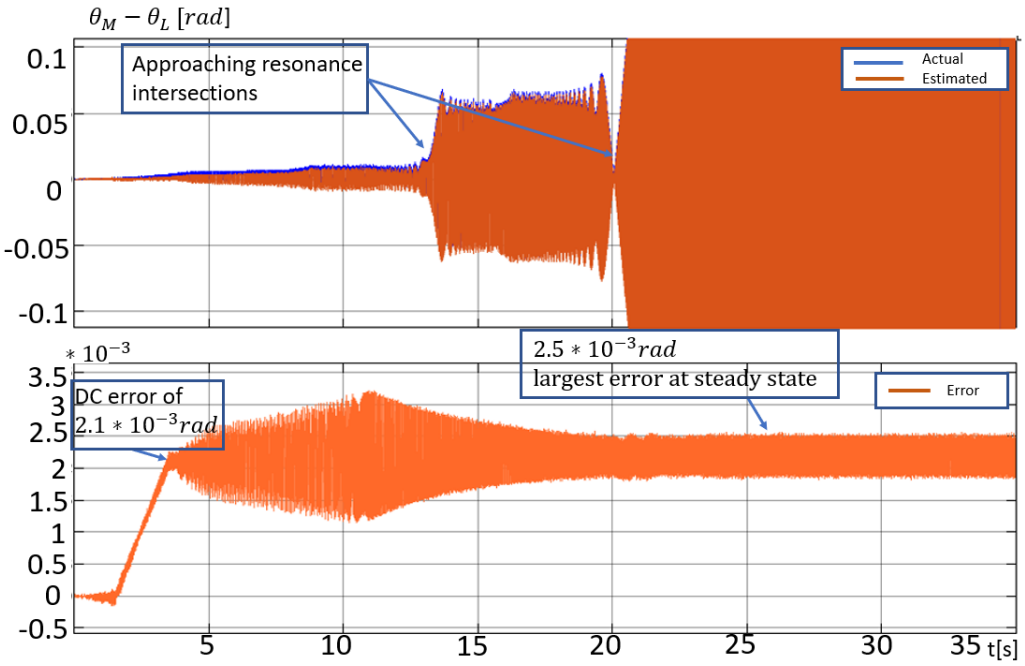

Figure 5-34 Actual and estimated angular deflection (top) and the estimation error (bottom) of test 3 of second observer poles

5.2.5.3.2 Compensated response

The feedforward compensation is as well implemented to test if the system is able to avoid the steady-state resonance condition. For the sake of comparison the pole placement of observer 1 and observer 2 are simulated and produces the speed responses given in Figure 5-35 and Figure 5-36, respectively. As expected, the feedforward compensation action is able to suppress the first resonance intersection at $t_1 = 13.32s$, and avoid the steady-state resonance condition to happen at $t_2 = 20s$. Hence, the system is able to operate at that critical speed without experiencing the resonance effects. Once again, the estimation accuracy of the two choices of observer poles has little effect on the results of the torsional vibration suppression.

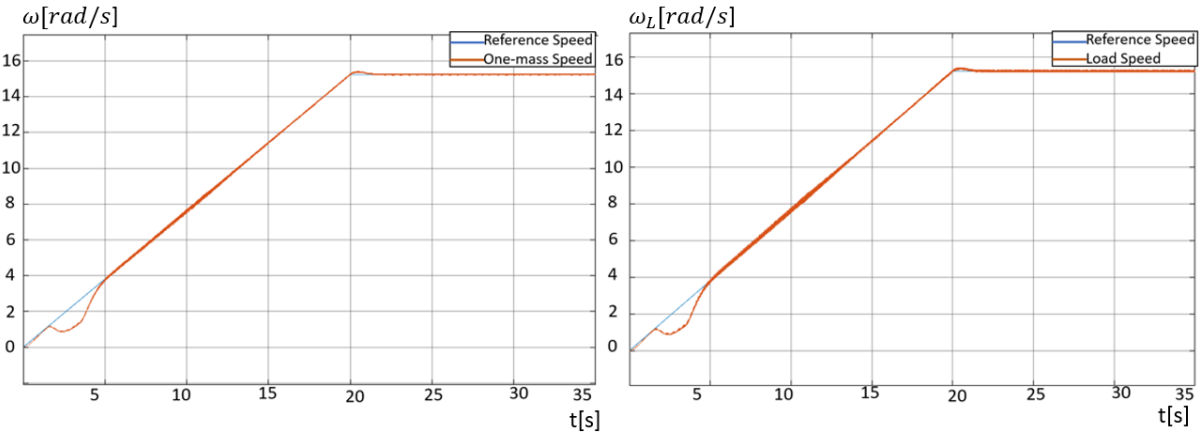

Figure 5-35 Reference speed, one-mass speed (left), and load speed of the two-mass system (right) of test 3 with observer 1

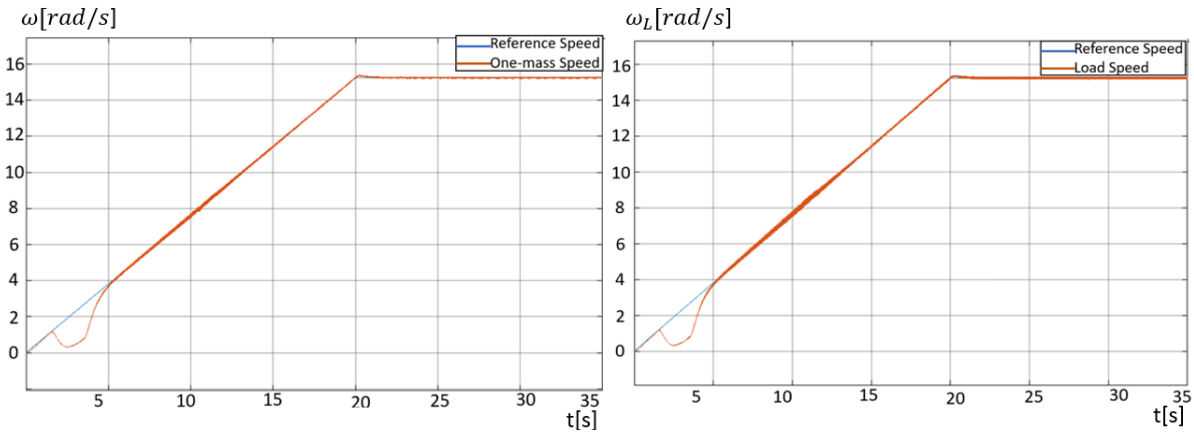

Figure 5-36 Reference speed, one-mass speed (left), and load speed of the two-mass system (right) of test 3 with observer 2

An analogous behaviour is represented in the angular deflection plots in Figure 5-37 and Figure 5-38, where the resonance condition has been completely avoided. As well as the first resonance peak has been decreased from around $0.06\ rad$ seen in Figure 5-33 to approximately $0.007\ rad$ for the both cases.

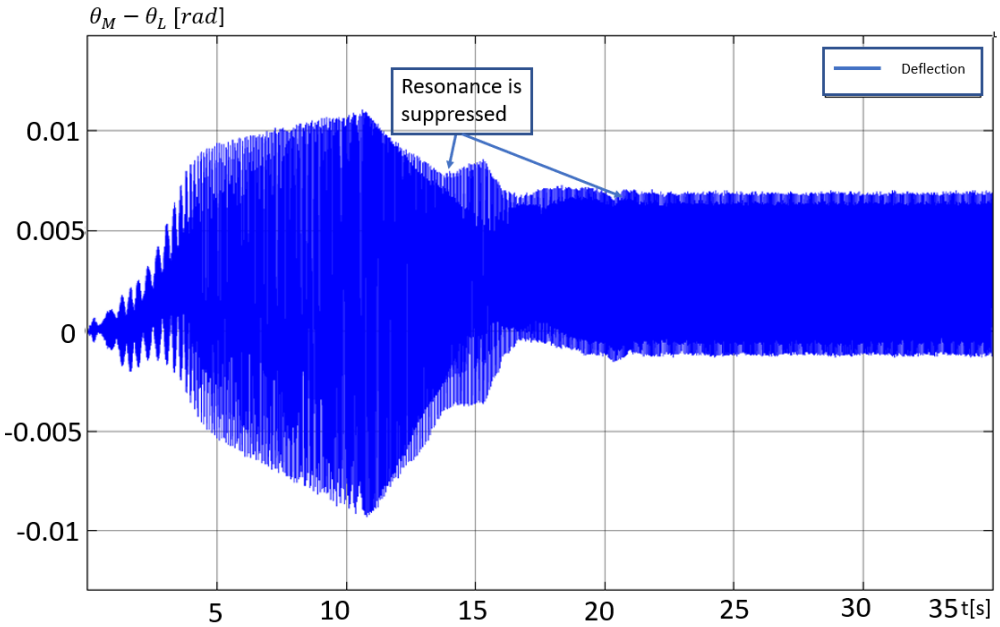

Figure 5-37 angular deflection of test 3 with observer 1

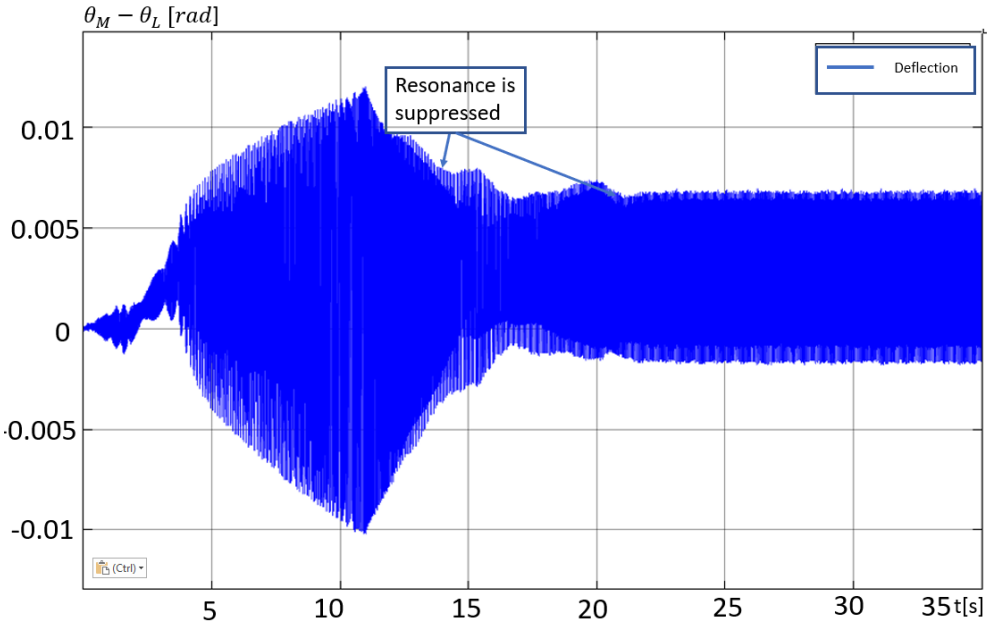

Figure 5-38 angular deflection of test 3 with observer 2

5.2.5.4 Test 4: Two-mass mechanical model, second reference speed signal

The final test 4 is conducted to show how a practical system of two masses with an elastic coupling behaves under the resonance condition of the second reference signal.

5.2.5.4.1 Base model response

For the normal system response without the addition of the feedforward compensating, the motor speed (ω_M) and load speed (ω_L) are reported in Figure 5-39, and the angular deflection in Figure 5-40 and Figure 5-41. It can be noticed that the first resonance point is crossed, and a sudden increase in the motor speed and the angular deflection is present. However, when the system reaches the second critical point, where the mechanical resonance is excited by the 12th harmonic the speed PI control is able to avoid the resonance and suppresses it, in contrast to the case seen in the 3rd test where the angular deflection increases uncontrollably.

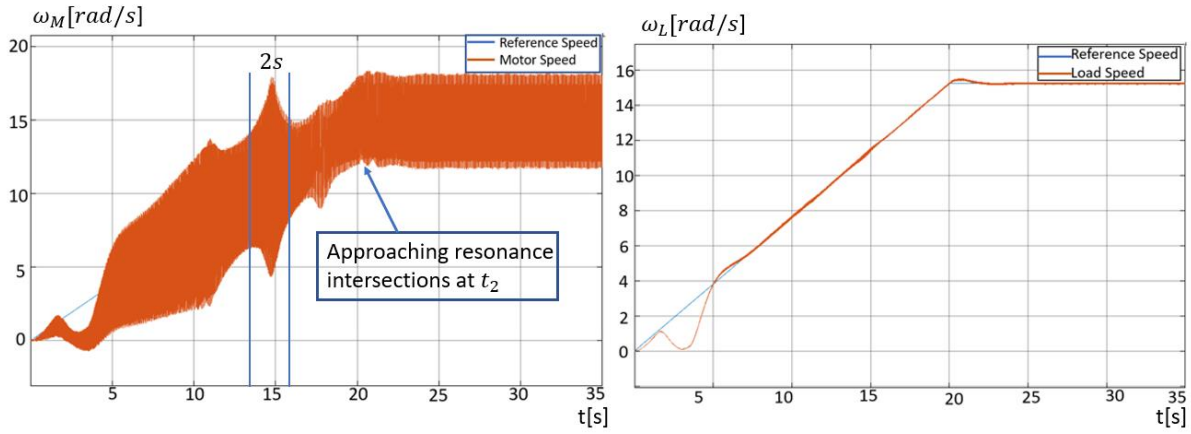

Figure 5-39 Reference speed, motor speed (left), and load speed (right) of the two-mass system of test 4

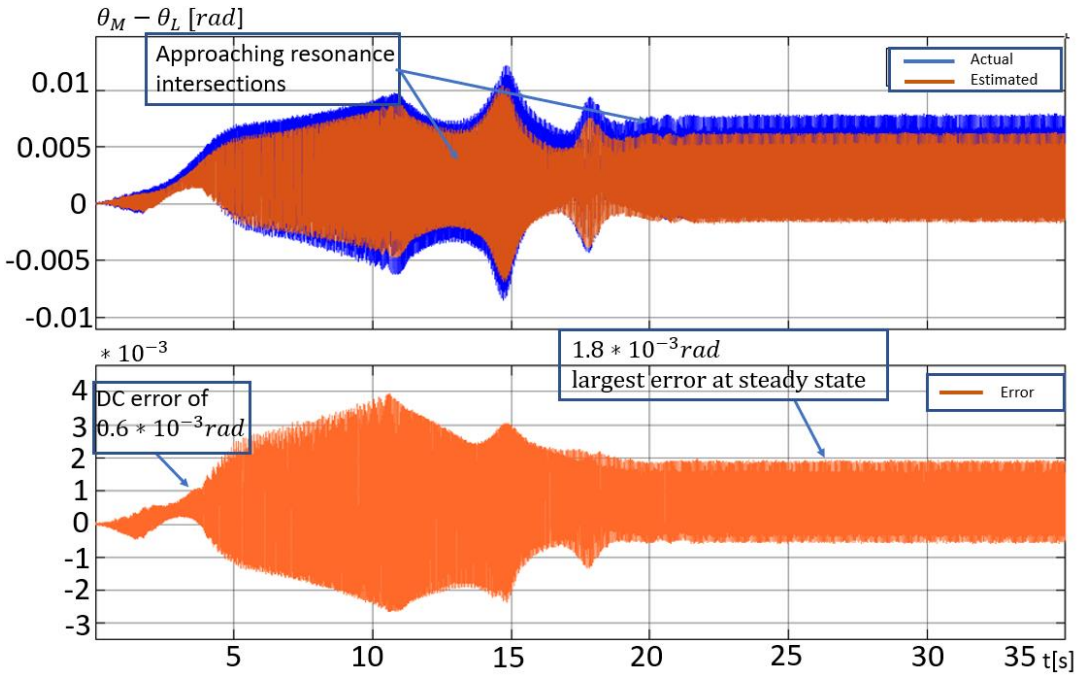

Figure 5-40 Actual and estimated Angular deflection (top) and the estimation error (bottom) of test 4 of first observer poles

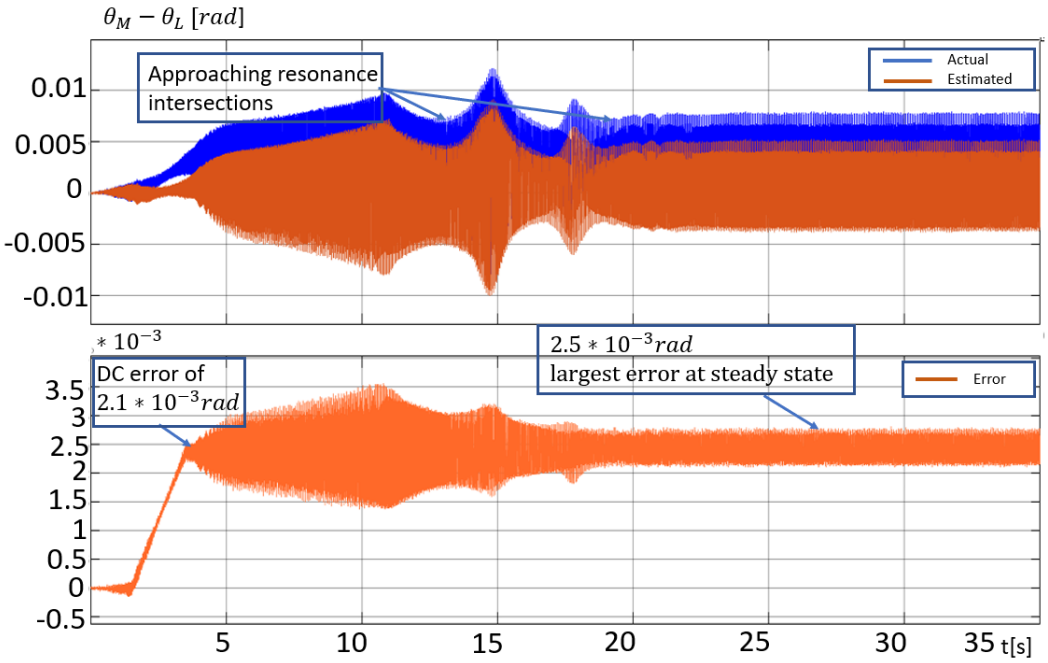

Figure 5-41 Actual and estimated Angular deflection (top) and the estimation error (bottom) of test 4 of second observer poles

5.2.5.4.2 Compensated response

Finally, the feedforward compensation is tested for this particular system configuration. The compensation is done twice, similarly to the previous tests for the two observer poles.

The speed responses in Figure 5-42 and Figure 5-43, shows a positive result by suppressing the first resonance intersection instantly and completely damp it. In addition, the machine is still able to operate at the steady state resonance condition when it reaches $t = 20s$. Hence, the baseline is not affected negatively by the compensation action.

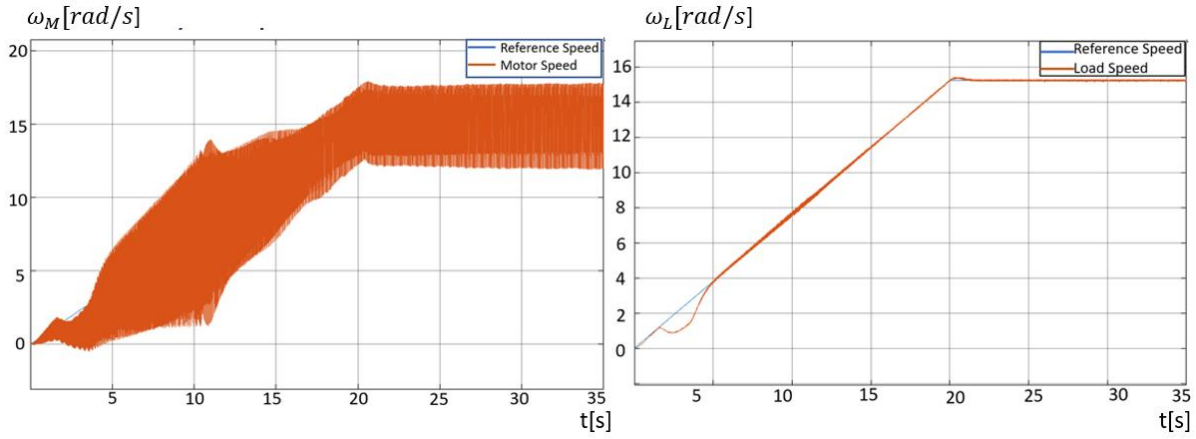

Figure 5-42 Reference speed, motor speed (left), and load speed (right) of the two-mass system of test 4 with observer 1

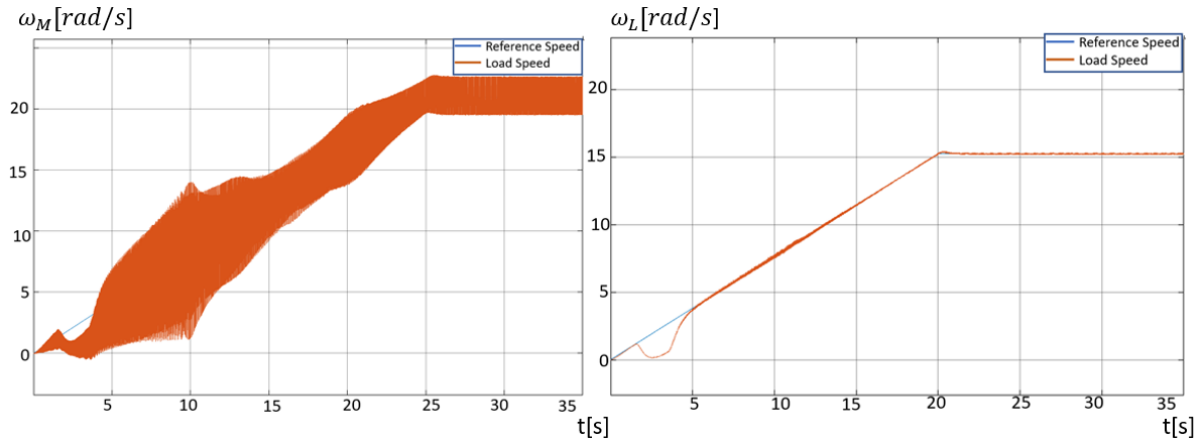

Figure 5-43 Reference speed, motor speed (left), and load speed (right) of the two-mass system of test 4 with observer 2

The result of the feedforward compensation of the two-mass system for the angular deflection values in Figure 5-44 and Figure 5-45, shows the effectiveness of the system to supress the torsional resonance for the first intersection near $t = 14s$, in fact the torsional angle has been decreased from around $0.0125\,rad$ to about $0.0068\,rad$ as can be noticed by comparing Figure 5-43 and Figure 5-40. A small change in the steady-state angular deflection can be noticed from around $0.0072\,rad$ from Figure 5-40 to $0.0053\,rad$ in Figure 5-45.

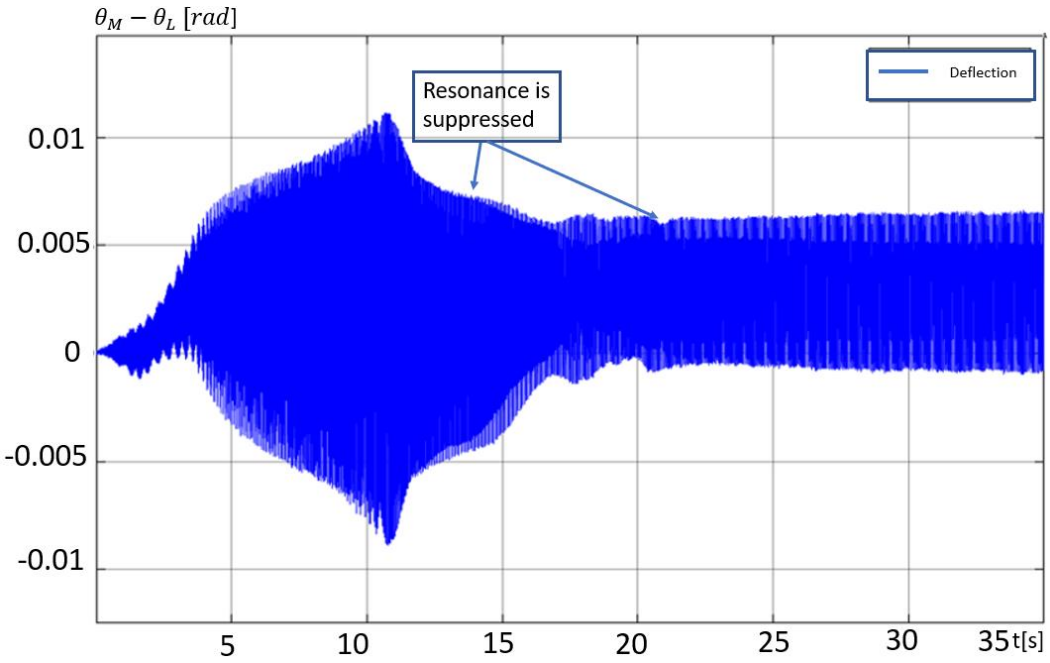

Figure 5-44 angular deflection of test 4 with observer 1

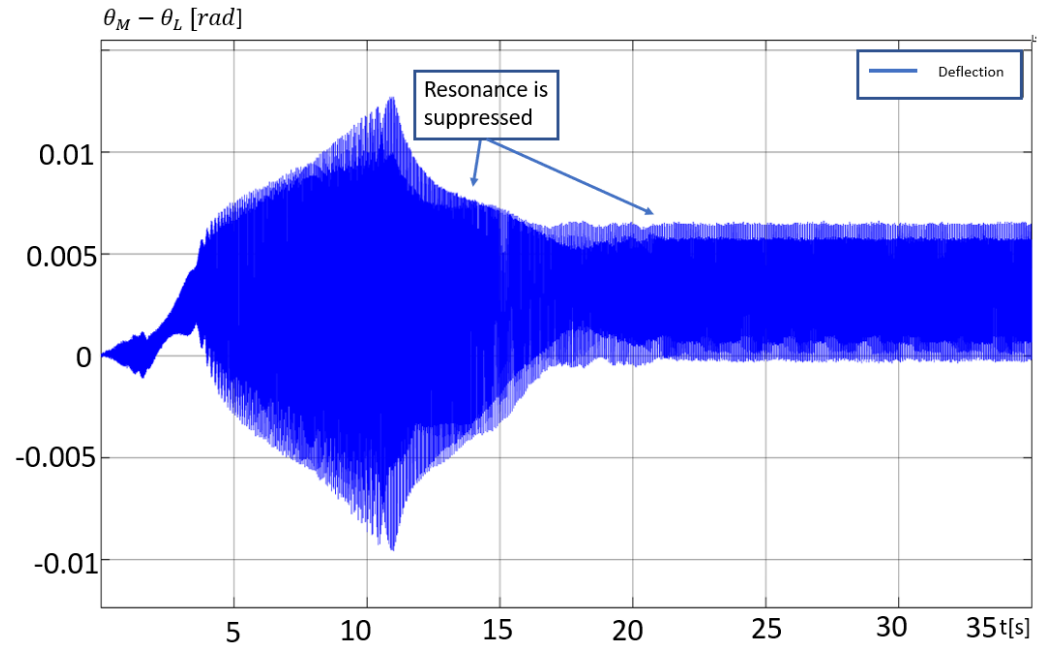

Figure 5-45 angular deflection of test 4 with observer 2

5.2.6 Nonlinear extended state observer formulation

In this section an alternative approach to disturbance estimation is explained, which is the nonlinear extended state observer. As for the linear Luenberger observer, the system parameters must be known in order to construct it. For example, the load inertia J_L was much involved in designing the observer from the system matrix $\boldsymbol{A}$ in the general formula for the observer system in (5-43). The load inertia was not only necessary for the observer design, but as well for the calculation of the gain coefficient for the observer gain vector (5-53). Hence, complete knowledge of the plant is necessary in advance before the implementation of such an

observer. The alternative approach with the nonlinear extended state observer shows a different way of designing the observer to avoid much information about the plant.

This type of observer follows a different formulation direction other than the state space representation which was followed for the Luenberger observer. In contrast, it is described by differential equations. If we consider a class of SISO system of order n depicted by the following:

$$y^{(n)}(t) = a(t) + bu(t) \tag{5-63}$$

Where the superscript denotes the n time derivative, $y(t)$ the controlled output, $u(t)$ the control input, b the output system parameter, and $a(t)$ the lumped disturbances which can consist of the external and the internal disturbances depending on the observer formulation. To simplify the notation, the time variable will be dropped. Letting

$$x_1 = y, x_2 = \dot{y}, \dots, x_n = y^{(n-1)} \tag{5-64}$$

then the system is described as [16][27]:

$$\begin{cases} \dot{x}_1 = x_2 \\ x_2 = x_3 \\ \vdots \\ \dot{x}_{n-1} = x_n \\ \dot{x}_n = a(t) + bu \\ y = x_1 \end{cases} \tag{5-65}$$

Now the following extra state, i.e., "extended state" is usually introduced into the framework of the state observer:

$$x_{n+1} = a(t) \tag{5-66}$$

The nonlinear term $a(t)$ from the system equation (5-65) can now be simplified by substituting (5-65) into it; we obtain the extended-state equation:

$$\begin{cases} \dot{x}_1 = x_2 \\ \dot{x}_2 = x_3 \\ \vdots \\ \dot{x}_{n-1} = x_n \\ \dot{x}_n = a(t) + bu \\ \dot{x}_{n+1} = h(t) \\ y = x_1 \end{cases} \tag{5-67}$$

Where

$$h(t) = \dot{a}(t)$$

Since the system is in the correct format of the extended state observer, it is possible to estimate the extended state by using the extended state observer represented in Figure 5-46. The observer system takes the form:

$$\begin{cases} \dot{z}_1 = z_2 - \beta_1 g(z_1 - y) \\ \dot{z}_2 = z_3 - \beta_2 g(z_1 - y) \\ \vdots \\ \dot{z}_n = z_{n+1} - \beta_n g(z_1 - y) + bu \\ \dot{z}_{n+1} = -\beta_{n+1} g(z_1 - y) \end{cases} \tag{5-68}$$

The observer form in (5-68) consists of two parts:

- the states z_1, z_2, …, z_n and z_{n+1}, which are the estimates of the original plant states $x_1, x_2, \dots, x_n$, and x_{n+1}.
- the correction terms $\beta_1 g(z_1 - y)$, $\beta_2 g(z_1 - y)$, $\beta_n g(z_1 - y)$, and $\beta_{n+1} g(z_1 - y)$. These correction terms allow the observer to follow the system states depending on the observation error from the repeated term $(z_1 - y)$. The nonlinear function $g(.)$ gives the name for the "nonlinear extended state observer" and its purpose is to increase the efficiency of the observer by having a nonlinear function with higher gains and smaller errors. The general rule is to choose the function $g(.)$ based on experiments. Finally the nonlinear function is multiplied by the observer gains noted by $\beta_1, \beta_2, \dots, \beta_n$, and β_{n+1}; they are to be designed in the same manner as the Luenberger observer gains.

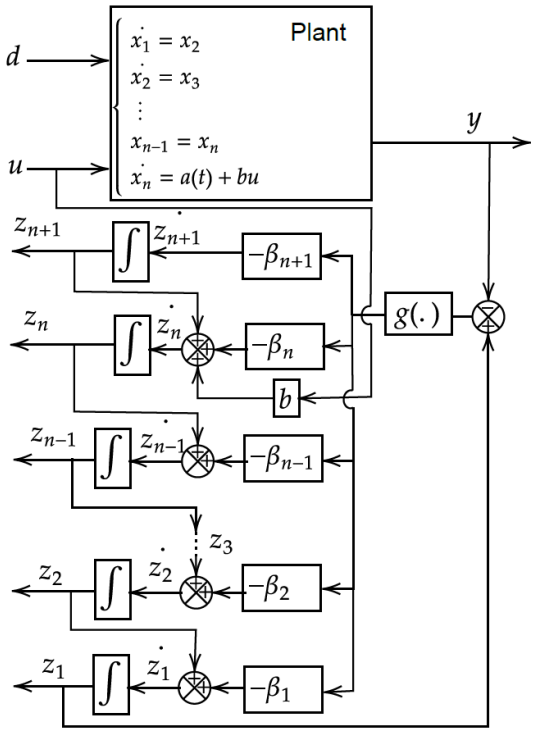

Figure 5-46 Block diagram of the nonlinear extended state observer

5.2.7 Nonlinear extended state observer design

For this type of observer, we recall the two-mass mechanical system represented in the second chapter:

Motor side: $$J_M(\dot{\omega_M}) + B_M \omega_M = T_M - T_s$$

Load side: $$J_L(\dot{\omega_L}) + B_L\omega_L = -T_L + T_s$$

Torsional torque: $$T_s = K_s(\theta_M - \theta_L) + B(\omega_M - \omega_L)$$

Neglecting the damping of the system, the previous equations become:

Motor side: $$J_M(\dot{\omega_M}) = T_M - T_s$$

Load side: $$J_L(\dot{\omega_L}) = -T_L + T_s \quad (5\text{-}69)$$

Torsional torque: $$T_s = K_s(\theta_M - \theta_L)$$

The damping negligence has been justified in the Sect 2.1. In addition, for the sake of comparison the extended state observer will be designed for the same simulation configuration of the Luenberger observer where all damping parameters were set to zero. Firstly, the state variables of system $(x_1, x_2, \dots, x_n)$ must be set to comply the general form of (5-65). In this thesis, we choose:

$$x_1 = \theta_m \;\; x_2 = \omega_m \quad (5\text{-}70)$$

which makes a proper choice for the next step. From the previous state variables, the output is:

$$y = x_1 = \theta_m \quad (5\text{-}71)$$

Similar to the linear observer, the control variable u is set as the motor torque reference T_{Mref}:

$$u = T_{Mref} \quad (5\text{-}72)$$

and the control coefficient:

$$b = 1/J_M \quad (5\text{-}73)$$

Since all state variables and coefficient have been identified, it is possible to write our system in the same form of equation (5-65) as:

$$\begin{cases} \dot{\theta}_M = \omega_m \\ \dot{\omega}_M = -\dfrac{K_S}{J_M}(\theta_M - \theta_L) + \dfrac{1}{J_M}T_{Mref} \\ y = \theta_m \end{cases} \quad (5\text{-}74)$$

where

$$a(t) = -\frac{K_S}{J_M}(\theta_M - \theta_L) \quad (5\text{-}75)$$

is an unknown quantity.

Now a third order extended state observer can be constructed by using (5-67). Setting:

$$x_3 = a(t) \quad (5\text{-}76)$$

we have the extended system:

$$\begin{cases} \dot{\theta}_M = \omega_M \\ \dot{\omega}_M = a(t) + \dfrac{1}{J_M} u \\ \dot{a}(t) = h(t) \\ y = x_1 \end{cases} \tag{5-77}$$

and the observer for the extended system is expressed as (5-78), where the nonlinear function $g(.)$ is set as (5-79) [17]:

$$\begin{cases} \dot{z}_1 = z_2 - \beta_1 g(z_1 - y) \\ \dot{z}_2 = z_3 - \beta_2 g(z_1 - y) + bu \\ \dot{z}_3 = -\beta_3 g(z_1 - y) \end{cases} \tag{5-78}$$

$$g(x) = \frac{e^x - e^{-x}}{2} = \sinh(x) \tag{5-79}$$

The nonlinear function was chosen from the reference [17], due to the fact that this function initially requires experiments to be set. Hence it was used as a starting point. In addition, the paper in the reference is analysing a system which has similar configurations compared to our system to some degree. By substituting our system variables in (5-78), we have:

$$\begin{cases} \dot{\hat{\theta}}_M = \hat{\omega}_M - \beta_1 g\left(\hat{\theta}_M - \theta_M\right) \\ \dot{\hat{\omega}}_M = \hat{a}(t) - \beta_2 g\left(\hat{\theta}_M - \theta_M\right) + \dfrac{1}{J_M} T_{Mref} \\ \dot{\hat{a}}(t) = -\beta_3 g\left(\hat{\theta}_M - \theta_M\right) \end{cases} \tag{5-80}$$

Where $a(t)$ is given by (5-75). The observer gains β_1, β_2 and β_3 can be found in similar manner as for the linear observer with the direct pole placement method. Subtracting (5-77) from (5-80) yields:

$$\begin{bmatrix} \dot{\hat{\theta}}_M - \dot{\theta}_M \\ \dot{\hat{\omega}}_M - \dot{\omega}_M \\ \dot{\hat{a}}(t) - \dot{a}(t) \end{bmatrix} = \begin{bmatrix} 0 & 1 & 0 \\ 0 & 0 & 1 \\ 0 & 0 & 0 \end{bmatrix} \begin{bmatrix} \hat{\theta}_M - \theta_M \\ \hat{\omega}_M - \omega_M \\ \hat{a}(t) - a(t) \end{bmatrix} - \begin{bmatrix} \beta_1 \\ \beta_2 \\ \beta_3 \end{bmatrix} g\left(\hat{\theta}_M - \theta_M\right) + \begin{bmatrix} 0 \\ 0 \\ -h(t) \end{bmatrix}$$

$$[\dot{\boldsymbol{e}}] = A_e[\boldsymbol{e}] - \boldsymbol{\beta} \cdot g\left(\hat{\theta}_M - \theta_M\right) + \begin{bmatrix} 0 \\ 0 \\ -h(t) \end{bmatrix} \tag{5-81}$$

$$\hat{y} - y = \begin{bmatrix} 1 & 0 & 0 \end{bmatrix} \begin{bmatrix} \hat{\theta}_M - \theta_M \\ \hat{\omega}_M - \omega_M \\ \hat{a}(t) - a(t) \end{bmatrix} = \boldsymbol{C}[\boldsymbol{e}]$$

Where $\hat{y} - y = \hat{\theta}_M - \theta_M$, and the system matrix A can be recognized from the previous matrices as:

$$\boldsymbol{A_e} = \begin{bmatrix} 0 & 1 & 0 \\ 0 & 0 & 1 \\ 0 & 0 & 0 \end{bmatrix}$$

The subscript e is to distinguish the matrices from the previous linear observer design. However, the matrix $\boldsymbol{C}$ is identical. The observer gain matrix can be set as:

$$\boldsymbol{\beta} = \begin{bmatrix} \beta_1 \\ \beta_2 \\ \beta_3 \end{bmatrix}$$

To design the coefficients of vector $\boldsymbol{\beta}$, the same steps of the pole placement method (Sect. 5.2.3) could be followed. At first, Taylor's series expansion of $g(x)$ around the initial position (x_0=0) yields:

$$\sinh(x)|_{x0=0} \approx x$$

Thus:

$$g(\hat{\theta}_M - \theta_M) \approx (\hat{\theta}_M - \theta_M) \tag{5-82}$$

and (5-81) becomes:

$$[\dot{\boldsymbol{e}}] = A_e[\boldsymbol{e}] - \boldsymbol{\beta} C[\boldsymbol{e}] + \begin{bmatrix} 0 \\ 0 \\ -h(t) \end{bmatrix}$$

The last vector in the previous equation can be considered as an input; thus it does not influence the stability of this differential equation system and the direct pole placement method can be proceed.

$$|s\boldsymbol{I} - (\boldsymbol{A_e} - \boldsymbol{\beta C})| = (s-\mu_1)(s-\mu_2)(s-\mu_3)$$

$$\left|\begin{bmatrix} s & 0 & 0 \\ 0 & s & 0 \\ 0 & 0 & s \end{bmatrix} - \left(\begin{bmatrix} 0 & 1 & 0 \\ 0 & 0 & 1 \\ 0 & 0 & 0 \end{bmatrix} - \begin{bmatrix} \beta_1 \\ \beta_2 \\ \beta_3 \end{bmatrix} [1 \quad 0 \quad 0]\right)\right| = (s+\alpha_{\text{ext}})(s^2 + 2\zeta\omega_{\text{ext}}s + \omega_{\text{ext}}^2)$$

$$\left|\begin{bmatrix} s & 0 & 0 \\ 0 & s & 0 \\ 0 & 0 & s \end{bmatrix} - \left(\begin{bmatrix} 0 & 1 & 0 \\ 0 & 0 & 1 \\ 0 & 0 & 0 \end{bmatrix} - \begin{bmatrix} \beta_1 & 0 & 0 \\ \beta_2 & 0 & 0 \\ \beta_3 & 0 & 0 \end{bmatrix}\right)\right| = (s+\alpha_{\text{ext}})(s^2 + 2\zeta\omega_{\text{ext}}s + \omega_{\text{ext}}^2)$$

$$\begin{vmatrix} s+l_1 & -1 & 0 \\ l_2 & s & -1 \\ l_3 & 0 & s \end{vmatrix} = (s+\alpha_{\text{ext}})(s^2 + 2\zeta\omega_{\text{ext}}s + \omega_{\text{ext}}^2)$$

$$s^3 + \beta_1 s^2 + \beta_2 s + \beta_3$$
$$= s^3 + (2\zeta_{ext}\omega_{ext} + \alpha_{ext})s^2 + (2\zeta\omega_{ext}\alpha_{ext} + \omega_{ext}^2)s + \omega_{ext}^2\alpha_{ext}$$

$$\beta_1 = 2\zeta_{ext}\omega_{ext} + \alpha_{ext}$$

$$\beta_2 = 2\zeta\omega_{ext}\alpha_{ext} + \omega_{ext}^2 \tag{5-83}$$

$$\beta_3 = \omega_{ext}^2\alpha_{ext}$$

The parameters α_{ext}, ω_{ext}, and ζ_{ext} follow the same rules that have been explained in detail in linear observer analysis. Hence, the poles are set as the second choice of the previously designed Luenberger observer, i.e., to have the cutoff frequency two times higher than the cutoff frequency of the current regulator ω_{cI}. Hence:

$$\alpha_{ext} = \omega_{ext} = 2 * \omega_{cI} \tag{5-84}$$

$$\alpha_{ext} = \omega_{ext} = 160\, rad/s$$

and the damping coefficient ζ is left as one and unmodified from the previous observer design. By substituting the values of (5-84) in (5-83), we have:

$$\begin{aligned} \beta_1 &= 480\ [rad/s] \\ \beta_2 &= 76800\ [rad/s]^2 \\ \beta_3 &= 4096 * 10^3\ [rad/s]^3 \end{aligned} \tag{5-85}$$

After the design has been completed to estimate z_3, a few arithmetic manipulations can be done to obtain the estimated load angle ($\widehat{\theta_L}$) and therefore from (5-69), the estimated torsional torque can also be calculated. Since:

$$z_3 = a(t) = -\frac{K_S}{J_M}(\theta_M - \theta_L) \tag{5-86}$$

and $x_1 = \theta_M$, then:

$$\hat{\theta}_L = \frac{J_M}{K_S} z_3 + x_1 \tag{5-87}$$

Where the hat notation has been added to load angle variable to indicate it as an estimate. The estimated torsional torque can be obtained straightforward with the following formula:

$$\widehat{T_s} = K_s\left(\theta_M - \widehat{\theta_L}\right) \tag{5-88}$$

Notice in this nonlinear extended state observer design the load inertia J_L was not involved. As well as in the obtaining the observer gain parameters in (5-83) no system parameters were used, which shows that this type of observer is inherently robust against any system model uncertainties. It is also worth mentioning the linearization of the function $g(x)$ in (5-82) was done to design the observer gains (β_1, β_2, and β_3). However, during the operation $g(x)$ is used in its nonlinear form which was specified in (5-79).

5.2.8 Simulation results of the nonlinear extended state observer

The designed observer was implemented in Simulink in order to simulate and compare it with the previous Luenberger observer and to test the feasibility of such an observer. The steps to implement such a system in Simulink was a straightforward procedure as it can be built in a similar manner to the block diagram in Figure 5-46. The Simulink blocks are reported in Appendix B. The simulation configuration and system model parameters are left unchanged from the previous simulation. In contrast to the previous tests, In the following only two tests are performed, as summarized in Table IV.

Table IV Tested to be simulated for the nonlinear extended state observer

Configuration	Test 5	Test 6
Mechanical model	Two mass	Two mass
Reference signal	First signal (Figure (5-13)) passes through two resonance intersections	Second signal (Figure (5-14)), steady-state at critical speed
Poles	$\alpha_{ext} = \omega_{ext} = 160\, rad/s$	

The tests simulated only the two-mass mechanical model system and only one choice the observer poles specified in the previous table. The tests were set to be comparable to their corresponding setting from the previous linear observer simulation. For example, test 5 will be compared to test 2 and the same case for test 6 and test 4. Since implementing any type of observer does not affect the baseline system design the base response plots for the motor and load speed are not repeated. However, the angle deflection figures are reported to analyse the level of accuracy the difference between the two type of observers if they exist.

5.2.8.1 Test 5, Nonlinear extended state observer, two-mass system, first reference signal

In this test, the exact same simulation configuration and system parameters as test 2 are used. The comparison points will be the estimation accuracy, and its effectiveness in suppression of torsional vibrations. Since we have a similar case of test 2, the base speed response figures of the motor speed ω_M and load speed ω_L are not repeated and Figure 5-25 is taken as a reference.

5.2.8.1.1 Estimation error

The performance of the angular deflection estimation of the nonlinear extended state observer with the chosen poles of $\alpha_{ext} = \omega_{ext} = 160\, rad/s$ is reported in Figure 5-47, where it can be noticed that the constant error that was perceived in the linear observer is no longer present. With the same observer poles selection the constant error which was identified due to the load torque T_L dropped from $2.4 * 10^{-3}\, rad$, as it was reported in Figure 5-27, to no constant error in the nonlinear observer. We can say with the same pole placement for the two observers, the nonlinear extended state observer outperformed the former. Regarding the error at steady state, it can be calculated as:

$$\frac{0.7642 * 10^{-3} rad}{3.567 * 10^{-3} rad} = 21.42 * 10^{-2} \tag{5-89}$$

The previous value shows the error improved almost by 20% from the best case in (5-61).

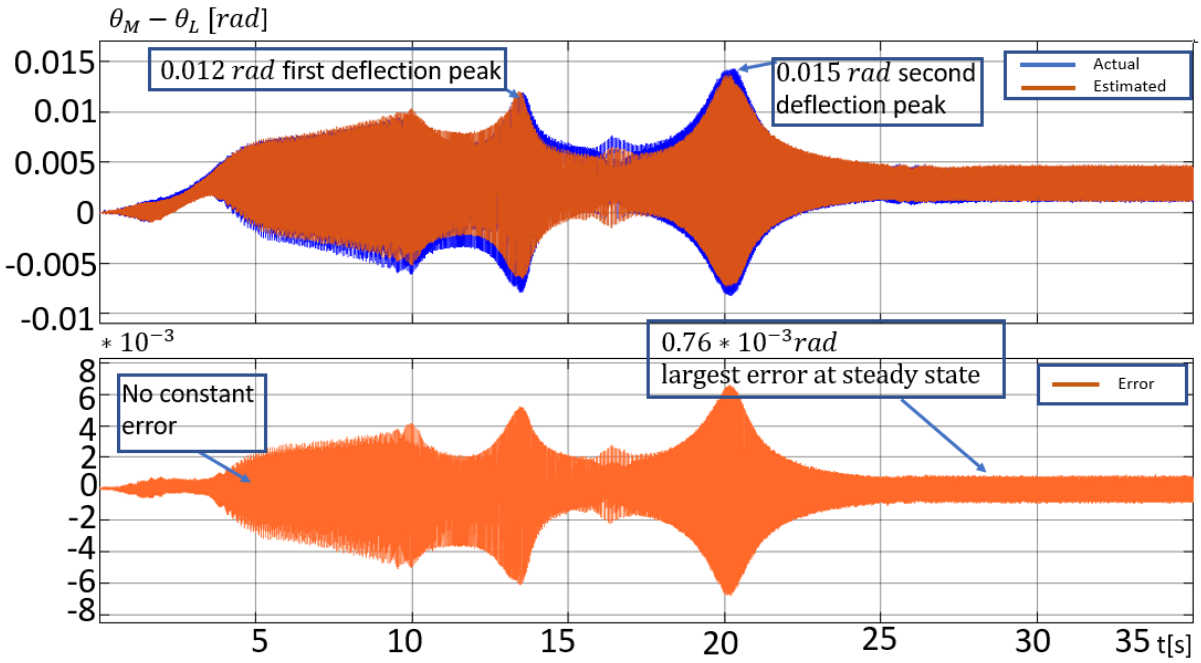

Figure 5-47 Actual and estimated Angular deflection (top) and the estimation error (bottom) of test 5

5.2.8.1.2 Compensated system

The speed response of the motor and the load speed when using the shaft torque (T_s) estimated by the nonlinear extended state observer for feedforward compensation is shown in (5-50). Comparing the results obtained with test 2 speed results in Figure 5-29, it shows that again, the observer is succeeding the task of suppressing the torsional vibrations in a similar manner of the linear observer.

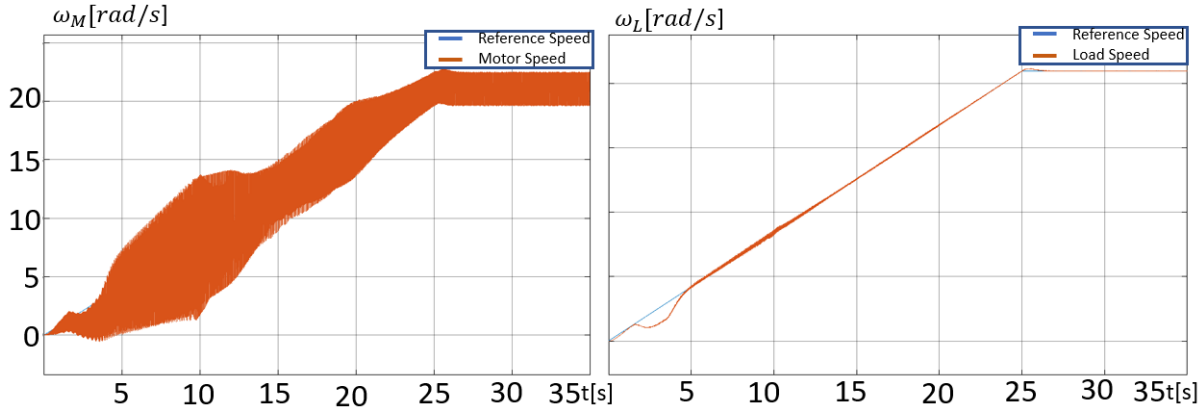

Figure 5-48 Reference speed, motor speed (left), and load speed (right) of the two-mass system of test 5

The angular deflection values after compensation are shown in Figure 5-49. As it was evident from the previous motor speed graph the resonance peaks have been decreased in an identical manner of test 2. Nonetheless there was a significant improvement in the estimation accuracy,

the angular deflection in the figure below shows a mirrored results of what has been obtained by the linear observer from Figure 5-31.

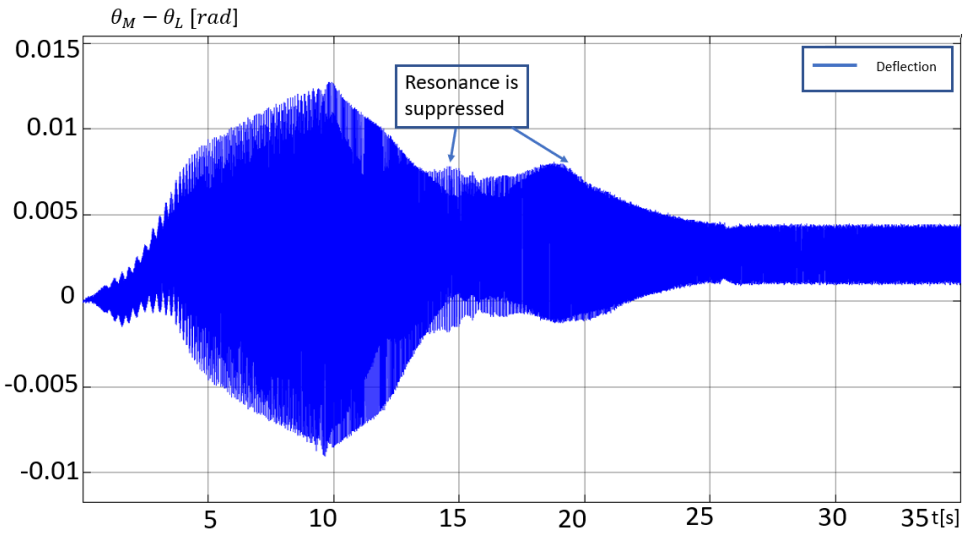

Figure 5-49 Angular deflection of test 5 with the nonlinear extended state observer

5.2.8.2 Test 6, Nonlinear extended state observer, two-mass system, second reference signal

The extended state observer performance is once again tested in case when the system operates at a critical point causing resonance in steady state. This test uses the second speed reference signal shown in Figure 5-14, where we have passed through a critical point at around $t_1 = 13.32s$ and once the system reaches $t_2 = 20s$ the speed reaches to a steady state at the second resonance point. To avoid repetition the speed outputs of the system without the feedforward compensation reported in Figure 5-39 of test 4, in order to be compared after the compensation action have been implemented and simulated.

5.2.8.2.1 Estimation error

Similar to the previous test, Figure 5-50 shows the estimation accuracy of the extended state observer where unlike Luenberger observer, there is no constant error. However, the error in percentages is not reported since it follows the same behaviour as the previous test.

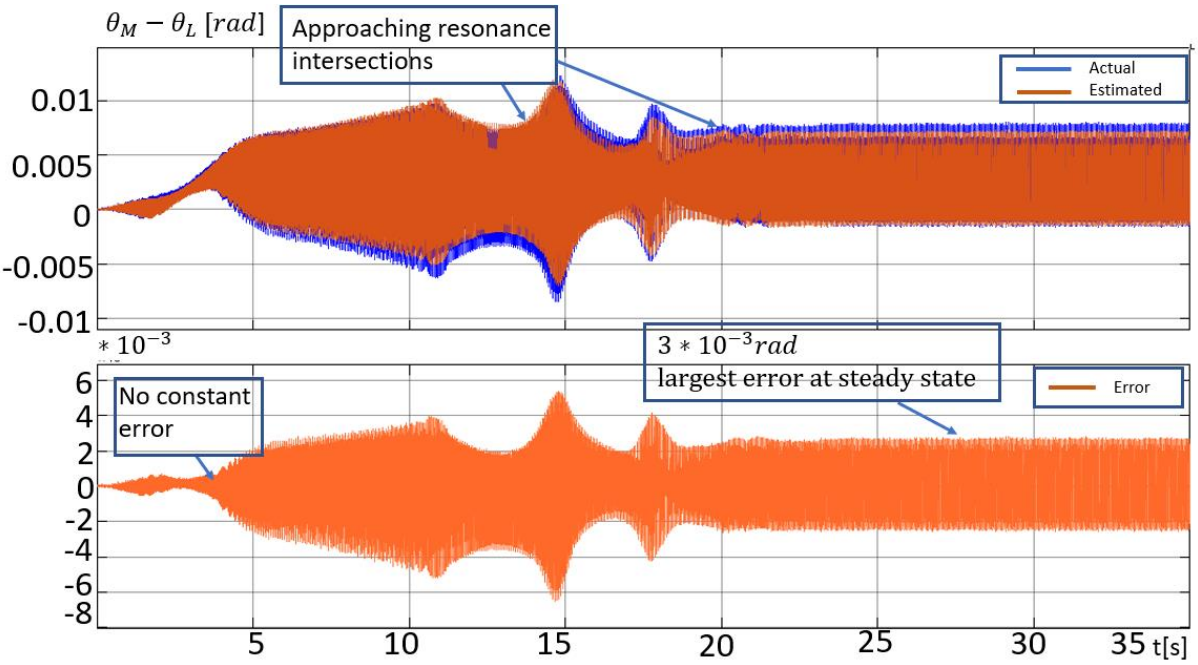

Figure 5-50 Actual and estimated Angular deflection (top) and the estimation error (bottom) of test 6

5.2.8.2.2 Compensated system

The plots for the speed in Figure 5-51 and the angular deflection in Figure 5-52, show an analogous behaviour of what has been reported in test 4 of the linear observer. The first resonance peak at $t = 13.32s$ has been suppressed in both of the figures, and the system is able to operate under the steady state resonance condition after it has been reached at $t_2 = 20s$. Hence, the implementation of the nonlinear extended state observer did not degrade the original performance of the system, in contrast the system is benefited.

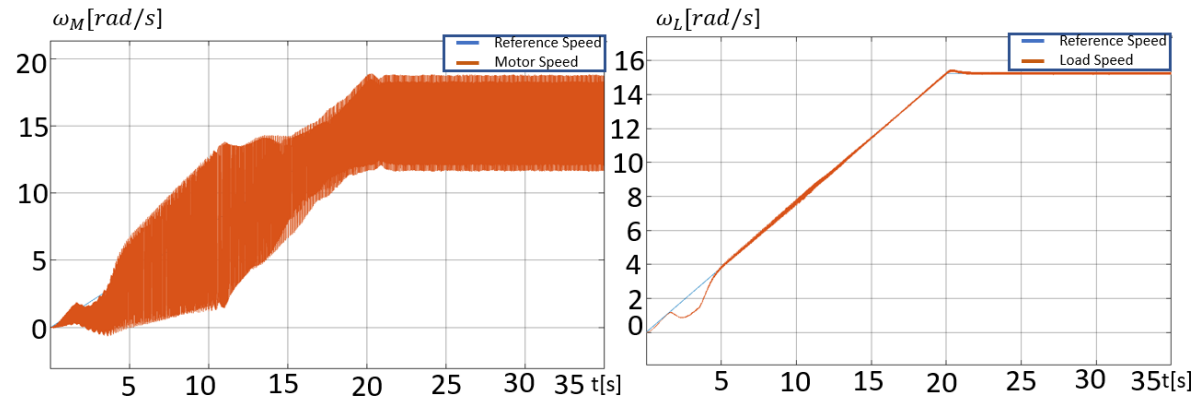

Figure 5-51 Reference speed, motor speed (left), and load speed (right) of the two-mass system of test 6

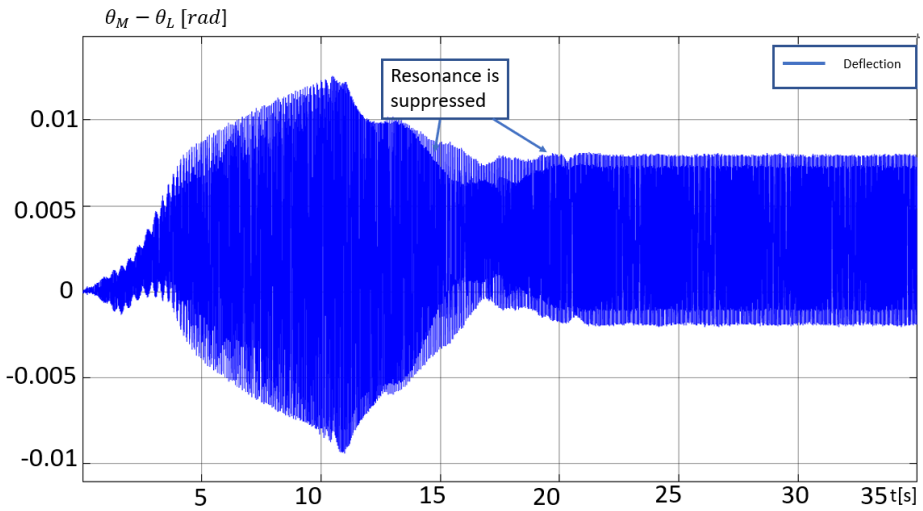

Figure 5-52 Angular deflection of test 6 with the nonlinear extended state observer

Conclusion

Implementing DOBC has shown some evident benefits to the design system, which can be summarized in following points:

- The inclusion of the DOBC using any type of observer did not degrade the nominal performance of the system, instead improved it by implementing the torsional suppression.
- The implementation of the DOBC did not modify the design process of the regular tuning of the PI regulator of system.
- The torsional suppression as seen in the results of the tests 2, 4, 5, and 6 is immediate, the resonance peaks are decreased to match the normal system performance as there was no resonance intersection to be crossed. The speed of such suppression was compared to the baseline of the PI regulators performance where the angular deflection changes due to the resonance lasted for more than two seconds that delay can cause damage to the machine components and decrease its reliability.
- While the linear Luenberger observer and the nonlinear extended state observer followed different formulation paths, both types of the observer showed an identical behaviour regarding the suppression of the torsional vibration.
- The observer estimation accuracy was affected the placement of the observer poles as noticed while simulating the systems with observer 1 and observer 2. Where the first choice of observer pole which were selected to be a larger value than the second showed a better performance against external disturbances in the terms of the accuracy. However, the latter choice showed smaller oscillations.
- The extended state observer is proven to be superior to the Luenberger observer in the design process due to the fact that the former uses less system parameters. Hence, it is inherently more robust against system parameters uncertainties.

Several approaches can be taken to continue the study of the DOBC using the Leuenberger observer and the nonlinear extended state observer for torsional vibration suppresion such as:

- Extending the analysis to multi-mass mechanical systems instead of simple two-mass system.
- Testing the effect of system paramter variation to the DOBC appraoch to the Luenberger observer and the nonlinear extended state observer. It is worth mentioning that the latter observer type is expected to preform in more robust manner due to its indepenadce on the model parameters.
- Testing the suppresion effectivness of the DOBC scheme under the influnce of larger and more random load torques as external disturbances.

This page left intentionally blank

References

[1] S. Filizadeh, *Electric Machines and Drives*. University of Minnesola, Minneapolis, USA, 2016.

[2] J. C. Wachel and F. R. Szenasi, "Analysis of torsional vibrations in rotating machinery," *Proc. twenty-second Turbomach. Symp.*, pp. 127–151, 1993.

[3] S. Yamada and H. Fujimoto, "Vibration suppression control for a two-inertia system using load-side high-order state variables obtained by a high-resolution encoder," *IECON Proc. (Industrial Electron. Conf.*, no. 1, pp. 2897–2903, 2014.

[4] M. Paludetto, "Torsional vibrations and resonances in axial flux PMSMs due to interharmonics presence in High power converters," MSc thesis, Politecnico di Milano, 2017.

[5] M. Mauri, M. Rossi, and M. Bruha, "Generation of torsional excitation in a variable-speed-drive system," *2016 Int. Symp. Power Electron. Electr. Drives, Autom. Motion, SPEEDAM 2016*, pp. 516–521, 2016.

[6] M. A. Corbo and S. B. Malanoski, "Practical design against torsional vibration," *Lantham, New York, Jan 1996*,.

[7] S. Thomsen, N. Hoffmann, and F. W. Fuchs, "PI control, PI-based state space control, and model-based predictive control for drive systems with elastically coupled loads-A comparative study," *IEEE Trans. Ind. Electron.*, vol. 58, no. 8, pp. 3647–3657, 2011.

[8] G. Zhang and J. Furusho, "Speed control of two-inertia system by PI/PID control," *IEEE Trans. Ind. Electron.*, vol. 47, no. 3, pp. 603–609, 2000.

[9] A. Yabuki, K. Ohishi, T. Miyazaki, and Y. Yokokura, "Fine vibration suppression control based on new two-inertia state observer feedback against three-inertia robot joint," *IEEE Int. Symp. Ind. Electron.*, pp. 1093–1098, 2017.

[10] M. Nakao, K. Ohnishi, and K. Miyachi, "Robust Decentralized Joint Control Based on Interference Estimation.," pp. 326–331, 1987.

[11] Y. Kazuaki, M. Toshiyuki, and O. Kouhei, "Vibration Control of a 2 Mass Resonant System by the Resonance Ratio Control," *Ieej Trans. Ind. Appl.*, vol. 113, no. 10, pp. 1162–1169, 1993.

[12] Y. Hori, H. Sawada, and Y. Chun, "Slow resonance ratio control for vibration suppression and disturbance rejection in torsional system," *IEEE Trans. Ind. Electron.*, vol. 46, no. 1, pp. 162–168, 1999.

[13] E. Saito and S. Katsura, "Force control of two-mass resonant system with vibration suppression based on modal transformation," *IECON Proc. (Industrial Electron. Conf.*, pp. 2589–2594, 2012.

[14] S. Thomsen and F. W. Fuchs, "Speed control of torsional drive systems with backlash," *2009 13th Eur. Conf. Power Electron. Appl. EPE '09*, vol. 49, no. 0, pp. 1–10, 2009.

[15] K. Fujikawa, Z. Q. Yang, H. Kobayashi, and T. Koga, "Robust and fast speed control for torsional system based on state-space method," *IECON Proceedings (Industrial*

Electronics Conference), vol. 1. pp. 687–692, 1991.

[16] S. Li, J. Yang, W. H. Chen, and C. Xisong, *Disturbance-Observer-Based-Control-Methods-and-Applications*. Taylor & Francis Group, LLC, 2014.

[17] R. Zhang and C. Tong, "Torsional vibration control of the main drive system of a rolling mill based on an extended state observer and linear quadratic control," *JVC/Journal Vib. Control*, vol. 12, no. 3, pp. 313–327, 2006.

[18] F. Gong and X. Ren, "Extended state observer based adaptive integral sliding mode control for two inertia system," *Proc. - 2015 7th Int. Conf. Intell. Human-Machine Syst. Cybern. IHMSC 2015*, vol. 1, pp. 483–486, 2015.

[19] J. Ji and S. Sul, "Kalman filter and LQ based speed controller for torsional vibration suppression in a 2-mass motor drive system," *IEEE Trans. Ind. Electron.*, vol. 42, no. 6, pp. 564–571, 1995.

[20] K. Szabat and T. Orlowska-Kowalska, "Performance improvement of industrial drives with mechanical elasticity using nonlinear adaptive Kalman filter," *IEEE Trans. Ind. Electron.*, vol. 55, no. 3, pp. 1075–1084, 2008.

[21] A. Tokunaga, M. Nakamura, H. Takami, and T. Okamoto, "An optimal observer design for 2-inertia system via ILQ design method," *Conf. Rec. - IAS Annu. Meet. (IEEE Ind. Appl. Soc.*, pp. 1–8, 2012.

[22] J. F. Gieras, R. J. Wang, and M. J. Kamper, *Axial flux permanent magnet brushless machines*. Springer Science + Business Media B.V, 2005.

[23] F. Caricchi, F. Crescimbini, F. Mezzetti, and E. Santini, "Multistage axial-flux PM machine for wheel direct drive," *IEEE Trans. Ind. Appl.*, vol. 32, no. 4, pp. 882–888, 1996.

[24] S.-H. Kim, *Fundamentals of electric motors*. Elsevier Inc., 2017.

[25] J. Song-Manguelle, G. Ekemb, D. L. Mon-Nzongo, T. Jin, and M. L. Doumbia, "A theoretical analysis of pulsating torque components in AC machines with variable frequency drives and dynamic mechanical loads," *IEEE Trans. Ind. Electron.*, vol. 65, no. 12, pp. 9311–9324, 2018.

[26] R. H. B. Richard C. Dorf, *Modern Control Systems, 13th Ed.* Pearson Education, Inc., Hoboken, New Jersey, 2017.

[27] W. H. Chen, J. Yang, L. Guo, and S. Li, "Disturbance-Observer-Based Control and Related Methods - An Overview," *IEEE Trans. Ind. Electron.*, vol. 63, no. 2, pp. 1083–1095, 2016.

[28] K. Ogata, *Modern Control Engineering 5th Edition*, vol. 39, no. 12. Pearson Education, Inc., Hoboken, New Jersey, 2002.

[29] S. E. Saarakkala and M. Hinkkanen, "State-space speed control of two-mass mechanical systems: Analytical tuning and experimental evaluation," *2013 IEEE Energy Convers. Congr. Expo. ECCE 2013*, no. 1, pp. 3762–3769, 2013.

Appendix A M-files of MATLAB

Inverter limiting function

```
function fo = fcn(fi)

 if ( fi < 4)
        fo=4;
  else
        fo=fi;
 end
 end
```

Campbell Diagram m-file

```
                                          %% Campbell Diagram
close all
clear all
clc
%                                          Mechanical Paramters
frated = 150;              % [Hz] Rated Frequency
wrated = 2*pi*frated;      % [rad/s]
p = 6;                     %          Number of Poles
J_M=2.7e-3;                % [kg*m2] moment of inertia of the motor
J_L=40*J_M;                % [kg*m2] moment of inertia of the load
Jtot = 41*J_M;             % [kg*m2] moment of inertia of the one mass
system
B=0;                       % [N.m.s/rad] viscous friction
K_s=794;                   % [N.m/rad]   Equivalent Coefficient of
Stiffness
Wmrated = wrated*2/p;      % [rad/s] Mechanical Rated Speed;
w_res=sqrt(K_s*(J_M+J_L)/(J_M*J_L)) ;    % [rad/s]       Resonance
Frequency
w_ares=sqrt(K_s/J_L);      % [rad/s]       Anti-Resonance Frequency
f_res=w_res/2/pi;          % [Hz]          Resonance Frequency

%                                       The Construction of Campbell
Diagram
W_M=0:Wmrated;
f_ele= W_M*p/(4*pi);
h_6=6*f_ele;
h_12=12*f_ele;
h_18=18*f_ele;
h_24=24*f_ele;
h_30=30*f_ele;
h_36=36*f_ele;
figure(3)
plot(W_M,h_6,W_M,h_12,W_M,h_18,W_M,h_24,W_M,h_30,W_M,h_36)
yline(f_res)
xlim([0 30])
ylim([0 200])
title('Campbell Diagram');
legend
grid; xlabel('Machine speed [rad/s]'); ylabel('Exciation Frequency
[Hz]');
```

```
h=legend('h_{6}','h_{12}','h_{18}','h_{24}','h_{30}','h_{36}','f_{re
s}');
```

Current and speed PI-regulators m-files

```
                                        %% Current and speed PI-regulators
design %%
%%                                          System Parameters
clc
clear all
close all


%                                           Electrical Paramters
Pn     = 6910;          % [W] Rated Power
Vrated = 350;           % [V] Rated Voltage
i_rated= 15.6;          % [A] Rated Current
Rs     =  0.393;        % [Ohm] Machine Resistance
L_s    =  0.0048;       % [H]   Machine Inductance (isotropic L_d=L_q=L_s]
frated = 150;           % [Hz] Rated Frequency
p = 6;                  %           Number of Poles
wrated = 2*pi*frated;   % [rad/sec]
Wmrated = wrated*2/p;   % [rad/sec] Mechanical Rated Speed;
psiPM=0.165*sqrt(3);    % [Wb]      PM Flux av. measured
Trated = Pn/Wmrated;    % [N.m]     Rated Torque

%                                         Mechanical Paramters
J_M=2.7e-3;             % [kg*m2] moment of inertia of the motor
J_L=40*J_M;             % [kg*m2] moment of inertia of the load
Jtot = 41*J_M;          % [kg*m2] moment of inertia of the one mass system
B1=0;                   % [N.m.s] viscous friction
K_s=794;                % [N/m]   Equivalent Coefficient of Stiffness

%                                         Inverter's PWM Parameters
Vdc=60;                 % [V]     Rated Ideal DC Voltage
f=10;                   % [Hz]    Rated Operating Frequency
m_f=15;                 %         Frequency Modulation Ratio
f_s=m_f*f;              % [Hz]    Switching Frequency
T_s=1/f_s;              % [sec]   Switching Time




%%                                    Current and speed PI-regulators design

s = tf('s');                             % Complex Frequency

%                                       Current Open-loop Transfer Function

L_I = 1/((1+s*T_s)*(s*L_s+ Rs));         %        Open-loop transfer function
for the current controllers

% ploting the transfer function to find the cutoff frequency

figure(1);
w = logspace(0,3,500);                     %          w ranges between 1 and
1E3 rad/s with 500 points
bode(L_I,'r',w);   grid;                   %         Frequency Response of the
open-loop transfer function
```

```
title('Transfer Function of the L_{isd}(s) system regarding the current
loop');

w_cI = 80;                                  % [rad/s] Chosen cutoff frequency
[magI,csI] = bode(L_I,w_cI);            %       Gain and phase corresponding
to the chosen cutoff frequency
phi_I = 10:1:90;                            % [deg]   phase margin
theta_I = -180 + phi_I - csI;
K_PI = cos(theta_I*pi/180)/magI;            % [deg]   Propotional Constant
K_II = -w_cI*sin(theta_I*pi/180)/magI;      %         Integral Constant

%ploting the variance of the PI constant with the change    of the phase
margin

figure(2);
subplot(2,1,1);    plot(phi_I,K_PI);    grid;    xlabel('\phi_{I}    [deg]');
ylabel('k_{pI}');
title('k_{pI} [p.u.] and k_{iI} [1/s] variation with the phase margin phi
[deg]');
subplot(2,1,2);    plot(phi_I,K_II);    grid;    xlabel('\phi_{I}    [deg]');
ylabel('k_{iI}');

phimI = 70;                                 % [deg]   Chosen phase
magdb=20*log10(magI);                       %         Converting to dB
theta_I = -180 + phimI - csI;
K_PI = cos(theta_I*pi/180)/magI;            % [deg]   Propotional Constant
K_II = -w_cI*sin(pi*theta_I/180)/magI;      %         Integral Constant

%         Current closed-loop tranfer function with the designed controller

PID_I = K_PI + K_II/s;                      %         Current PI Controller
L_PII = PID_I*L_I;                      %       Open-loop Transfer Function
F_Is = L_PII/(1 + L_PII);                   %          Closed-loop Transfer
Function
% Frequency response of the open-loop and closed-loop transfer functions
figure(3);
bode(L_PII,'b',F_Is,'r',w); grid;
title('Open-loop   L_{PI_{Is}}(s)   and   closed-loop   F_{is}(s)   transfer
functions');
h=legend('L_{PI_{Is}}(s)','F_{i_{s}}(s)');
%%                                  Speed Open-loop Transfer Function

G_W = 1 / (Jtot*s+B1);                  %       Open-loop transfer function
for the speed controller
L_W = G_W*F_Is;                         %       Open-loop transfer function
with the current closed-loop TF

% ploting the transfer function to find the cutoff frequency

figure(4);
w = logspace(-2,2,1000);                %       w ranges between 1E-2 and
1E2 rad/s with 1000 points
bode(L_W,'b',w);   grid;
title('Transfer  function  of  the  process  L_{\omega}(s)  regarding  the
mechanical loop');

w_cW =3;                                % [rad/s] Chosen cutoff frequency

[magW,csw] = bode(L_W,w_cW);                %           Gain and phase
corresponding to the chosen cutoff frequency
phiW = 10:1:150;                            % [deg]   phase margin
```

```
theta_M = -180 + phiW - csw;
K_PW = cos(theta_M*pi/180)/magW;          %         Propotional Constant
K_IW = -w_cW*sin(theta_M*pi/180)/magW;    %         Integral Constant

%ploting the variance of the PI constants with the change    of the phase
margin

figure(5);
subplot(2,1,1);  plot(phiW,K_PW);  grid;  xlabel('\phi_{  \omega}  [deg]');
ylabel('kp \omega');
title('kp_{\omega} [p.u.] and ki_{\omega} [1/s] with \phi [deg]');
subplot(2,1,2);   plot(phiW,K_IW);   grid;   xlabel('\phi_{\omega}   [deg]');
ylabel('ki \omega');



phimW = 60;                               % [deg]   Chosen phase
magdb=20*log10(magW);                     %         Converting to dB
theta_I = -180 + phimW - csw;
K_PW = cos(theta_I*pi/180)/magW;          %         Propotional Constant
K_IW = -w_cW*sin(pi*theta_I/180)/magW;    %         Integral Constant

%       whole system closed-loop tranfer function with the designed controller

PID_W = K_PW + K_IW/s;                    %         Speed PI Controller
L_PIW = PID_W*L_W;                           %           Open-loop Transfer
Function
F_W = L_PIW/(1 + L_PIW);                   %          Closed-loop Transfer
Function
% Frequency response of the open-loop and closed-loop transfer functions
figure(6);    bode(L_PIW,'b',F_W,'r',w); grid;
title('Open-loop  L_{PI\omega}(s)  and  closed-loop  F_{\omega}(s)  transfer
functions');
legend('L_{PI\omega}(s)','F_{\omega}(s)');
```

Current controllers figures and tuning procedure

The bandwidth of the system under control is found to be $50.3\ rad/s$, then the current closed-loop cutoff frequency is chosen to be $\omega_{cI} = 80 rad/s$. Testing the effect of varying the PI control parameters K_{PI} and K_{iI} at the same point to study the phase margin noted by ϕ_I for the current controller is done. The phase angle at the stable point is given by:

$$\theta = -180 + \phi_I - \alpha_I$$

where α_I is the phase shift at the chosen cutoff frequency (ω_{cI}). Figure 0-1 is produced by evaluating different phase margin requirements at the cutoff frequency for the PI parameters using the following equations:

$$\begin{aligned} K_{PI} &= cos(\theta)/m_I \\ K_{II} &= -\omega_{cI}\, sin(\theta)/m_I \end{aligned} \qquad (0\text{-}1)$$

The response magnitude is noted by m_I. The criteria for stability require both the parameters to have the same sign and to be real. In addition, a suggested phase margin is chosen no less than 45^o shows that the phase margin ϕ_I should not exceed $89^o$to satisfy the criterion.

Therefore, in this case the phase margin is chosen $\phi_I = 70^o$. The parameters of the PI current regulator are:

$$K_{PI} = 0.7604\,\Omega$$

$$K_{II} = 20.728\,\Omega/s$$

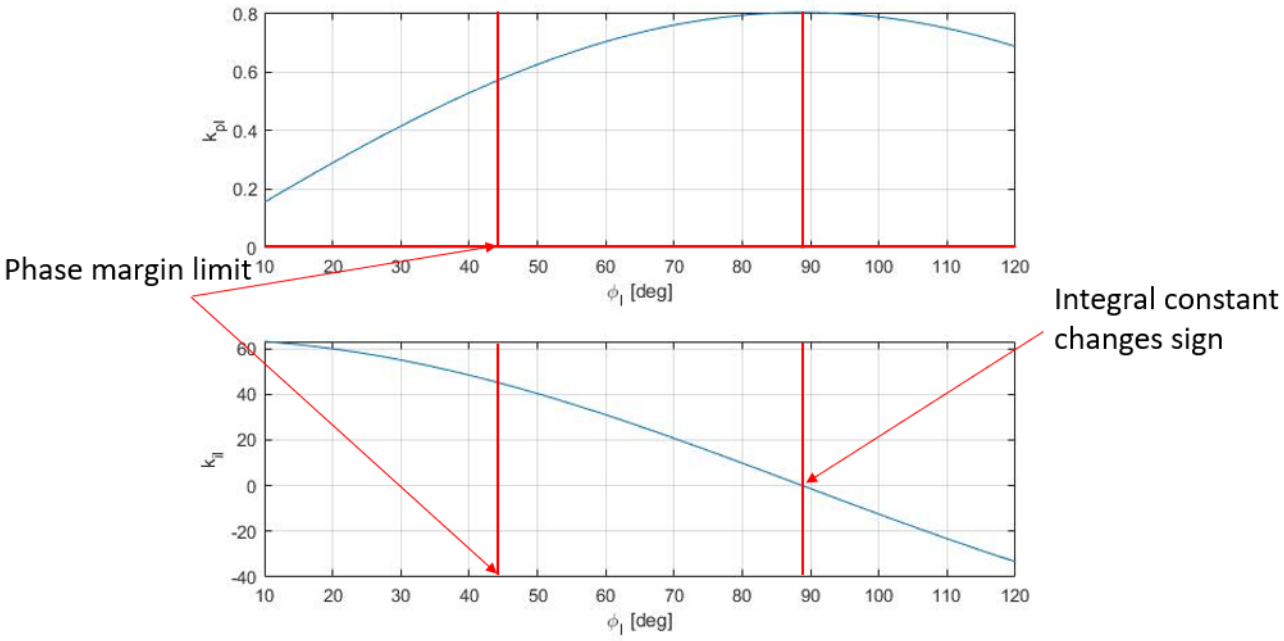

Figure 0-1 PI current regulator parameters variation along different values of the phase margin

Checking the design values from the open and closed-loop transfer functions frequency response by plotting the bode plot of the equations (5-5) and (5-6) is shown in Figure 5-5. It can be noticed the phase margin criterion is fulfilled at the chosen cutoff frequency.

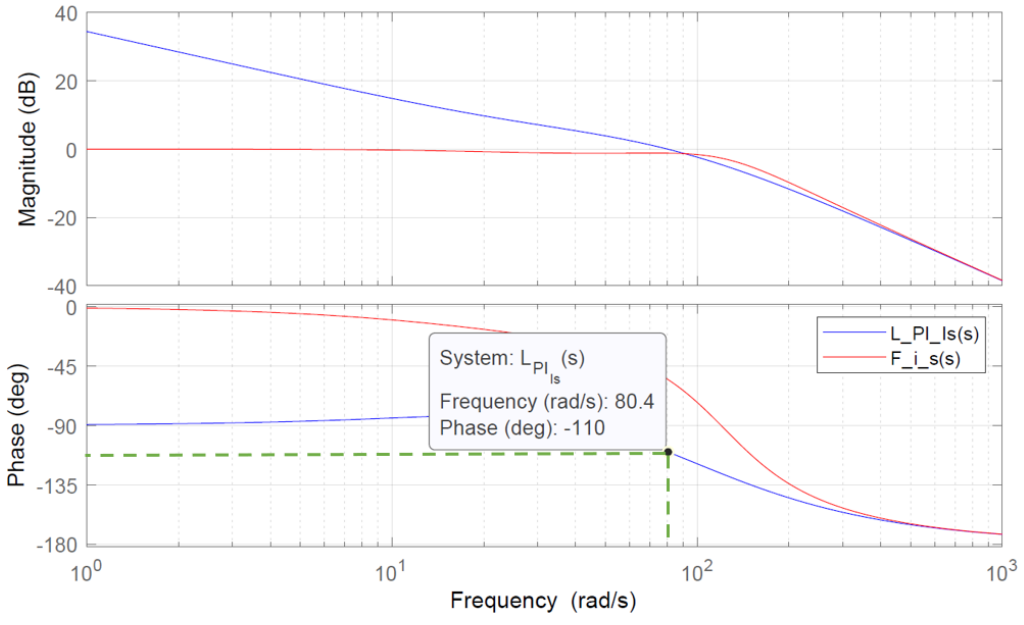

Figure 0-2 Bode plot of the open-loop and closed-loop of the current regulator

Speed regulator figures and tuning procedure

The next step is to choose a suitable phase margin to ensure the stability. Figure 0-2 shows that a phase margin below 88^o meets the condition of having both control parameters to be positive. The phase margin in this case is chosen to be $\phi_\omega = 60^o$.

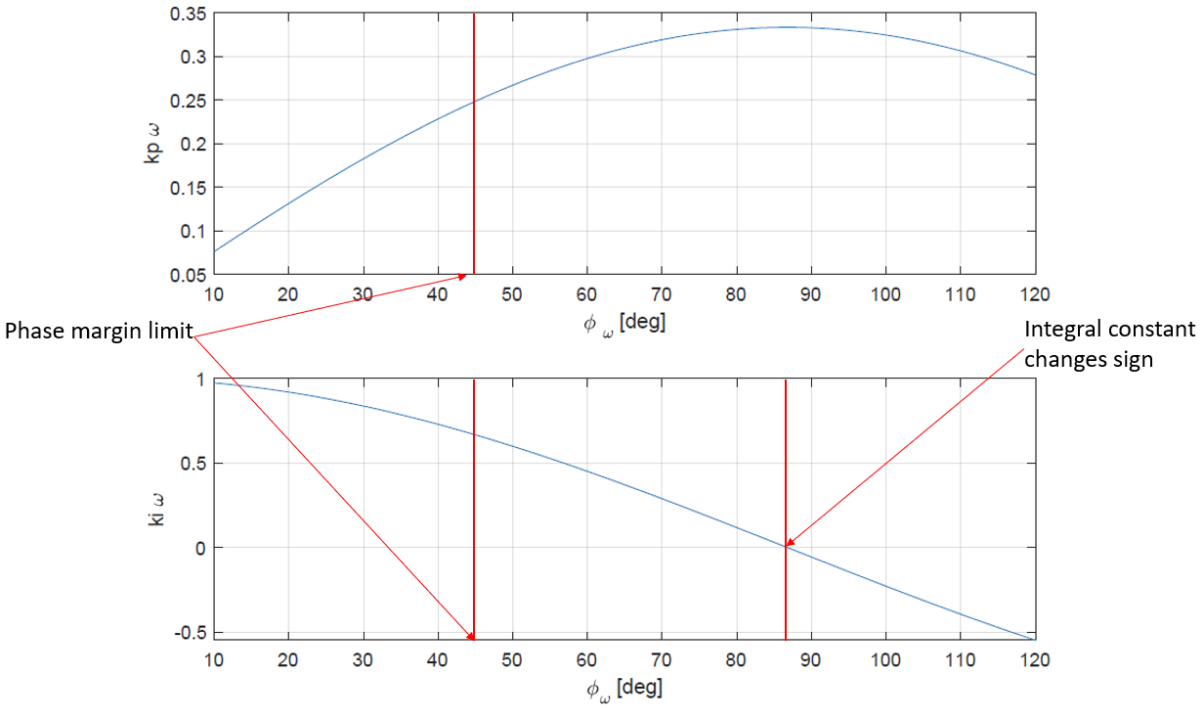

Figure 0-3 PI speed regulator parameters variation along different values of the phase margin

Substituting the phase margin requirement, the gain at the cutoff frequency, and the cutoff frequency results the following PI constants:

$$K_{P\omega} = 0.2975\ Nms/rad$$

$$K_{I\omega} = 0.4503\ Nms/rad$$

The phase margin design requirement is met by analyzing the bode plot of the open-loop transfer function in Figure 5-6

System and simulation parameters and the construction of the observer m-files

```
% PMSM of Castelli Dezza DC brushless. Servomac Type BMS14243619
% 6.91kW 6 poles, 3000 rpm, Tstall=22Nm, Tpeak=88Nm, Istall=15.6A,
% Ipeak=70A.... (Measured Resistance LL 0.25 ohm, Measure PsiPM 0.288 Wb)

%%                                          System Parameters
clc
clear all
close all
```

```
%                                        Electrical Paramters
Pn     = 6910;          % [W] Rated Power
Vrated = 350;           % [V] Rated Voltage
i_rated= 15.6;          % [A] Rated Current
R_s     =  0.393;       % [Ohm] Machine Resistance
L_s     =  0.0048;      % [H]   Machine Inductance (isotropic L_d=L_q=L_s]
frated = 150;           % [Hz] Rated Frequency
p = 6;                  %           Number of Poles
wrated = 2*pi*frated;   % [rad/s]
Wmrated = wrated*2/p;   % [rad/s] Mechanical Rated Speed;
psiPM=0.165*sqrt(3);    % [Wb]      PM Flux av. measured
Trated = Pn/Wmrated;    % [N.m]     Rated Torque

%                                       Mechanical Paramters
J_M=2.7e-3;             % [kg*m2] moment of inertia of the motor
J_L=40*J_M;             % [kg*m2] moment of inertia of the load
Jtot = 41*J_M;          % [kg*m2] moment of inertia of the one mass system
B=0;                    % [N.m.s/rad] viscous friction
K_s=794;                % [N.m/rad]   Equivalent Coefficient of Stiffness

%                                       Inverter's PWM Parameters
Vdc=60;                 % [V]     Rated Ideal DC Voltage
f_ele=10;               % [Hz]    Rated electrical Operating Frequency
m_f=15;                 %         Frequency Modulation Ratio
f_s=m_f*f_ele;          % [Hz]    Switching Frequency
t_s=1/f_s;              % [s]   Switching Time

%                                       PI regulatiors coefficients
% w_cI = 80;  w_cW=3
Ccurr_Kp = 0.7604;
Ccurr_Ki = 20.7289;
Cmecc_Kp = 0.2975;
Cmecc_Ki = 0.4503;

%                                       Simulation Paramters
Ts =8e-6;               % [s]     Sample time in the powergui block
t_stop=11;              % [s]     Simulation total time
Tstep=4e-6;             % [s]     Maximum step size, variable-step solver
slope_speed=0.1;        %         Reference Speed Slope Speed
slope_torque=0.5;       %         Load Torque Slope Speed
TL_start=1.5;           %         Load Torque Insertion Time
Wref=4*pi*f_ele/p;      % [rad/s] Reference Operating Mechincal Speed
TL=0.1*Trated;          %         Reference Load Torque

                              %% Defining the state Space Representation Of
the System

%x(t)=[omega_M (theta_M-theta_L) omega_L]
% [nx1] The State Variables Of The System
%u(t)=[T_Mref]                              % [mx1] The Control Input
%d(t)=[T_L]                                 % [mx1] The %Disturbance
%y(t)=[W_M]                                 % [lx1] System Output
A=[-B/J_M -K_s/J_M B/J_M;1 0 -1; B/J_L K_s/J_L -B/J_L];
% [nxn] State Space Matrix
B_u=[1/J_M;0;0];                            % [nXm] Control Inputs Matrix
B_d=[0; 0 ;-1/J_L];                         % [nXm] Distrubance Matrix
C=[1 0 0] ;                                 % [lXn] Output Matrix
D=[0];
% Forming:
%        dx/dt = Ax(t) + B_uu(t)+B_dd(t)
```

```
%            y(t) = Cx(t) + Du(t)

                                %% Checking  the observerablility of the
system
% obbtest=[transpose(C) transpose(A)*transpose(C)
(transpose(A))^2*transpose(C)];
% ranka=rank(obbtest);
% The rank agrees with n


                                %% choosing the observer gains

w_res=sqrt(K_s*(J_M+J_L)/(J_M*J_L)) ;% [rad/s]       Resonance Frequency
w_ares=sqrt(K_s/J_L);                % [rad/s]       Anti-Resonance
Frequency
f_res=w_res/2/pi;                    % [Hz]          Resonance Frequency

w_d=2*w_ares/3+w_res/3 ;             % [rad/s]       selected frequency
w_cI= 80 ;                           % [rad/s]       cut off frequency of
the current regualtors

                                     % First Choice of observer poles
w_obs=w_d
alpha_obs=w_res
zeta=1;
                                     % Second Choice of observer poles
% w_obs=2*w_cI
% alpha_obs=2*w_cI
% zeta=1;

L_1= alpha_obs+2*zeta*w_obs;
L_2=1+J_M/J_L-J_M*(2*zeta*w_obs*alpha_obs+w_obs^2)/K_s;
L_3=(J_M*alpha_obs*w_obs^2)/K_s-J_M*L_1/J_L;
Ke=[L_1; L_2 ;L_3]

                                          %% Extended state observer

zeta_2=1;
alpha_ext= 160;
w_ext=160;

b1=2*zeta_2*w_ext+alpha_ext;
b2=2*zeta_2*alpha_ext*w_ext+w_ext^2;
b3=w_ext^2*alpha_ext;
```

Appendix B Simulink block diagrams

Mechanical system

The first part in Figure 0-1 shows the mechanical system inputs and motor side equation responsible to calculate the motor speed (ω_M), torsional torque (T_S), and the angular deflection $\theta_M - \theta_L$.

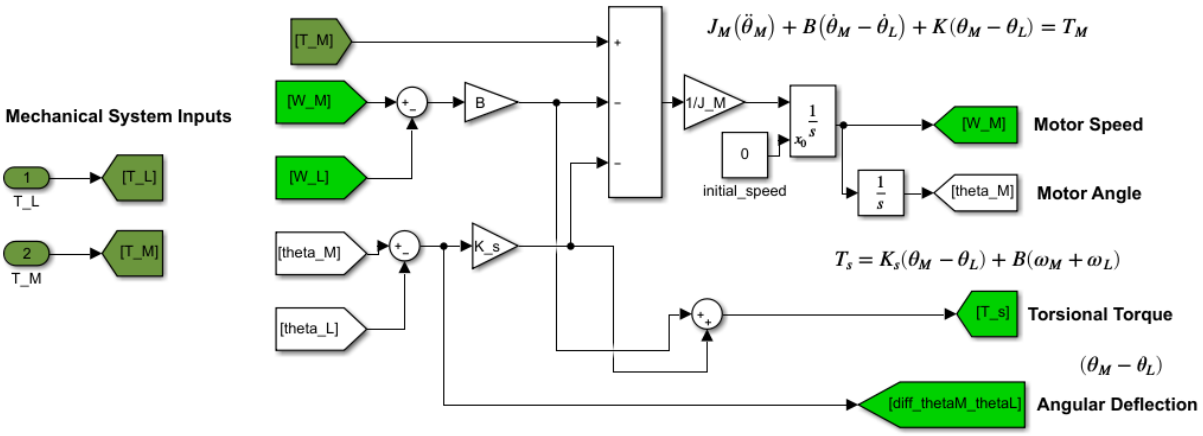

Figure 0-1 First part of the two mass mechanical system in Simulink

The second part of the model shows the block diagram of the representation of the load equation resulting the load speed (ω_L), and the whole mechanical system output can be seen on the right hand side of Figure 0-2.

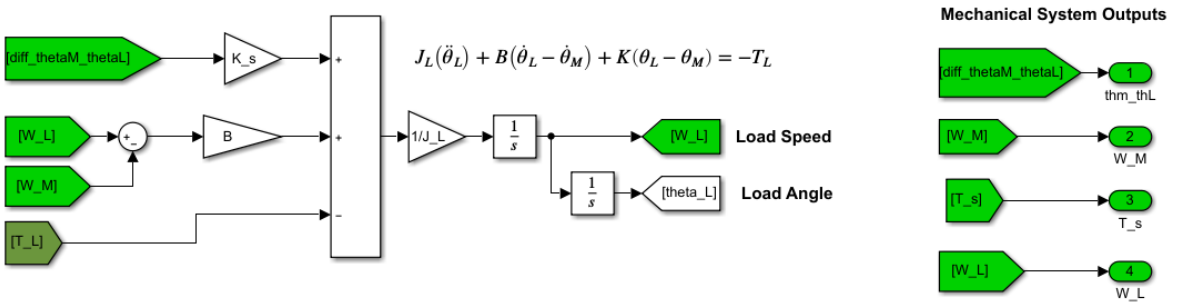

Figure 0-2 Second part of the two-mass system in Simulink

Finally, for the sake of comparison, the one-mass model of the mechanical system is also created in Simulink shown completely in Figure 0-3.

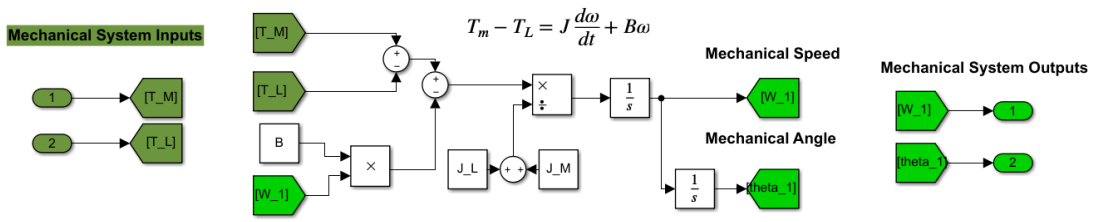

Figure 0-3 One-mass mechanical system block diagram

Electrical machine model

In the following the block diagrams of each section representing the system is reported. As any machine the inputs of the system are the applied phase voltage, and for the PM machine the electrical speed is also considered as input in order to calculate the position of the rotor for the projection of the direct and quadrature components as seen in Figure 0-4.

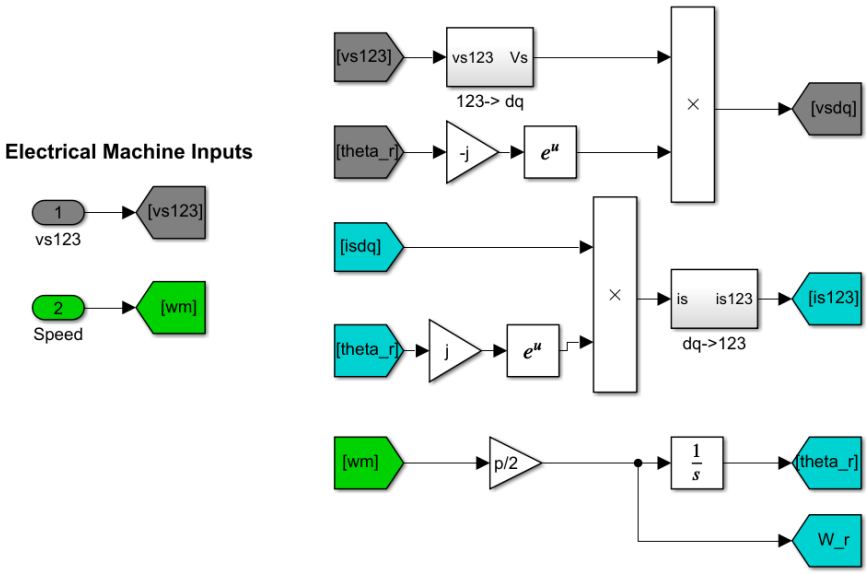

Figure 0-4 PM machine inputs and the calculation of the voltage and current components

Next is the calculation of the stator flux of the machine, by rearranging and integrating equation (4-7) seen in the block diagram Figure 0-5

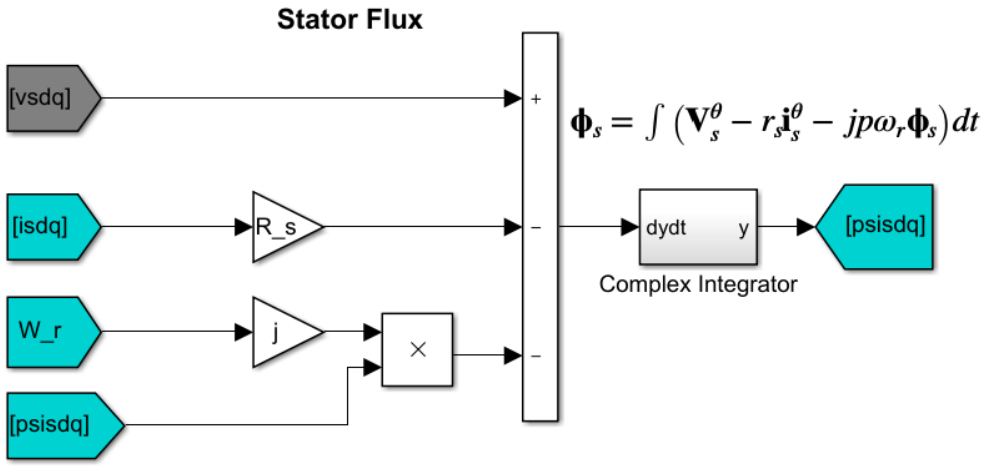

Figure 0-5 Stator flux calculation block diagram

The direct and quadrature current components can be obtained from the stator flux from equation (4-8) showed in Figure 0-6

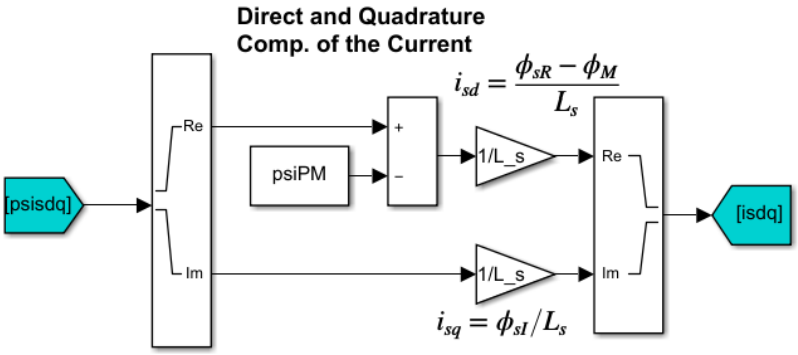

Figure 0-6 Direct and quadrature current components

Finally, the electromagnetic torque is calculated from (4-11), the block diagram showing the torque and the machine outputs are in Figure 0-7.

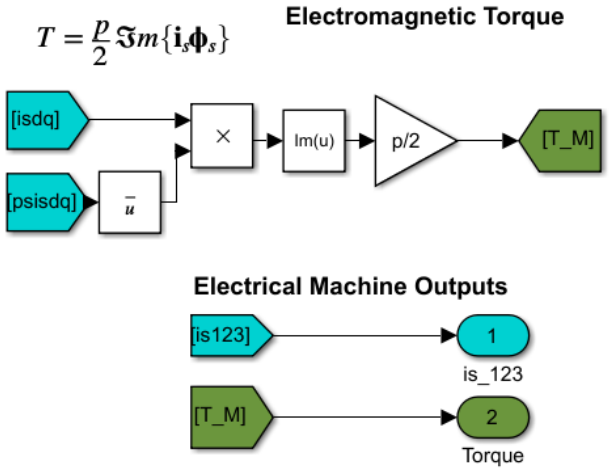

Figure 0-7 Electromagnetic torque and machine outputs

PWM inverter

As in Figure 0-8, The MATLAB function appearing on the left of the figure is to define the switching frequency which at the beginning is constant, and then starts increasing linearly as the machine accelerates.

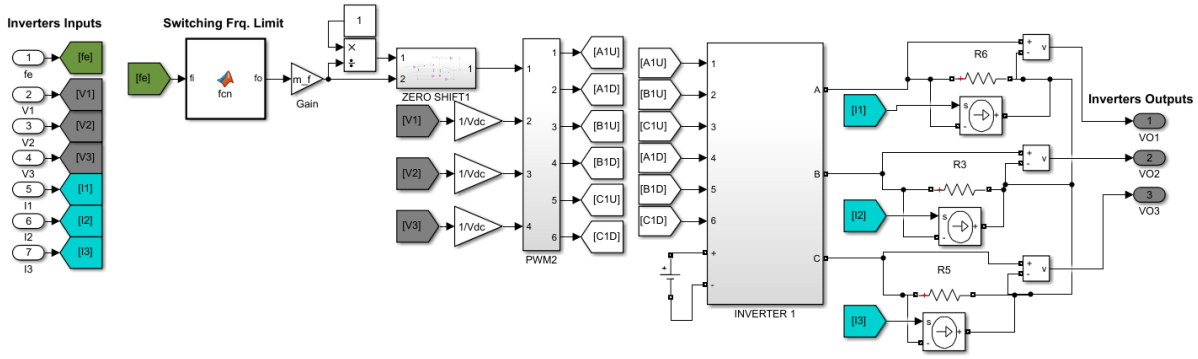

Figure 0-8 PWM inverter implementation in Simulink supplied by Ideal DC voltage source

Control system

Building the PI regulators in Simulink is a straightforward procedure as seen for the current controllers in Figure 0-9. As seen on the left of the figure the inputs of the current controllers are the reference and measured values of the current components and the reference quadrature current component has been calculated according to equation (4-12) from section 0. In addition to the current signals, the electrical angle is also used to transfer the voltages from the direct and quadrature reference frame to three phase symmetrical system, which is the output of this part of the regulators.

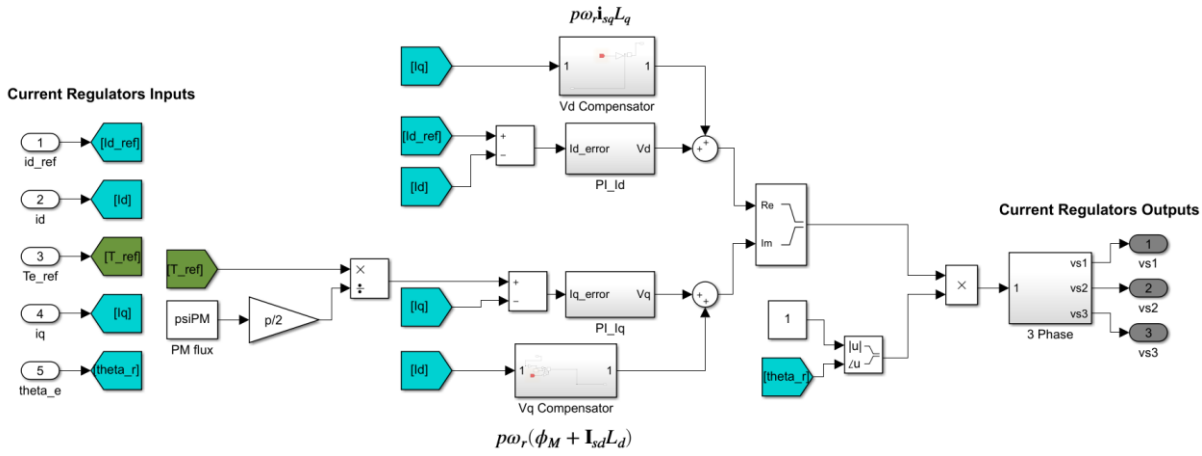

Figure 0-9 PI current regulators in Simulink

As for the speed controller the same concept applies with routing the reference and measured values of the speed. In addition, the reference speed is generated by a simple ramp function saturated with the reference speed as shown in Figure 0-10. In addition, the electrical frequency is also calculated in this stage to be used later on in the PWM inverter.

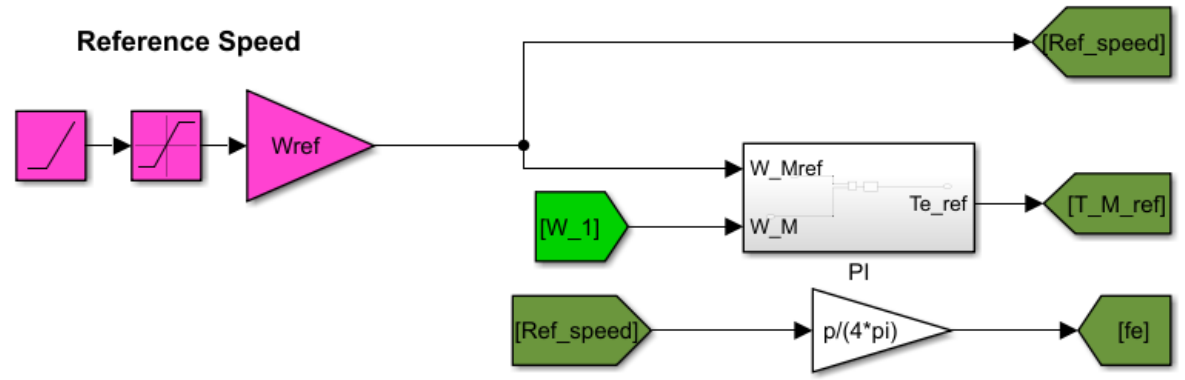

Figure 0-10 Reference speed generation and PI speed regulator.

With the completion of the speed regulator design, the benchmark of the synchronous machine is ready.

Time domain observer

Figure 0-11 shows the complete design of the observer where the input signal (u) is the torque reference (T_{Mref}) which is the output from the speed controller, and the output signal (y) is the motor speed given by the speed encoder. The outputs of the observer are the estimated state variables seen in Figure 5-15.

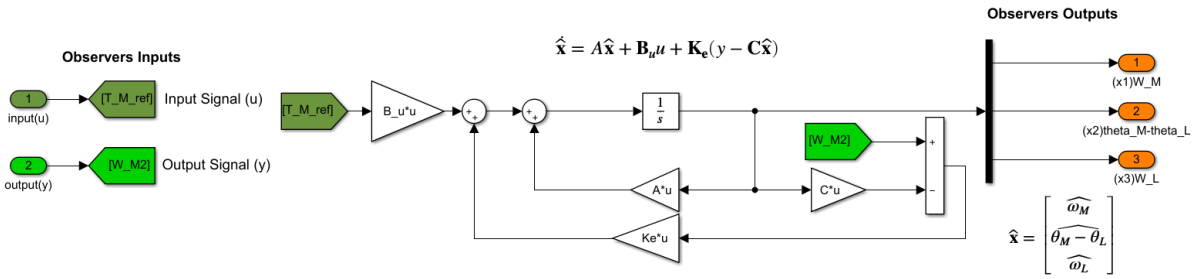

Figure 0-11 Time-domain observer implementation in Simulink

The overall block of the observer, with the obtained estimated torsional torque is shown in Figure 0-12.

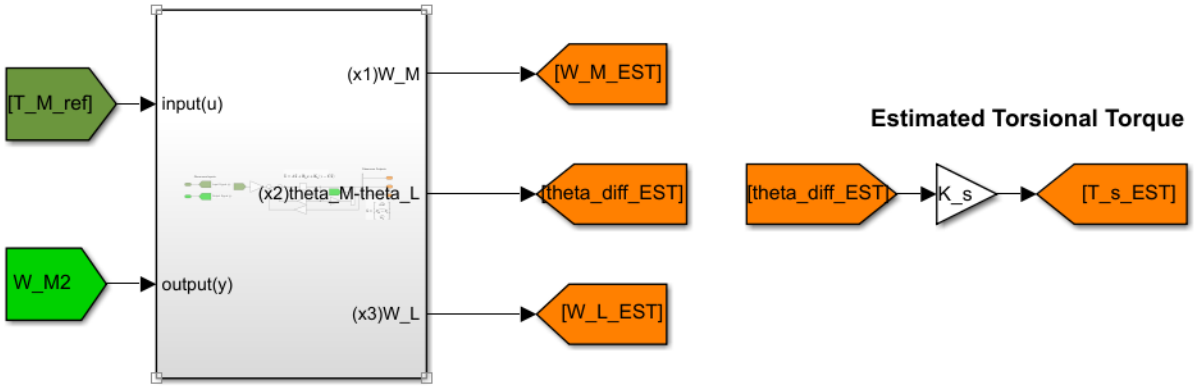

Figure 0-12 Overall representation of the observer in Simulink

Finally, to compensate the estimated torsional torque, the signal is simply added to the torque reference value as shown in Figure 0-13.

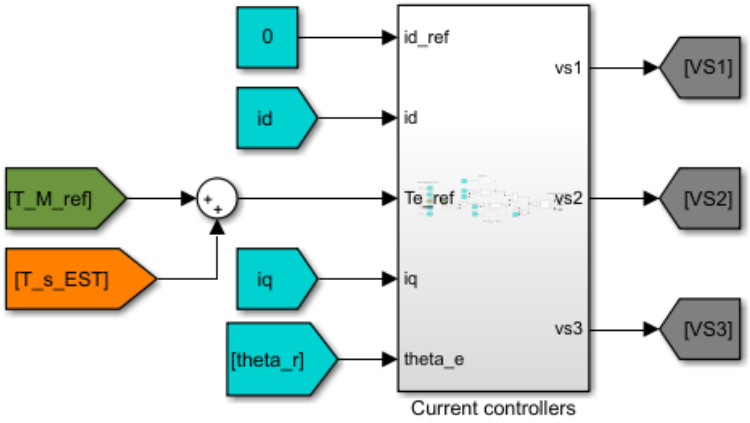

Figure 0-13 Compensation action in Simulink

Nonlinear extended state observer

Figure 0-14 shows the first part and the main part of the observer as it was designed in chapter 5. The figure shows the input of the observer as the motor speed (ω_M) and the motor torque reference speed T_{Mref}. The motor speed is then converted to a the motor angle θ_M with a simple integration operation as seen on the left hand side.

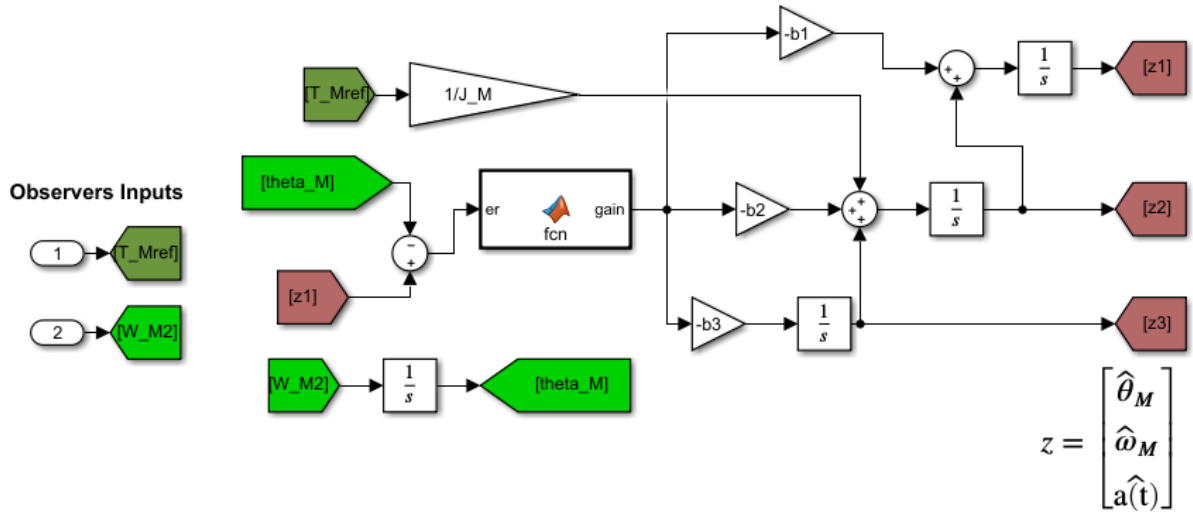

Figure 0-14 First part of the nonlinear extended state observer

The second part of the observer in Figure 0-15 shows the algebraic operations to obtain the estimated angular deflection ($\widehat{\theta_M - \theta_L}$), and the estimated torsional torque ($\hat{T}_s$). In addition, the output of the observer shown on the right part of the figure.

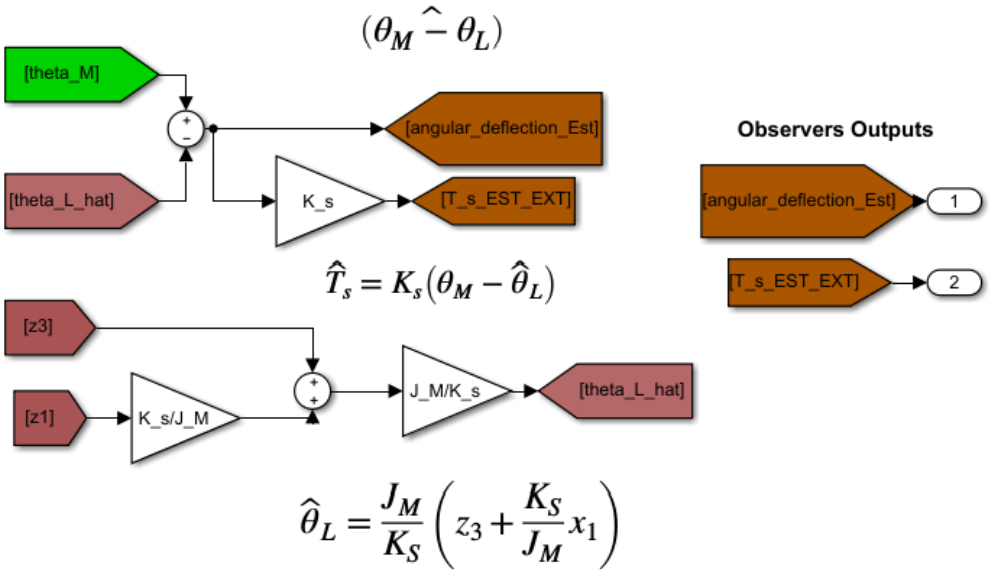

Figure 0-15 Second part of the nonlinear extended state observer

Systems overview

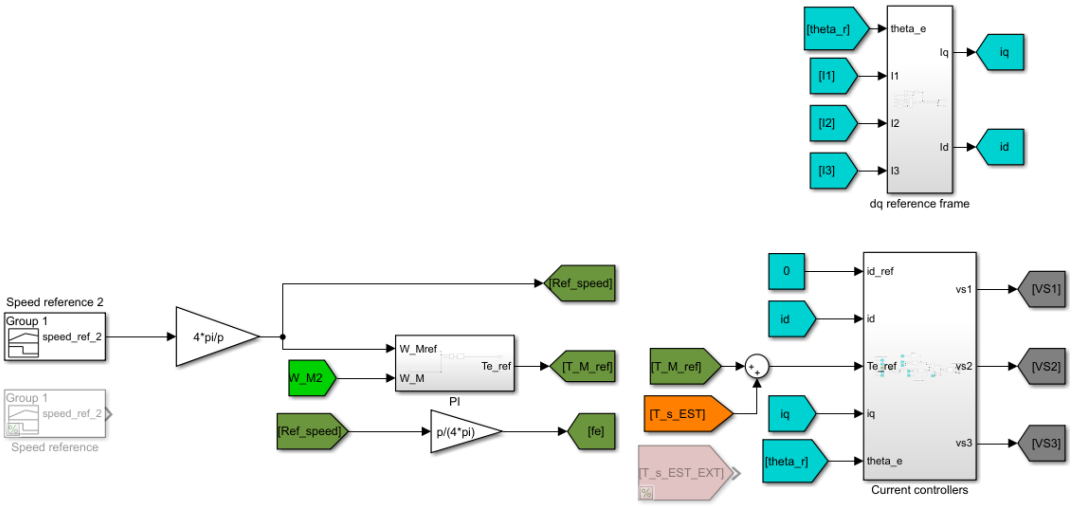

Figure 0-16 System overview part one

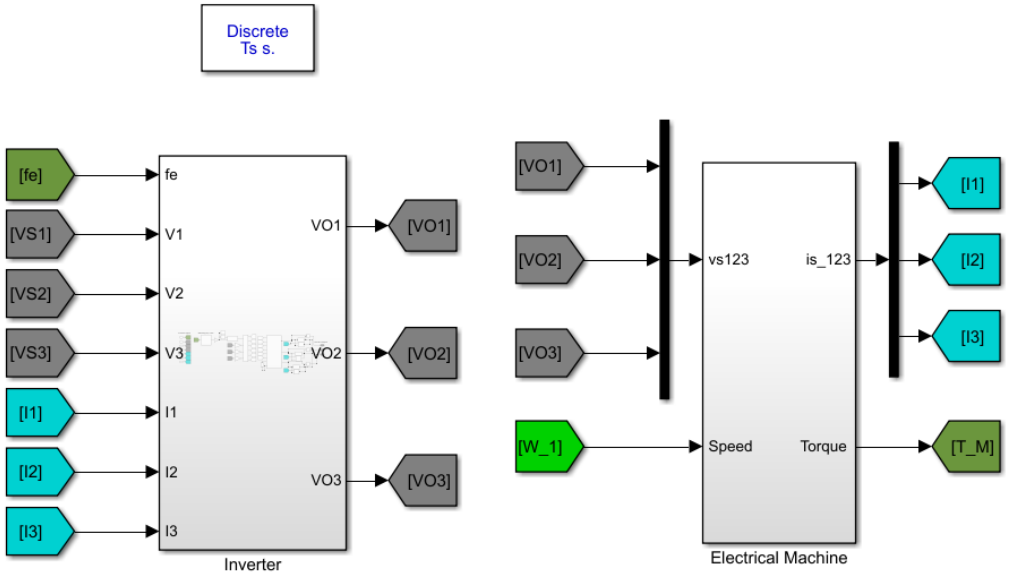

Figure 0-17 System overview part two

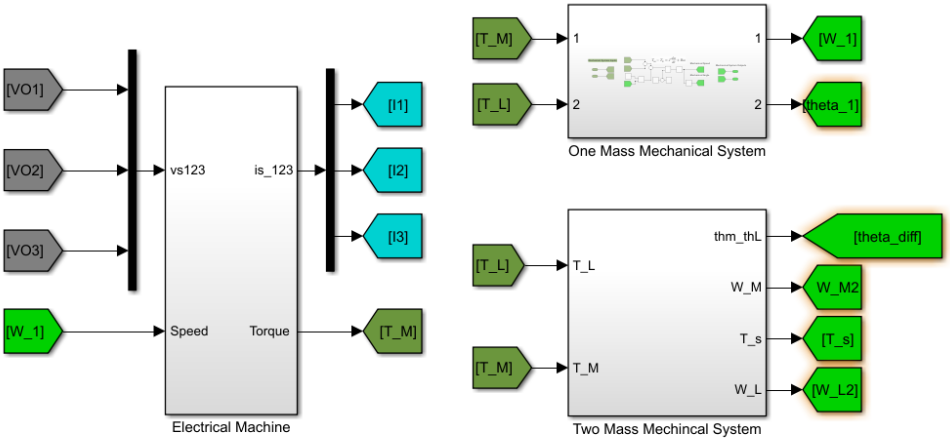

Figure 0-18 System overview part three

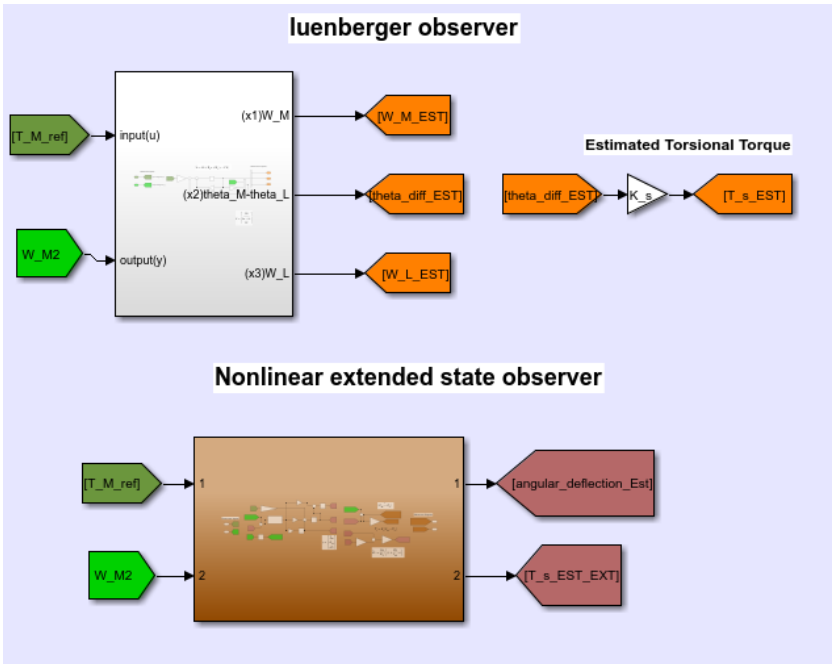

Figure 0-19 System overview part four